In-pixel temperature sensors for dark current compensation of a CMOS image sensor

Abarca Prouza, A.N.

DOI
10.4233/uuid:e39ef7a3-7756-4ab4-a55b-92bce28a76fa

Publication date
2021

Document Version
Final published version

Citation (APA)
Abarca Prouza, A. N. (2021). *In-pixel temperature sensors for dark current compensation of a CMOS image sensor*. [Dissertation (TU Delft), Delft University of Technology]. https://doi.org/10.4233/uuid:e39ef7a3-7756-4ab4-a55b-92bce28a76fa

IN-PIXEL TEMPERATURE SENSORS FOR DARK CURRENT COMPENSATION OF A CMOS IMAGE SENSOR

Dissertation

for the purpose of obtaining the degree of doctor
at Delft University of Technology
by the authority of the Rector Magnificus Prof.dr.ir T.H.J.J. van der Hagen
chair of the Board for Doctorates
to be defended publicly on
Monday 13, September 2021 at 15:00 o'clock

by

Accel Nicolás ABARCA PROUZA
Master of Science in Electrical Engineering,
Delft University of Technology, the Netherlands
born in Santiago, Chile

This dissertation has been approved by the promotor.

Composition of the doctoral committee:

Rector Magnificus,	chairperson
Prof.dr.ir. A.J.P. Theuwissen	Delft University of Technology, promotor

Independent members:

Prof.dr. K.A.A. Makinwa	Delft University of Technology
Prof.dr. K. Bliznakova	Medical University of Varna, Bulgaria
Prof.dr. P. Magnan	ISAE Toulouse, France
Prof.dr. M.A. Diaz	University of Chile, Chile
Dr. Q. Fan	Delft University of Technology
Dr.ir. G. Meynants	Katholieke Universiteit Leuven, Belgium

Reserve member:

Prof.dr. P.J. French	Delft University of Technology

Keywords: CMOS image sensor, temperature sensor, Tixel, In-Pixel, dark current
Printed by: Gildeprint: https://www.gildeprint.nl/
Cover by: Idea Dorottya Erdős; Designed by Gildeprint: https://www.gildeprint.nl/

ISBN: 978-94-6419-302-2
An electronic copy of this dissertation is available at http://repository.tudelft.nl/

This research was funded by the EXIST project, and also funded by CONICYT.

To Dóri and Lucía

TABLE OF CONTENTS

1 INTRODUCTION

Over the last few decades, thanks to the electronic revolution which has taken place, our quality of life has improved significantly. One of the most important results of this revolution is the CMOS image sensor (CIS). Image sensors are utilized in different applications ranging from medical devices to surveillance, as well as astronomy and beyond. Noise is an important parameter of an image sensor, i.e. the random signals recorded with and without light. In a given image sensor, this can be expressed in terms of the so-called dark signal non-uniformity (DSNU). In principle, DSNU can be improved by signal processing techniques. However, this requires an accurate knowledge of the image sensor's temperature, since DSNU highly depends on temperature. The focus of this thesis is on the design and implementation of a CMOS image sensor with in-pixel temperature sensors to estimate the thermal distribution of the pixel array to locally compensate for the dark signal of a CIS.

In this chapter, a background on semiconductors electronic devices is given in Section 1.1. A short introduction to CMOS image sensors as well as temperature sensors is presented in Section 1.2. The motivation and objectives of this thesis are introduced in Section 1.3. Finally, the thesis outline is given in Section 1.4.

1.1 Background

Semiconductors are the basis of electronic circuits. The characteristic property of becoming a conductor under certain circumstances while acting as an insulator under others conditions, has given semiconductors a key role in electronics. Their study dates back to 1782 when Alessandro Volta first used the term “semiconductor” to describe the properties of a material [1]. Many elements as well as compounds have semiconducting properties similar to [2]: elements from group 14 of the periodic table including silicon (Si) and germanium (Ge); binary compounds such as gallium arsenide (GaAs) and silicon carbide (SiC); some ternary compounds; and some organic semiconductors. Initially, Ge was the dominant semiconductor because of its superior carrier mobility compared to Si which resulted in a better electrical performance [3], [4]. However, in 1959, the “surface passivation by thermal oxidation” technique was developed by M. Attala at Bell Labs [5]. This key moment in semiconductor history allowed Si devices to surpass the conductivity and performance of Ge devices, allowing Si devices to become the dominant devices used in prominent semiconductor industries [6], [7]. It is also worth mentioning that Si, of all the semiconductors, is the most abundant material on Earth [8], making Si devices more cost-effective than Ge devices. While the semiconductor industry was developed around Ge and Si, in 1947 the first working junction called the “point-contact transistor” was designed by Shockley’s team at AT&T’s Bell Labs [9]. This milestone marked the initiation of further development in the semiconductor-electronic industry. The first bipolar junction transistor (BJT) integrated circuit (IC) was designed by Kilby and Noise in 1959 [10]. The invention of the IC led to the development of metal oxide semiconductor (MOS) structures. All these inventions from the 1940s and 1950s led to the semiconductor revolution, which has been compared to the industrial revolution due to the impact it has had on modern society [11].

1.2 CMOS Image Sensor and Temperature Sensor

Of all the electronic sensors that have emerged from the semiconductor (r)evolution, there are two which are widely used: the image sensor and the temperature sensor. Both sensors are used in a variety of applications such as: surveillance, medical, astronomy, cameras, and temperature control [12], [13], [14], [15].

1.2.1 CCD Image Sensor and CMOS Image Sensor

There are two main types of image sensor: the charge coupled device (CCD) and the CMOS image sensor (CIS). They both make use of the same principle to capture light based on a photosensitive element, but they differ in their readout systems [16]. The CCD ruled the image sensor field for many years thanks to its excellent performance and there are still some specific applications where the CCD is utilized over the CIS. However, thanks to the advantages of system-on-chip (SoC) capability, in addition to the low power consumption, low cost, and the ongoing research in the image sensor field, the CIS has overtaken the CCD over the last few decades [17].

The MOS capacitor is the basis of a CCD. A CCD cell is composed of capacitors connected in series, as shown in Figure 1-1. These capacitors share the same substrate while the other plate is biased by digital pulses [17]. When one of the capacitors of the CCD cell is biased at a certain voltage, an induced potential well is created in the silicon.

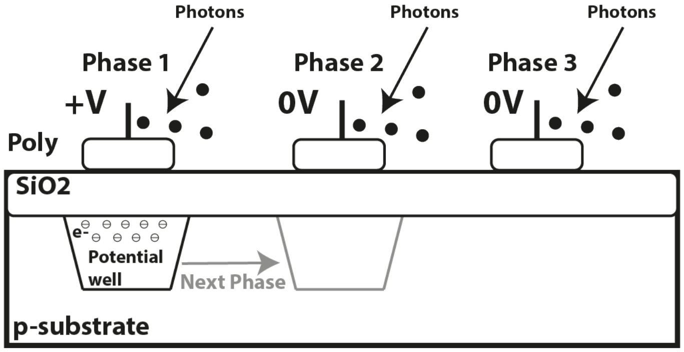

Figure 1-1: CCD architecture. Note: the spacing between the CCD gates has been exaggerated in order to have a clear figure. In fact, the spacing needs to be small in order to have a proper charge transfer.

Photons entering the CCD create electron-hole pairs. The electrons are then attracted to the positive potential where they generate a charge packet. This packet of electrons in the potential well are then continuously passed from one pixel to the neighboring pixel by sequentially biasing the capacitors (different phases) [17], [18], [19]. The charge is converted into a voltage by using an amplifier outside of the pixel area. An off-chip analog-to-digital converter is utilized to digitize the data of the CCD. In terms of performance, signal uniformity and fill factor are two parameters where the CCD shows advantages over CIS devices [17], [20], [21]. In terms of disadvantages, the speed of the CCD is limited by its transfer scheme as well as the considerably high power consumption required to improve the charge transfer efficiency of the pixels [22]. Perhaps the most significant drawback of the CCD is the non-integrability of its SoC due to its incompatibility with a CMOS process. The CCD technology is optimized for imaging (and not for CMOS) and the readout architecture is different than in CMOS (for instance, less flexible readout than random access). In this way, for instance, the readout system must be designed on a different chip, increasing the area, volume and cost of the final product [16], [23].

Although the CIS device was invented almost at the same time as the CCD, its poor sensitivity and deficient noise performance prevented it from developing at the same rate as the CCD. However, with the advances in CMOS process technology and the incorporation of the pinned photodiode, the sensitivity and noise performance greatly improved, ultimately reaching the level of the CCD [16], [24]. Moreover, as the CIS is made in CMOS technology, a SoC can be designed. The CIS can be integrated with: the readout system (column amplifiers, ADCs), digital signal processors, all the necessary periphery circuits (e.g. regulators), reducing thus its cost and power consumption [21]. In terms of performance, its readout speed is increased thanks to the in-pixel amplifier, but at the cost of resolution [25].

The high integrability of the CIS has allowed the size of the resulting cameras to be reduced to the extent that they can be integrated into a mobile phone. However, the high circuitry density of a mobile phone can lead to thermal noise problems in their cameras in the form of dark signal non-uniformity (DSNU), which highly depends on temperature and on the exposure time. Additionally, the lack of a mechanical shutter on the camera of a mobile phone makes it impossible to compensate for dark signal by using a captured dark reference frame. As the dark signal non-uniformity of the pixel array depends on the temperature variations of the chip, the DSNU can be characterized by determining the thermal distribution of the pixel array. The thermal distribution can be measured/characterized by integrated temperature sensors uniformly distributed across the pixel array. Thus, local thermal behavior can be measured and the dark signal level can be locally estimated in the different areas of the pixel array. In this way, the DSNU can be compensated even without the need for a mechanical shutter in the camera.

1.2.2 Temperature Sensors

Temperature sensors have been widely studied and developed. They might be some of the most used sensors in our daily life. They are found in various places, especially in control systems, from coffee machines to heating systems [15]. Thanks to developments in the semiconductor industry, it is also possible to integrate temperature sensors and their readout-processing SoC, resulting in a so-called “smart temperature sensor”. Many smart temperature sensors are based on the well-defined temperature dependence of the base-emitter voltage (V_{BE}) of bipolar transistors. However, a single temperature-dependent signal is not enough to realize a smart temperature sensor because the output signal should be a digital representation of its temperature. In order to achieve this representation, two voltages are required: a voltage that is proportional to absolute temperature (V_{PTAT}) and a temperature-independent reference voltage (V_{REF}). When V_{PTAT} is compared to V_{REF}, a ratiometric measurement is performed.

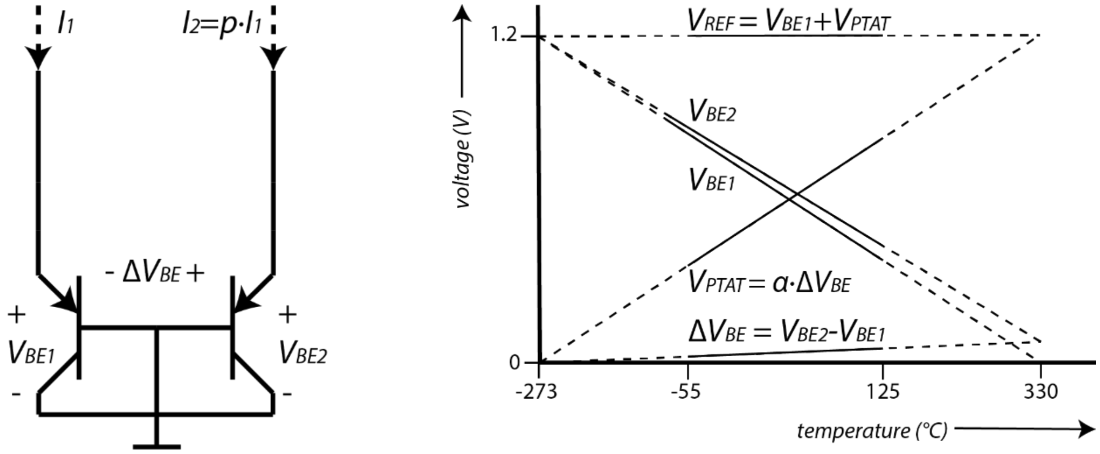

(a) (b)

Figure 1-2: (a) Two pnp BJT transistors biased by a current ratio 1:p. (b) The base-emitter voltages generated by the ratio 1:p are used to generate a PTAT voltage and a voltage reference.

In Figure 1-2 (a) two bipolar transistors are biased with currents in a ratio 1:p generating two base-emitter voltages (V_{BE1} and V_{BE2}). The PTAT voltage is generated from the difference in base-emitter voltage $\Delta V_{BE} = V_{BE2} - V_{BE1}$. However, the sensitivity of ΔV_{BE} is rather small (0.1 – 0.25 mV/K), thus, it needs to be amplified (α) in order to get a useful V_{PTAT}.

The reference voltage is based on the combination of the absolute base-emitter voltage of a bipolar transistor and V_{PTAT}. When the base-emitter voltage is extrapolated to -273 °C (0 K), V_{BE} is equal to the silicon bandgap voltage of about 1.2 V (Figure 1-2 (b)), decreasing by about -2mV/K. In order to compensate the decrease of V_{BE}, an amplified voltage $\alpha \cdot \Delta V_{BE} = V_{PTAT}$ is applied. This results in a voltage reference V_{REF} that is temperature-independent. V_{REF} is nominally equal to the silicon bandgap voltage and it is referred as a bandgap reference.

Various types of temperature sensors have been designed, but what they all have in common is the general-purpose bandgap references. Hilbiber presented the first bandgap reference in 1964 [26], and Widlar then used them in voltage regulators in 1971 [27]. Much of the work on bipolar-based temperature sensors has been done by Meijer [28], who introduced a general-purpose smart temperature sensor in 1989 [29]. Also, work on nMOS-based temperature sensors has been done [30], where the temperature data was obtained by using the differential gate-source voltage (ΔV_{GS}). More recently, research on resistor-based temperature sensors has been carried out [31], [32], reaching accuracies comparable to those of BJT-based ones.

1.3 Motivation and Objectives

The main objective of this thesis is to compensate for the dark signal non-uniformity in a CMOS image sensor by determining the temperature of the pixels and the thermal distribution of the pixel array. To enable the compensation, multiple temperature sensors are placed on the pixel array to locally estimate its temperature and thermal distribution across the pixel array.

The technology offers some alternatives that can be used as temperature sensors: parasitic BJT and nMOS-based temperature sensor. These two types can fulfil one of the constrain regarding the pixel pitch, which is usually in the order of tens micrometres. Also, the pixel's readout offers the opportunity to use correlated double sampling (CDS). CDS cancels the kTC noise produced by the reset action and the offset of the column amplifier. In this way, it becomes natural to use the same readout system for both: the pixels and the temperature sensors. At the same time, cross-talk sensitivity is a topic to be investigated as there is no information in literature about the integration of temperature sensors into the pixel array. All these questions can be targeted as secondary objectives.

The secondary objectives of this thesis are summarized as follows:

- Explore the use of different types of temperature sensors that can be integrated into a pixel array.
- Achieve the same readout system for the pixels and the temperature sensors.
- Apply different techniques to improve the accuracy of the temperature sensors.
- Model the temperature behavior of the dark signal (current) of the pixel array.
- Investigate whether there is cross-talk sensitivity between the temperature sensors and the pixels.
- Propose a dark signal compensation scheme by using the temperature information of the integrated temperature sensors.

1.4 Thesis Outline

This thesis comprises eight chapters, including the introduction. The organization of the chapters is as follows.

Chapter 2 gives a brief overview of two different types of CMOS image sensors (CISs). Also, the most important metrics used to characterize a CIS are defined. An overview of the main sources of noise in the spatial domain as well as the temporal domain is presented.

In Chapter 3, the dark current is analyzed, with an explanation of how the dark signal is generated in the pixel. The different sources of dark current are explained in this chapter. Also, the dependence on the exposure time and the temperature behavior are presented.

In Chapter 4, the integration of a BJT-based temperature sensor into the pixel array is described. These temperature sensors use the same readout system as pixels, and therefore measurements of a test chip prove the feasibility of integrating temperature sensors. Cross-talk sensitivity between the pixels and the bipolars is shown in this chapter as well.

In Chapter 5, the focus is on the use of the nMOS source follower (SF) transistor as a temperature sensor. A comparison is also made between the SF temperature sensor and the BJT-based one. Different techniques to improve the accuracy of both types of temperature sensors are discussed in this chapter. Measurements of a test chip prove the capability of both temperature sensors.

Chapter 6 presents a detailed analysis of the cross-talk sensitivity between pixels and BJT-based temperature sensors. Photon generation and/or hot carriers are believed to be the main causes of this cross-talk.

Chapter 7 proposes a scheme to compensate for dark current by using in-pixel temperature sensors. Different levels of compensation are reached depending on the type of temperature sensor used.

Chapter 8 provides the main conclusions of this thesis. Main contributions, findings, and future work are presented.

References

[1] G. Busch, "Early history of the physics and chemistry of semiconductors-from doubts to fact in a hundred years," *European Journal of Physics,* vol. 10, no. 4, pp. 254-264, 1989.

[2] B. G. Yacobi, *Semiconductor materials: an introduction to basic principles*. Springer Science & Business Media, 2003, pp. 135-170.

[3] J. Dabrowski, *Silicon surfaces and formation of interfaces: basic science in the industrial world*. World Scientific, 2000, pp. 344-346.

[4] P. Siffert and E. Krimmel, *Silicon: Evolution and future of a technology*. Springer Science & Business Media, 2013, pp. 26-28.

[5] M. M. Atalla, E. Tannenbaum, and E. J. Scheibner, "Stabilization of silicon surfaces by thermally grown oxides," *The Bell System Technical Journal,* vol. 38, no. 3, pp. 749-783, 1959.

[6] Y. J. Chabal, *Fundamental Aspects of silicon oxidation*. Springer Science & Business Media, 2012, pp. 35-60.

[7] C.-T. Sah, "Evolution of the MOS transistor-from conception to VLSI," *Proceedings of the IEEE,* vol. 76, no. 10, pp. 1280-1326, 1988.

[8] P. Tréguer, D. M. Nelson, A. J. Van Bennekom, D. J. DeMaster, A. Leynaert, and B. Quéguiner, "The Silica Balance in the World Ocean: A Reestimate," *Science,* vol. 268, no. 5209, p. 375, 1995.

[9] W. Shockley, "The path to the conception of the junction transistor," *IEEE Transactions on Electron Devices,* vol. 23, no. 7, pp. 597-620, 1976.

[10] J. S. Kilby, "Invention of the integrated circuit," *IEEE Transactions on Electron Devices,* vol. 23, no. 7, pp. 648-654, 1976.

[11] S. E. Thompson and S. Parthasarathy, "Moore's law: the future of Si microelectronics," *Materials Today,* vol. 9, no. 6, pp. 20-25, 2006.

[12] S. Ay, M. Lesser, and E. Fossum, "CMOS Active Pixel Sensor (APS) imager for scientific applications," in *Astronomical Telescopes and Instrumentation*, 2002, vol. 4836, pp. 271-278.

[13] M. Schanz, C. Nitta, A. Bussmann, B. J. Hosticka, and R. K. Wertheimer, "A high-dynamic-range CMOS image sensor for automotive applications," *IEEE Journal of Solid-State Circuits,* vol. 35, no. 7, pp. 932-938, 2000.

[14] A. E. Gamal and H. Eltoukhy, "CMOS image sensors," *IEEE Circuits and Devices Magazine,* vol. 21, no. 3, pp. 6-20, 2005.

[15] M. A. P. Pertijs and J. H. Huijsing, *Precision temperature sensors in CMOS technology*. Springer, 2006, pp. 1-10.

[16] D. Durini, *High performance silicon imaging: fundamentals and applications of cmos and ccd sensors*. Woodhead Publishing, 2019, pp. 37-53.

[17] A. J. P. Theuwissen, "CCD or CMOS image sensors for consumer digital still photography?," in *2001 International Symposium on VLSI Technology, Systems, and Applications. Proceedings of Technical Papers*, 2001, pp. 168-171.

[18] W. S. Boyle and G. E. Smith, "Charge coupled semiconductor devices," *The Bell System Technical Journal,* vol. 49, no. 4, pp. 587-593, 1970.

[19] J. B. Williams, *The electronics revolution: inventing the future*. Springer, 2017, pp. 245-246.

[20] C. Huang, "Future development for thinned back-illuminated CCD imager devices," in *Prog. IEEE Charge-Coupled Devices Workshop*, 1991.

[21] E. R. Fossum and D. B. Hondongwa, "A review of the pinned photodiode for CCD and CMOS image sensors," *IEEE Journal of the electron devices society,* vol. 2, pp. 33-43, 2014.

[22] C. Seibold, "Comparison of cmos and ccd image sensor technologies," *Proceeding of IEEE Sensor Council,* vol. 1, pp. 171-176, 2002.

[23] B. S. Carlson, "Comparison of modern CCD and CMOS image sensor technologies and systems for low resolution imaging," in *IEEE SENSORS*, 2002, vol. 1, pp. 171-176.

[24] E. Fossum, "Active pixel sensors: are CCDs dinosaurs?," in *Symposium on Electronic Imaging: Science and Technology*, 1993, vol. 1900, pp. 2-14.

[25] E. R. Fossum, "CMOS image sensors: electronic camera-on-a-chip," *IEEE Transactions on Electron Devices,* vol. 44, no. 10, pp. 1689-1698, 1997.

[26] D. Hilbiber, "A new semiconductor voltage standard," in *IEEE International Solid-State Circuits Conference. Digest of Technical Papers*, 1964, vol. 4, pp. 32-33.

[27] R. J. Widlar, "New developments in IC voltage regulators," *IEEE Journal of Solid-State Circuits,* vol. 6, no. 1, pp. 2-7, 1971.

[28] G. C. Meijer, "Integrated circuits and components for bandgap references and temperature transducers," Ph.D. Dissertation, Delft University of Technology, pp. 25-52, 1982.

[29] G. Meijer, R. Van Gelder, V. Nooder, J. Van Drecht, and H. Kerkvliet, "A three-terminal intergrated temperature transducer with microcomputer interfacing," *Sensors and Actuators,* vol. 18, no. 2, pp. 195-206, 1989.

[30] K. Souri and K. A. Makinwa, *Energy-Efficient Smart Temperature Sensors in CMOS Technology*. Springer, 2017, pp. 91-108.

[31] S. Pan, Y. Luo, S. H. Shalmany, and K. A. A. Makinwa, "A Resistor-Based Temperature Sensor With a 0.13 pJ · K2 Resolution FoM," *IEEE Journal of Solid-State Circuits,* vol. 53, no. 1, pp. 164-173, 2018.

[32] J. A. Angevare and K. A. A. Makinwa, "A 6800-μm2 Resistor-Based Temperature Sensor With ±0.35 °C (3σ) Inaccuracy in 180-nm CMOS," *IEEE Journal of Solid-State Circuits,* vol. 54, no. 10, pp. 2649-2657, 2019.

2 CMOS IMAGE SENSOR

In this chapter an overview of the most important aspects of a CMOS image sensor is presented. In Section 2.1 the 3T and 4T pixel architectures are described. Then, the most representative metrics to characterize an image sensor are discussed in Section 2.2. Finally, in Section 2.3 noise in image sensors is examined.

2.1 Pixel Architecture

Pixels based on CMOS technology fall into two categories: passive pixel sensors (PPSs) and active pixel sensors (APSs). The PPS consists of a photodiode (PD) and a transistor acting as a switch (RS). Column amplifiers read the output signal of a passive pixel, as shown in Figure 2-1 (RST: reset; VREF: reference voltage). One of the main characteristics of the PPS is its high fill factor (Section 2.2.2) due to the presence of only one in-pixel transistor. On the other hand, the PPS suffers from considerable readout noise because of the substantial loading capacitance [1]. Another source of noise is the kTC noise introduced by the reset action (Section 2.3.1.3). The photodiode is reset after each light exposure, introducing kTC noise when the junction capacitance of the photodiode is charged to the reset voltage [2]. Also, the photogenerated charge of the PPS is susceptible to noise injection between the pixel output and the charge detection amplifier [3].

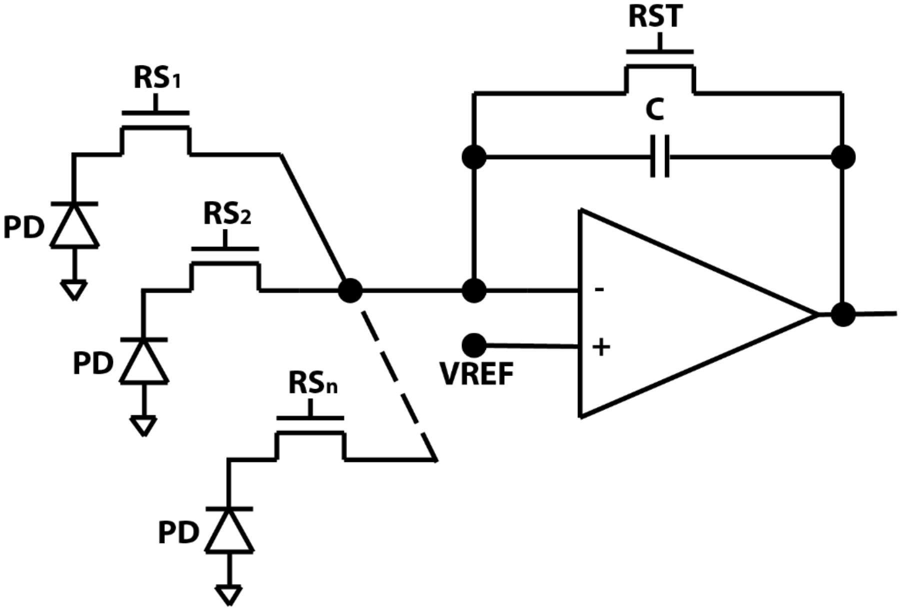

Figure 2-1: Schematic of the passive pixel.

The noise injection issue can be overcome by using an in-pixel source follower acting as a buffer between the photodiode and the readout bus [3]. The kTC noise also affects the APS, but compared to the PPS, the kTC noise can be canceled by using the correlated double sampling technique. Cross-talk is another source of noise that affects both the PPS and APS. Cross-talk refers to the charge exchange between neighboring pixels. This problem can be reduced by using deep trench isolation (DTI), which can be seen as “walls” to isolate neighboring pixels across the array [4], [5]. In this way, cross-talk is highly reduced. Another design technique is the creation of a deep p-well photodiode to prevent the diffusion of electrons from pixel to pixel [6].

The main difference between the PPS and the APS is the presence of an extra transistor in the pixel itself. The APS offers lower noise and higher readout speeds compared to the PPS. These features make the APS the preferred architecture for pixel design. In the following sections, the two main APS architectures will be introduced.

2.1.1 3T Pixel Architecture

The 3T pixel architecture consists of three in-pixel transistors and a p-n junction photodiode (PD) that functions as the light-sensitive area of the pixel. The three transistors of the in-pixel readout circuit are represented in Figure 2-2 by: the reset transistor (RST), the source follower (SF), and the row select (RS). Figure 2-2 shows the configuration of the 3T pixel, where the VDD_RST corresponds to the reset voltage of the photodiode, VDD_SF is the voltage supply of the SF, RST corresponds to the reset transistor, PD stands for the photodiode, RS corresponds to the row select transistor, PIX_OUT is the output signal of the pixel, and I_{bias} corresponds to the bias current of the source follower (shared by the pixels at the column level).

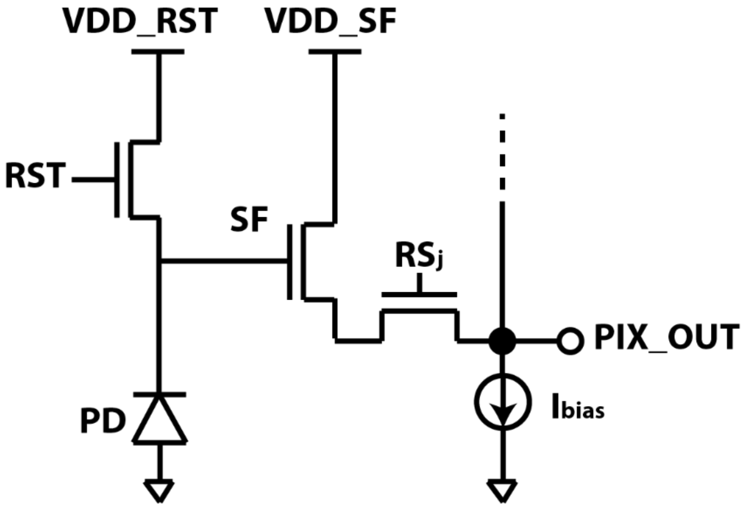

Figure 2-2: 3T pixel architecture.

In this case the photodiode has a double function: it collects the photon-generated electrons, and converts the charge into voltage. Then, this voltage signal is read by the SF before being read out through the RS transistor. Before the next light exposure, the photodiode is reset to VDD_RST when the RST is on.

Compared to other APSs, the 3T pixel has a higher fill factor (Section 2.2.2) due to the presence of fewer transistors. In terms of noise cancelation, the offset of the source follower and most of the flicker noise (Section 2.3.1.5) of the source follower can be canceled by using double data sampling (DDS). This method samples the signal generated in the photodiode just before the reset of the photodiode and the signal just after the reset, after which both signals are subtracted, thus cancelling the offset and the flicker noise. However, the kTC noise introduced by the reset action cannot be easily cancelled (as in the case of the 4T pixel) because the sampling of the noise and video signals are non-correlated in this type of pixel. The non-correlation exists because the reset operation takes place between the two samples. Sampling before and after the reset results in non-correlated noise. Also, the dark current can be larger than that of a 4T pixel because the photodiode has direct contact with the silicon-silicon oxide interface [2].

2.1.2 4T Pixel Architecture

A 4T pixel is composed of the same three transistors (RST, SF, and RS), as a 3T pixel, but with the addition of an extra transistor called a transfer gate (TG). The TG is added between the pinned photodiode (PPD) and the floating diffusion (FD). In addition to using an extra transistor (TG), the photodiode (of the 3T pixel) is replaced by a pinned photodiode in the 4T architecture. The PPD was first introduced as the photo-sensing part of a CCD to enable a complete charge transfer from the photodiode [7]. A schematic of the 4T pixel is shown in Figure 2-3.

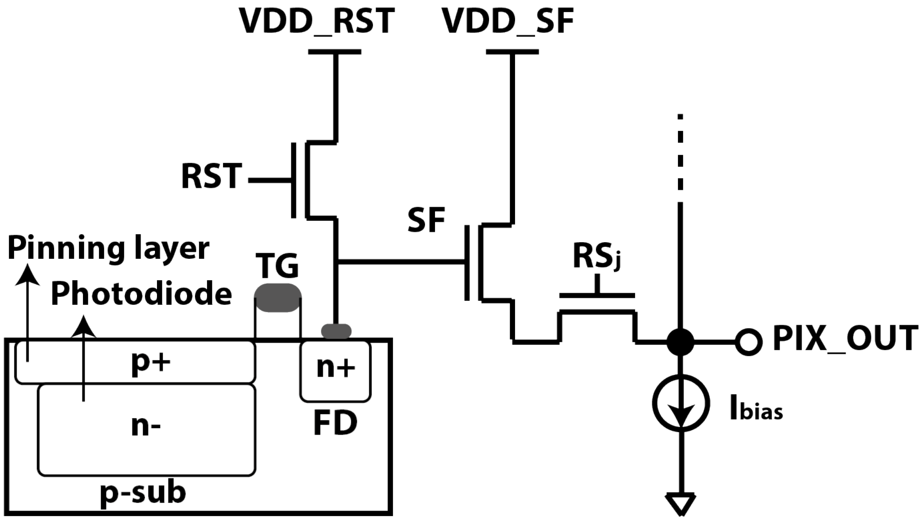

Figure 2-3: 4T pixel architecture.

The VDD_RST corresponds to the reset voltage of the FD node, VDD_SF is the voltage supply of the SF, RST corresponds to the reset transistor, TG stands for the transfer gate, FD is the floating diffusion, SF corresponds to the source follower transistor, RS corresponds to the row select transistor, PIX_OUT is the output signal of the pixel, and I_{Ibias} corresponds to the bias current of the SF (shared by the pixels at the column level).

The p+n-p-sub structure of the PPD compared to the n-p- junction of the PD has an extra p+ layer at the surface that was proposed by [7] to solve the transfer lag and kTC noise problems. This structure is used in almost every CCD and CIS [8]. One of the main characteristics of the PPD is the low dark current at the surface, mostly suppressed by the presence of the p+ layer [9]. Both the p+ and p- layers are connected to the same substrate voltage. This substrate voltage is usually at ground level but it has been shown in [10] that applying a negative voltage to the substrate extends the full well capacity (Section 2.2.4).

Another important feature of the 4T pixel is that the PPD-TG-FD structure allows real correlated double sampling (CDS) [11] due to the decoupling of the reset and readout operation from the integration period. This technique samples each pixel signal twice: first right after the reset operation, and then at the end of the charge transport from the photodiode to the floating diffusion node. Next, both signals are subtracted to remove the offset caused by the mismatch of the transistors. CDS cancels the kTC noise introduced by the reset action [12], reducing the dark temporal noise of the pixel. The remaining noise mostly comes from the SF transistor as 1/f and Johnson noise [13], [14].

Another feature of the 4T pixel is that its electron-to-voltage conversion gain (Section 2.2.6) has a higher value than that of a 3T pixel due to the existence of a small integration capacitor on the FD node, which increases the value of the conversion gain [15], [16].

2.2 Metrics

In this section important metrics that characterize a CMOS image sensor will be discussed.

2.2.1 Dark Current

Dark current corresponds to the signal response of the photodiode in the absence of light. In normal operation of the pixel (with light), dark current is part of the output signal, but it might not be as noticeable as in the absence of light. Dark current depends on exposure time and temperature. It directly affects the dynamic range and signal-to-noise ratio. A more complete definition of dark current, along with its different sources, how it varies with exposure time and temperature, and techniques to cancel it, will be discussed in Chapter 3.

2.2.2 Fill Factor

The fill factor (FF) refers to the ratio between the light-sensitive area of the pixel and the total area of the pixel. The light-sensitive area consists of the photodiode of the pixel, whereas the total area of the pixel is composed of the photodiode plus the in-pixel transistors (e.g. reset transistor, source follower, row select). The FF is defined by Equation (2-1):

$$FF = \frac{A_{PD}}{A_{pixel}} \tag{2-1}$$

where A_{PD} corresponds to the light-sensitive area, and A_{pixel} is the total area of the pixel.

A higher FF corresponds to a more sensitive pixel, which can collect more photons. Backside illumination (BSI) offers a higher FF than front-side illumination pixels because the light-sensitive area is placed on one side of the silicon substrate, occupying the total pixel area, with the electronics on the other side of the silicon substrate. In theory, BSI could offer a 100% FF [17].

2.2.3 Quantum Efficiency and Responsivity

Quantum efficiency (QE) refers to the capacity of a pixel to convert photons arriving at the photodiode surface into an electron-hole pair. The QE is defined by Equation (2-2):

$$QE(\lambda) = \frac{N_{\bar{e}}(\lambda)}{N_{ph}(\lambda)} \tag{2-2}$$

where $N_{\bar{e}}$ stands for the number of electrons generated in the light-sensitive area, N_{ph} corresponds to the number of photons reaching the pixel, and λ is the wavelength.

QE should ideally be 1, meaning that each photon generates one electron-hole pair and the pixel collects the generated electron. In practice, this is never the case because there is some loss in the system. One type of loss is the result of reflection at the interface of the photodetector.

Also, some electron-hole pairs recombine at both the SiO2-Si interface and outside of the depletion layer. There is photon loss as well, as not all photons reach or are absorbed by the silicon [18].

The responsivity (R) is another light metric which is closely related to QE. It is defined as the ratio between the photocurrent and optical input power [19]. Equation (2-3) defines R:

$$R(\lambda) = \frac{I_{ph}}{P} = \frac{qN_{\bar{e}}(\lambda)}{E_{ph}N_{ph}(\lambda)} = QE(\lambda)\frac{q\lambda}{hc} \tag{2-3}$$

where I_{ph} is the photocurrent, P is the input light power, q corresponds to the fundamental electric charge, E_{ph} stands for the photon energy, h corresponds to the Planck constant, and c is the speed of light.

The QE (and R) can be improved by implementing different geometries to maximize the ratio between the photodiode and the total pixel area (this ratio corresponds to the fill factor, Section 2.2.2). Changing the doping concentration of the photodetector also improves the QE. Furthermore, the collection loss can be reduced by designing the depletion region of the photodiode to be wide and deep [20]. Also, a carefully designed microlens increases the QE.

2.2.4 Full Well Capacity

The full well capacity (FWC) of an imager is defined as the maximum amount of charge that the photodiode is able to store before saturation when there is no limitation of the readout circuit [21]. As the FWC defines the saturation level, it also highly influences the dynamic range of the system. The FWC is given by Equation (2-4) [22]:

$$FWC = \frac{1}{q}\int_{V_{MIN}}^{V_{MAX}} C_{PD}(V) \cdot dV \tag{2-4}$$

where V_{MAX} is the saturation voltage, V_{MIN} corresponds to the minimum photodiode potential [23], and C_{PD} is the capacitance of the PD.

Efforts to extend the saturation level of the FWC include integrating a lateral overflow integration capacitor (LOFIC) that overrides the limitations of the photodiode or the floating diffusion FWC [24].

Temperature also influences the value of the FWC. For instance, it has been shown in [23], [25] that the FWC increases with temperature due to the dependency of the FWC on the pinning voltage (the pinning voltage is temperature dependent) [23].

2.2.5 Dynamic Range and Signal-to-Noise Ratio

The dynamic range (DR) and the signal-to-noise ratio (SNR) are both metrics of the capacity of the sensor which measure a certain signal level in comparison to the noise level.

The DR corresponds to the ratio between the saturation level and the dark noise level. The DR is defined by Equation (2-5):

$$DR = 20log\left(\frac{N_{sat}}{n_{dark}}\right) \tag{2-5}$$

where N_{sat} is the pixel saturation level (also known as full well capacity, Section 2.2.4), and n_{dark} corresponds to the total noise level in dark. To increase the DR, either the saturation level must be increased, or the dark-noise level must be reduced.

The SNR is defined as the ratio between the output signal of the sensor at a specific input signal and the corresponding total noise of the output signal. The SNR is given by Equation (2-6):

$$SNR = 20log\left(\frac{N_{sig}}{n_{sig}}\right) \tag{2-6}$$

where N_{sig} is the output signal level, and n_{sig} corresponds to the total noise at that output signal level.

2.2.6 Conversion Gain

An amount of charge is generated by the incoming light and is collected by the photodiode. The amount of charge can be expressed in electrons, but the output signal of the sensor is expressed as an analog voltage (for CCDs) or as a digital number (DN) (for CMOS image sensors). The conversion gain (CG), which is the parameter that relates both units (electrons and voltage/DN), is used to convert from one unit to the other (and vice versa). In general, the conversion gain is defined as the amount of voltage produced by one electron. The CG is given by Equation (2-7):

$$CG = \frac{q}{C_{FD}} \cdot A \tag{2-7}$$

where C_{FD} is the capacitance of the floating diffusion, and A is the gain of the in-pixel buffer (in the case of the 4T pixel, this buffer corresponds to the source follower).

In [25] the temperature dependence of the CG is analysed in terms of the C_{FD} and A_{SF} (gain of the source follower), where the capacitance of the floating diffusion increases its value with temperature while the gain of the source follower decreases its value with temperature. Thus, the value of the CG decreases when the temperature increases. The temperature behavior of the CG has been measured in [25], [26].

2.3 Sources of Noise in Image Sensors

In image sensors there are different sources of noise, some of which depend on the pixel itself (physical properties, material), while others are related to the electronics (source follower, amplifiers), and photon shot noise that is related to a random natural process. These noise sources are divided into two categories: temporal noise and spatial noise. At the same time, the contributors of temporal noise are photon shot noise, dark shot noise, reset noise, thermal noise, and flicker noise. On the other hand, spatial noise is divided into Dark Signal Non-Uniformity (DSNU), also called Fixed Pattern Noise (FPN) in dark, and Photon Response Non-Uniformity (PRNU), also called FPN in light.

2.3.1 Temporal Noise

The term temporal noise refers to a type of noise that depends on the time between images or frames. In other words, it is the variation in the pixel (or image sensor) response taken at different times but using the same light input. In the following sections the main sources of temporal noise will be defined.

2.3.1.1 Photon Shot Noise

Shot noise can be either photon shot noise or dark shot noise, but in both cases the phenomenon behind it follows the same idea of randomness. Photon shot noise arises with the random arrival of the light packets or photons at the pixel light-sensitive area. The photon shot noise follows a Poisson distribution [27]. The magnitude of the photon shot noise is shown in Equation (2-8):

$$n_{psn} = \sqrt{N_{sig}} \tag{2-8}$$

where n_{psn} corresponds to the photon shot noise, and N_{sig} is the output signal produced by the mean number of stored electrons in the light-sensitive area [18].

One unique characteristic of the photon shot noise is the possibility of deriving the conversion gain if the photon shot noise dominates the readout noise level. If the conversion gain is used to express n_{psn} in voltage, the following equation is obtained:

$$V_{psn} = CG\sqrt{N_{sig}} \tag{2-9}$$

where V_{psn} corresponds to the photon shot noise expressed as voltage.

The output signal can be also expressed as voltage by using the CG:

$$V_{sig} = CG \cdot N_{sig} \tag{2-10}$$

where V_{sig} is the output signal in voltage. By combining Equations (2-9) and (2-10), the conversion gain can be expressed as:

$$CG = \frac{V_{psn}^2}{V_{sig}} \tag{2-11}$$

2.3.1.2 Dark Shot Noise

In the case of dark shot noise, the output signal is generated through thermal excitation of the electrons only. An electron-hole pair can be generated while the pixel light-sensitive area is in complete darkness. Dark shot noise relates to dark current, as shown in Equation (2-12):

$$n_{dc} = \sqrt{N_{dc}} \tag{2-12}$$

where n_{dc} is the dark shot noise, and N_{dc} is the mean value of dark current in electrons.

2.3.1.3 Reset Noise

In a 4T pixel the PPD is reset by a voltage equal to or higher than the pinning voltage preceding each subsequent light exposure. This reset procedure is done by the reset transistor (Figure 2-3). However, this transistor acts as a resistor during the "on" phase, adding some thermal noise to the signal. This results in kTC noise on the floating diffusion after the reset. In [18], the reset noise is expressed by (2-13):

$$V_{res} = \sqrt{\frac{kT}{C_{FD}}} \tag{2-13}$$

where V_{res} is the reset noise in terms of voltage, k is the Boltzmann constant, T corresponds to absolute temperature, and C_{FD} is the capacitance of the floating diffusion.

The kTC noise can be canceled by using a CDS circuit. This property is one of the main features differentiating a 4T pixel from a 3T pixel architecture.

2.3.1.4 Thermal Noise

The pixel chain is composed of many electronic components such as transistors, capacitors, and resistors, all of which are temperature-dependent. Thermal noise refers to the excitation of electrons as a result of thermal agitation [28], [29]. This random motion of the electrons in the conductor results in a noisy output signal from the system [28].

2.3.1.5 Flicker Noise 1/f

Flicker noise is frequency-dependent and it is mainly caused by traps present at the surface and the bulk in the transistor channel. The charge carriers present in the channel of the transistor interact with these traps in a random way producing random current variations along the channel [30]. Flicker noise is inversely proportional to the frequency, which means that this noise becomes more important at low frequencies, while its influence diminishes at high frequencies where the thermal noise becomes predominant. In [31], flicker noise follows Equation (2-14):

$$\overline{V_n^2} = \frac{K}{C_{ox}WL} \cdot \frac{1}{f} \tag{2-14}$$

where $\overline{V_n^2}$ is the flicker noise power, K depends on the process, C_{ox} is the oxide gate capacitance, W and L are the width and length of the transistor, respectively, and f corresponds to the frequency.

2.3.2 Spatial Noise or Fixed Pattern Noise

Spatial noise refers to the variation in the output signal between different pixels when they are under constant illumination (or darkness). FPN is fixed for a given sensor but it varies between different sensors of the same batch. CMOS image sensors have higher FPN than CCDs because in CISs the in-pixel transistors and column amplifiers (column FPN) add extra noise to the pixel FPN. In CCDs, the pixels share the same output amplifier avoiding the column FPN. The main sources of FPN are the dark current generated inside the pixel and the mismatch of the transistors involved in the sensor design.

There are two types of spatial noise: FPN in dark (also called DSNU); and FPN in light (also called PRNU).

2.3.2.1 Fixed Pattern Noise in Dark

FPN in dark is seen as a different DC offset added to the output signal of each pixel. In a CIS under complete darkness condition, the main causes of FPN in dark are the in-pixel variations and the readout variations (column level).

The in-pixel variations are based on the photodetector fluctuations (such as area), dark current, and the in-pixel transistor mismatch. In the case of a 3T and a 4T pixel, the impurities added during the fabrication process induce mismatch in the transistor parameters such as the threshold voltage of the different transistors involved in the readout system.

The non-uniformity caused by the in-pixel transistors can be completely removed by using the correlated double sampling technique [11], [32].

Dark current is the main source of FPN generated inside the pixel. Under no light conditions, dark current is present, and it depends on the exposure time and temperature. It is difficult to remove this noise because the dark current is not uniform between pixels along the array, making it necessary to know the exact value of the dark current for every pixel.

Column amplifiers also suffer from mismatch causing non-uniformity in the column output signals. This non-uniformity, which is very typical in CMOS image sensors, can be clearly seen in the output image. The noise appears as stripes in the final image. It can be canceled by applying circuit techniques, such as in [33], where a dynamic column FPN reduction technique is used in column-level ADCs. These days, the cancelation of column FPN is mainly done on-chip rather than with off-chip image post-processing.

2.3.2.2 Fixed Pattern Noise in Light

FPN in light appears under constant, uniform illumination and in contrast to FPN in dark, it does not manifest as an offset but as gain FPN proportional to light [18]. This FPN is mainly due to the photon-response gain mismatch of the different pixels. It can also include FPN in dark, but if the image is taken at a short exposure time with a lot of light then the FPN in dark becomes negligible.

The light-sensitive area of the pixel itself affects the collection of light. Pixels are not exactly equal; thus, they react/convert light in a different way depending on the real size of the light-sensitive area. As in the case of dark conditions, the circuitry mismatch also induces differences pixel-by-pixel.

The camera can also contribute to FPN in light by means of the difference in light intensity produced by, for instance, the lens of the camera.

One way to cancel or diminish FPN in light is by means of gain calibration of each pixel along the array. If the exact gain per pixel is known and one gain is used as a reference, the noise can be compensated by properly correcting the gain of each pixel [18].

2.4 Conclusions

In this chapter, the difference between a passive pixel and active pixel has been presented, focusing on active 3T and 4T pixel architectures. The 4T pixel architecture is widely used because of its excellent performance. One of the main characteristics of the 4T pixel is the use of the PPD-TG-FD structure, which allows the cancelation of reset noise by using the correlated double sampling technique. In this thesis, the 4T pixel architecture is used for CMOS image sensor design.

The main performance metrics and noise sources of the CMOS image sensor have been defined. Special attention will be devoted to dark current in Chapter 3.

References

[1] G. P. Weckler, "Operation of pn junction photodetectors in a photon flux integrating mode," *IEEE Journal of Solid-State Circuits,* vol. 2, no. 3, pp. 65-73, 1967.

[2] G. Meijer, K. Makinwa, and M. Pertijs, *Smart sensor systems: Emerging technologies and applications*. John Wiley & Sons, 2014, pp. 173-189.

[3] J. Nakamura, *Image Sensors and Signal Processing for Digital Still Cameras*. Taylor & Francis Inc, 2005, pp. 153-159.

[4] B. J. Park *et al.*, "Deep trench isolation for crosstalk suppression in active pixel sensors with 1.7 µm pixel pitch," *Japanese journal of applied physics,* vol. 46, pp. 2454–2457, 2007.

[5] A. Tournier *et al.*, "Pixel-to-pixel isolation by deep trench technology: Application to CMOS image sensor," in *Proc. Int. Image Sensor Workshop*, 2011, pp. 12-15.

[6] M. Furumiya *et al.*, "High-sensitivity and no-crosstalk pixel technology for embedded CMOS image sensor," *IEEE Transactions on Electron Devices,* vol. 48, no. 10, pp. 2221-2227, 2001.

[7] N. Teranishi, A. Kohono, Y. Ishihara, E. Oda, and K. Arai, "No image lag photodiode structure in the interline CCD image sensor," in *1982 International Electron Devices Meeting*, 1982, pp. 324-327.

[8] Y. Xu, "Fundamental characteristics of a pinned photodiode CMOS pixels," Delft University of Technology, pp. 15-27, 2015.

[9] E. R. Fossum and D. B. Hondongwa, "A review of the pinned photodiode for CCD and CMOS image sensors," *IEEE Journal of the electron devices society,* vol. 2, pp. 33-43, 2014.

[10] C. C.-M. Liu *et al.*, "6.8 A 1.5 V 33Mpixel 3D-stacked CMOS image sensor with negative substrate bias," in *2016 IEEE International Solid-State Circuits Conference*, pp. 124-125, 2016.

[11] M. H. White, D. R. Lampe, F. C. Blaha, and I. A. Mack, "Characterization of surface channel CCD image arrays at low light levels," *IEEE Journal of Solid-State Circuits,* vol. 9, no. 1, pp. 1-12, 1974.

[12] M. Tabet, "Double sampling techniques for CMOS image sensors," Ph.D. Dissertation, University of Waterloo, pp. 31-50, 2002.

[13] B. Pain, T. Cunningham, B. Hancock, C. Wrigley, and C. Sun, "Excess noise and dark current mechanisms in CMOS imagers," in *IEEE Workshop on CCD's and Advanced Image Sensors*, 2005, pp. 145-148.

[14] J. Y. Kim *et al.*, "Characterization and improvement of random noise in 1/3.2" UXGA CMOS image sensor with 2.8 um pixel using 0.13 um-technology," in *IEEE Workshop on CCD's and Advanced Image Sensors*, 2005, pp. 149-152.

[15] F. Wang, "Linearity Research of A CMOS Image Sensor," Ph.D. Dissertation, Delft University of Technology, pp. 11-29, 2018.

[16] N. Xie, "Low-Power Low-Noise CMOS Imager Design: in Micro-Digital Sun Sensor Application," Ph.D. Dissertation, Delft University of Technology, pp. 13-25, 2012.

[17] J. Tower *et al.*, "BSI Low Light Level CMOS Image Sensor Employing P-type Pixel," in *International Image Sensor Workshop*, 2013, pp. 5-8.

[18] X. Wang, "Noise in sub-micron CMOS image sensors," Ph.D. Dissertation, Delft University of Technology, pp. 13-41, 2008.

[19] A. J. Theuwissen, *Solid-state imaging with charge-coupled devices*. Springer Science & Business Media, 2006, pp. 324-327.

[20] R. Hui, "Photodetectors," in *Introduction to Fiber-Optic Communications*: Elsevier, 2020, pp. 125-154.

[21] B. Mheen, Y.-J. Song, and A. J. P. Theuwissen, "Negative offset operation of four-transistor CMOS image pixels for increased well capacity and suppressed dark current," *IEEE electron device letters,* vol. 29, no. 4, pp. 347-349, 2008.

[22] A. Pelamatti, V. Goiffon, M. Estribeau, P. Cervantes, and P. Magnan, "Estimation and modeling of the full well capacity in pinned photodiode CMOS image sensors," *IEEE electron device letters,* vol. 34, no. 7, pp. 900-902, 2013.

[23] A. Pelamatti *et al.*, "Temperature dependence and dynamic behavior of full well capacity in pinned photodiode CMOS image sensors," *IEEE Transactions on Electron Devices,* vol. 62, no. 4, pp. 1200-1207, 2015.

[24] K. Mizobuchi *et al.*, "4.5 μm pixel pitch 154 ke- full well capacity CMOS image sensor," in *Proc. Int. Image Sensor Workshop*, 2009, pp. 101-104.

[25] F. Wang and A. J. P. Theuwissen, "Temperature effect on the linearity performance of a CMOS image sensor," *IEEE Sensors Letters,* vol. 2, no. 3, pp. 1-4, 2018.

[26] S. Xie and A. Theuwissen, "Compensation for Process and Temperature Dependency in a CMOS Image Sensor," *Sensors,* vol. 19, no. 4, pp. 870-870, 2019.

[27] J. R. Janesick, T. Elliott, S. Collins, M. M. Blouke, and J. Freeman, "Scientific charge-coupled devices," *Optical Engineering,* vol. 26, no. 8, pp. 35-45, 1987.

[28] B. Carter, "Op Amp Noise Theory and Applications," in *Op Amps for Everyone*: Elsevier, 2009, pp. 163-188.

[29] R. Perez, "Noise and Interference Issues in Analog Circuits," in *Wireless Communications Design Handbook*: Elsevier, 1998, pp. 52-102.

[30] A. L. McWhorter and others, "1/f noise and related surface effects in germanium," Ph.D. Dissertation, Massachusetts Institute of Technology, pp. 69-88, 1955.

[31] B. Razavi, *Design of analog CMOS integrated circuits*. McGrawHill, 2001, pp. 30-40.

[32] A. El Gamal and H. Eltoukhy, "CMOS image sensors," *IEEE Circuits and Devices Magazine,* vol. 21, no. 3, pp. 6-20, 2005.

[33] M. F. Snoeij, A. J. P. Theuwissen, K. A. A. Makinwa, and J. H. Huijsing, "A CMOS imager with column-level ADC using dynamic column fixed-pattern noise reduction," *IEEE Journal of Solid-State Circuits,* vol. 41, no. 12, pp. 3007-3015, 2006.

3 DARK CURRENT ANALYSIS

One of the main components of fixed pattern noise (FPN) in dark is dark current non-uniformity generated inside the pixel, along the pixel array. This non-uniformity (in addition to the mismatch of in-pixel and/or column-level transistors) is expressed as the FPN in dark. The dark current is seen as an offset signal of the pixel generated under no light conditions. Although the dark current is not noticeable under normal illumination, it becomes of relevance when images require long exposure times under low light conditions or images taken during high temperature operations. The dark current limits the full well capacity reducing the dynamic range of the image sensor.

In this chapter, the physical mechanisms of dark current generation will be explained in Section 3.1. The time and temperature dependence will be presented in Sections 3.2 and 3.3, respectively. Finally, the conclusion of this chapter will be presented in Section 3.4.

3.1 Generation of Dark Current

There are three ways to recognize the source of dark current generated inside an n+/p-junction: depletion dark current due to free minority carriers generated in the depletion region; diffusion dark current due to dark carriers generated in the neutral bulk and diffused towards the depletion region; and the presence of carrier generation centers at the Si-SiO_2 boundary [1], [2]. Figure 3-1 shows the n+/p- junction and the places where dark current is generated.

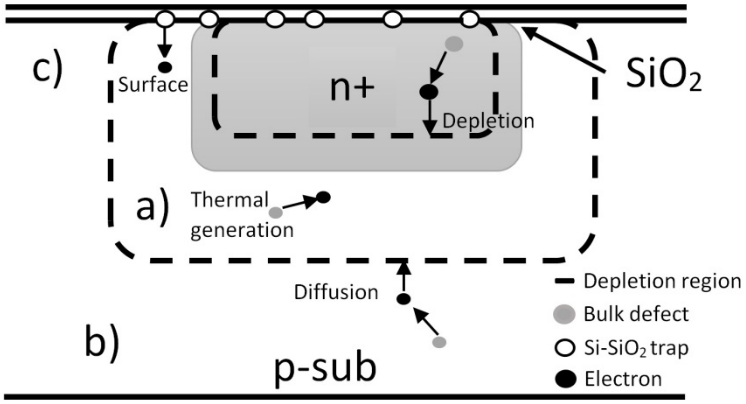

Figure 3-1: Generation of dark current [1], [3]. a) Depletion dark current. b) Diffusion dark current. c) Surface dark current.

3.1.1 Depletion Dark Current

It is known that silicon is an indirect bandgap semiconductor where the dominant generation-recombination process occurs through defects (energy states) located in the silicon bandgap [4], [5]. Extra energy must be provided to an electron for it to pass from the valence band to the conduction band through one of these energy states. Under dark conditions, this extra energy is provided by thermal excitation.

In a zero-biased p-n junction the generation process and recombination process are at complete equilibrium. In an image sensor, the p-n junction of the photodiode is normally reverse-biased to create a wide depletion region and achieve a high QE [3]. At the depletion region of a reverse-biased p-n junction, the emission of electrons and holes to restore system equilibrium is dominated by the generation process instead of the recombination process. Moreover, there is a strong electric field that enables the collection of most generated electrons before they are recombined. In a forward-biased p-n junction, recombination takes over the generation process to restore equilibrium at the junction.

The generation rate (G) of an electron-hole pair is modeled by the Shockley-Read-Hall theory [5], [6] as shown in Equation (3-1):

$$G = \left\{ \frac{\sigma_p \sigma_n v_{th} N_t}{\sigma_n \exp\left(\frac{E_t - E_i}{kT}\right) + \sigma_p \exp\left(\frac{E_i - E_t}{kT}\right)} \right\} n_i \tag{3-1}$$

where σ_n corresponds to the electron capture cross section, σ_p corresponds to the hole capture cross section, v_{th} is the thermal velocity, N_t is the concentration of generation centers (silicon defects), E_t corresponds to the energy level of the defect, E_i corresponds to the intrinsic Fermi level, k is the Boltzmann constant, T is the absolute temperature, and n_i is the intrinsic concentration.

What is considered a simple case is when $\sigma_n = \sigma_p = \sigma_o$, from which Equation (3-1) becomes:

$$G = \frac{(v_{th} \sigma_o N_t) \cdot n_i}{2\cosh\left(\frac{E_t - E_i}{kT}\right)} \tag{3-2}$$

From Equation (3-2), it can be inferred that the maximum generation rate value is reached when $E_t = E_i$, whereby G decreases exponentially when E_t moves away from E_i. Another consequence of Equation (3-2) is that the silicon defects whose energy levels are close to mid bandgap contribute the most to the total generation rate.

The generation lifetime (τ_g) is defined as the average time it takes to generate an electron-hole pair. τ_g is given by Equation (3-3) [4]:

$$\tau_g = \frac{2\cosh\left(\frac{E_t - E_i}{kT}\right)}{v_{th} \sigma_o N_t}. \tag{3-3}$$

The depletion dark current (I_{depl}) is defined by Equation (3-4) [4]:

$$I_{depl} = \int_0^W qG\, dx \approx qGW = \frac{q n_i W}{\tau_g} \tag{3-4}$$

where W corresponds to the depletion width, and q is the electronic charge. As Equation (3-4) states, I_{depl} is proportional to the generation rate, which becomes proportional to the intrinsic concentration. As will be shown in Section 3.3, n_i highly depends on temperature, resulting in a temperature dependence of I_{depl}.

3.1.2 Diffusion Dark Current

The diffusion dark current is based on the diffusion (movement) of not only electrons from the p-type neutral region but also holes from the n-type neutral region to the depletion region. At the edges of the depletion region under reverse bias, the minority carrier density is lower than that of equilibrium and reaches the equilibrium by the diffusion of charge coming from the neutral p-type and n-type regions. The continuity equation in the neutral region is represented by Equation (3-5) [4]:

$$\frac{d^2 n_p}{dx^2} - \frac{n_p - n_{p0}}{D_n \tau_n} = 0 \tag{3-5}$$

where n_p is the electron concentration in the p-type region, n_{p0} corresponds to the minority carriers in the p-type region at thermal equilibrium, D_n is the diffusion coefficient of electrons, and τ_n is the minority carrier lifetime. Equation (3-5) can be solved by applying the boundary conditions $n_p(x = \infty) = n_{p0}$ and $n(0) = 0$. Then the diffusion dark current is represented by Equation (3-6) [7] [7]:

$$I_{diff} = \frac{q D_n n_{p0}}{L_n} = q\sqrt{\frac{D_n}{\tau_n}} \cdot \frac{n_i^2}{N_A} \tag{3-6}$$

where L_n corresponds to the diffusion length (representing the average distance at which electrons diffuse before recombining), and N_A is the acceptor concentration. In this case, I_{diff} depends on the square of the intrinsic concentration. Thus, I_{diff} is also temperature-dependent. n_i mainly determines the temperature dependency of I_{depl} and I_{diff}, and as will be shown in Section 3.3, I_{depl} dominates in a certain temperature range while I_{diff} dominates in a different range.

3.1.3 Surface Dark Current

The surface dark current is generated from thermal excitation, as is depletion dark current [4]. However, the generation of dark current at the surface can be higher than at the depletion region because of the existence of more surface or interface states compared to bulk states in the silicon. This large number of surface states is due to the abrupt discontinuity of the lattice structure at the Si-SiO2 interface. The density of these surface states is determined by the fabrication process.

The surface dark current is expressed by Equation (3-7):

$$I_{surf} = \frac{qS_0n_i}{2} \tag{3-7}$$

where S_0 is the surface generation velocity of Si [8]. The trap energy and the capture cross section of Si determine S_0. In addition I_{surf} is proportional to n_i, thus, the surface current is temperature-dependent as are I_{depl} and I_{diff}.

3.1.4 Total Dark Current

The total dark current is obtained by adding the effect of the depletion dark current (Eq. (3-4)), the diffusion dark current (Eq. (3-6)), and the surface dark current (Eq. (3-7)). Equation (3-8) shows the total dark current (I_{dark}):

$$I_{dark} = I_{depl} + I_{diff} + I_{surf} = \frac{qn_iW}{\tau_g} + q\sqrt{\frac{D_n}{\tau_n}} \cdot \frac{n_i^2}{N_A} + \frac{qS_0n_i}{2}. \tag{3-8}$$

With the implementation of the pinned photodiode, the surface dark current can be significantly suppressed. The pinned photodiode structure introduces a p+ pinning layer at the surface of the n-type region, as shown in Figure 3-2.

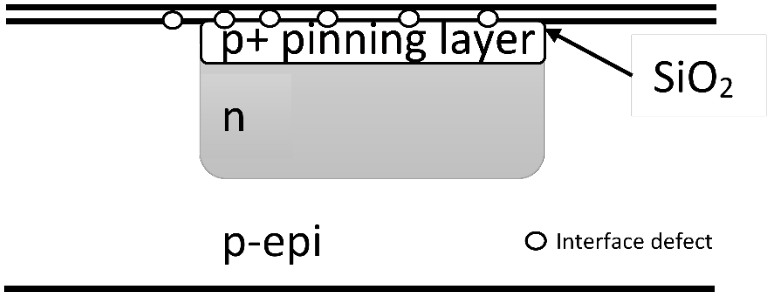

Figure 3-2: Cross section of a simplified pinned photodiode.

The depletion region in the pinning layer is very thin and is separated from the interface due to the heavy doping of the p+ layer. This prevents adding electrons to the charge packet, considerably reducing the surface dark current [9].

3.2 Time Dependence

The amount of (dark) charge generated in the photodiode (mainly) of the pixel is proportional to the integration time, as shown in Equation (3-9) [1]:

$$N_{dark} = \frac{Q_{dark}}{q} = \frac{I_{dark} \cdot t_{INT}}{q} \tag{3-9}$$

where N_{dark} is the amount of (dark) charge (also called the mean dark signal), I_{dark} is the total dark current at a certain temperature, and t_{INT} is the integration time. I_{dark} represents the slope of the mean dark signal corresponding to the integration time, and is expressed as electrons per pixel and per second.

3.3 Temperature Dependence

All components of the dark current defined in Sections 3.1.1, 3.1.2, and 3.1.3 depend on the intrinsic carrier concentration n_i. This concentration n_i highly depends on temperature, as shown in Equation (3-10):

$$n_i = c_n T^{3/2} \exp\left(-\frac{E_g}{2kT}\right) \tag{3-10}$$

where c_n is a constant which depends on Planck's constant and the effective mass of electrons and holes, and E_g corresponds to the energy bandgap of silicon.

At the same time, the energy bandgap of silicon is also temperature-dependent. Equation (3-11) shows the empirical temperature dependence of the bandgap of silicon in eV [10], [11]:

$$E_g(T) = 1.17 - \frac{4.73 \cdot 10^{-4} T^2}{T + 636}. \tag{3-11}$$

In this thesis, the effect of the surface dark current of the pinned photodiode is neglected, replacing Eq. (3-10) with Eq. (3-8). The temperature dependence of the dark current can therefore be expressed by Equation (3-12):

$$I_{dark} = A_{depl} \cdot T^{\frac{3}{2}} \cdot \exp\left(-\frac{E_g}{2kT}\right) + B_{diff} \cdot T^3 \cdot \exp\left(-\frac{E_g}{kT}\right) \tag{3-12}$$

where A_{depl} is a coefficient dependent on the depletion dark current parameters, and B_{diff} is a coefficient dependent on the diffusion dark current parameters. The bandgap of silicon (Equation (3-11)) is not replaced in Equation (3-12), but it is considered in the simulation depicted in Figure 3-2, which shows the dark current behavior with respect to temperature.

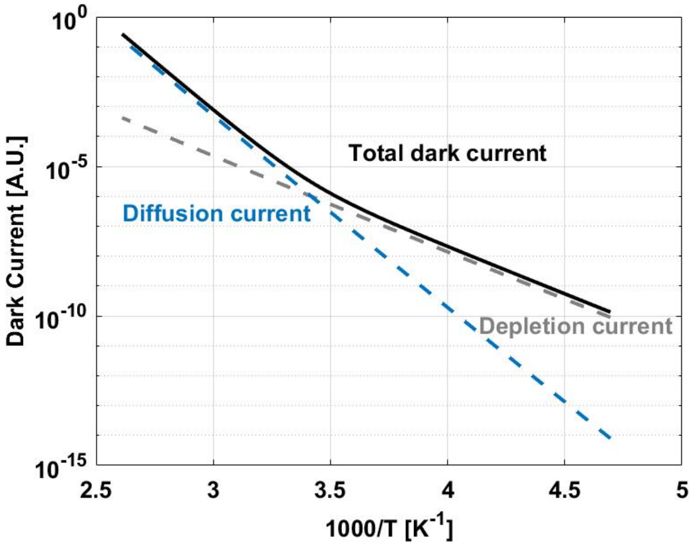

Figure 3-3: Temperature dependence of dark current. Simulation of Equation (3-12).

The simulation of Equation (3-12) (illustrated in Figure 3-2) shows that the dark current follows two different curves depending on the temperature range. It is known that at low temperatures the depletion dark current dominates over the diffusion dark current, while at high temperatures the diffusion dark current becomes the dominant one. Both curves have a characteristic slope depending on the activation energy of the dark current in a certain temperature range. The activation energy can be calculated by using the Meyer-Neldel rule [12], which relates the activation energies and the exponential prefactors for processes that follow an equation in the form of: $X = X_0 \exp(-\Delta E/kT)$. The dark current of Equation (3-12) clearly follows an equation derived from the Meyer-Neldel rule. From Figure 3-2, the activation energy of the depletion dark current can be calculated, obtaining a value of ~ 0.5 eV, which corresponds to (almost) half of the energy bandgap of silicon [7], [13]. The activation energy of the diffusion dark current is in the order of ~ 1.1 eV, corresponding to (almost) the energy bandgap of silicon [7], [13]. The Meyer-Neldel rule can be used to see which kind of dark current mechanism is dominant in a certain temperature range.

3.4 Conclusion

In this chapter the dark current has been defined and its main sources of generation have been presented. The dark current has three main sources: depletion, diffusion, and surface. In the case of a pinned photodiode the surface dark current is reduced and neglected to calculate the temperature behavior of the total dark current. A simulation of the total dark current has shown two different mechanisms depending on the temperature range. By using the Meyer-Neldel rule, it has been found that the depletion dark current dominates at low temperatures where the activation energy is half that of the silicon bandgap, while the diffusion dark current dominates at high temperatures where the activation energy is about that of the silicon bandgap.

References

[1] J. Nakamura, *Image Sensors and Signal Processing for Digital Still Cameras*. Taylor & Francis Inc, 2005, pp. 67-72.

[2] M. M. Blouke, "Diffusion dark current in front-illuminated CCDs and CMOS image sensors," in *Sensors, Cameras, and Systems for Industrial and Scientific Applications XIII*, 2021, pp. 1-15.

[3] X. Wang, "Noise in sub-micron CMOS image sensors," Ph.D. Dissertation, Delft University of Technology, pp. 45-55, 2008.

[4] S. M. Sze, *Semiconductor devices: Physics and technology*. John Wiley & Sons, 1985, pp. 48-55.

[5] W. Shockley and W. T. Read, "Statistics of the Recombinations of Holes and Electrons," *Physical Review,* vol. 87, pp. 835-842, 1952.

[6] R. N. Hall, "Electron-Hole Recombination in Germanium," *Physical Review,* vol. 87, pp. 387-387, 1952.

[7] R. Widenhorn, M. M. Blouke, A. Weber, A. Rest, and E. Bodegom, "Temperature dependence of dark current in a CCD," in *Sensors and Camera Systems for Scientific, Industrial, and Digital Photography Applications III*, 2002, pp. 193-201.

[8] R. Pierret, *Advanced Semiconductors Fundamentals*. Addison-Wesley, 1987, pp. 134-165.

[9] N. Teranishi, A. Kohono, Y. Ishihara, E. Oda, and K. Arai, "No image lag photodiode structure in the interline CCD image sensor," in *1982 International Electron Devices Meeting*, 1982: IRE, pp. 324-327.

[10] Y. P. Varshni, "Temperature dependence of the energy gap in semiconductors," *Physica,* vol. 34, pp. 149-154, 1967.

[11] W. Bludau, A. Onton, and W. Heinke, "Temperature dependence of the band gap of silicon," *Journal of Applied Physics,* vol. 45, pp. 1846-1848, 1974.

[12] R. Widenhorn, L. Mündermann, A. Rest, and E. Bodegom, "Meyer–Neldel rule for dark current in charge-coupled devices," *Journal of Applied Physics,* vol. 89, pp. 8179-8182, 2001.

[13] H. I. Kwon, I. M. Kang, B.-G. Park, J. D. Lee, and S. S. Park, "The Analysis of Dark Signals in the CMOS APS Imagers From the Characterization of Test Structures," *IEEE Transactions on Electron Devices,* vol. 51, pp. 178-184, 2 2004.

4 INTEGRATION OF BJT-BASED TEMPERATURE SENSORS INTO A CMOS IMAGE SENSOR

This chapter of the thesis is based on the publication:

A. Abarca, S. Xie, J. Markenhof, and A. Theuwissen, “Integration of 555 temperature sensors into a 64 × 194 CMOS image sensor,” *Sensors and Actuators A: Physical*, vol. 282, pp. 243-250, 2018.

This chapter presents a novel approach for measuring relative temperature variations across the active area of a CMOS image sensor. 555 out of 12,288 image pixels have been replaced with temperature sensor pixels (Tixels) in the same pixel array layer. Sensors, pixels and Tixels all utilize the same readout structure to obtain data. The measured temperature variations in the pixel array can then be used in a compensation algorithm for dark signal non-uniformity. Measurements of dark current and temperature have been performed in a temperature range between -40 °C and 90 °C. The results demonstrate that pixels and Tixels can effectively share the same readout system based on source followers and column amplifiers. The average dark current of the image sensor increases with temperature in the temperature range of -40 °C to 60 °C, and at the same time, the Tixels exhibit a highly linear response, achieving an inaccuracy (3σ) of ±0.3 °C after systematic non-linearity removal and a fixed 5th order polynomial.

4.1 Introduction

One of the major contributors of fixed pattern noise (FPN) in image sensors is dark current, or leakage current. The dark current FPN greatly depends on process variations and temperature variations. It has been reported that dark current doubles its value every 5-10 °C for temperatures above 10 °C [1], [2]. Dark current can be compensated by means of a dark reference frame. To take a dark reference frame, a mechanical shutter is needed. However, in the case of mobile phones a mechanical shutter is not available. Efforts to reduce the effect of dark current have also been made by modifying the photodetector at the physical level, by, for instance, adding a p-well layer to surround the pixel [3].

This design proposes the integration of temperature sensors in the same layer as the image pixels and using the same readout system to obtain the data from the pixel-Tixel sensors. In this way, relative temperature variations can be measured as well as the temperature distribution in the pixel array. This information can then be used to compensate for dark current after the calibration of the Tixels and pixels, i.e. in terms of dark current at different temperatures. For instance, it is possible to recreate a “non-uniform” dark reference frame by using the temperature measurements of the Tixels.

A description of the pixel and Tixel architectures is presented in Section 4.2. An overview of the readout system is given in Section 4.3. Then, in Section 4.4, the measurement setup is described. The measurement results of the CIS, including the Tixels, are then presented in Section 4.5. Finally, this chapter is concluded in Section 4.6.

4.2 Description of the Sensor

The sensor array is composed of image pixels and temperature sensor pixels. In the following sections, both sensors will be presented.

4.2.1 Pixel Architecture

The image pixels are based on a typical CMOS 4T (4-transistor) architecture, as shown in Figure 4-1 (a). This architecture is composed of a pinned photodiode (PPD), a floating diffusion (FD) and four transistors: the reset transistor (RST), the transfer gate (TG), the source follower (SF), and a row select (RS) transistor. In this architecture, the incoming light is converted by the pinned photodiode into electrical charge while the TG is closed. When the TG is open, all this charge is transferred to the floating diffusion where the charge is converted into a voltage signal. Then, this signal is readout via the source follower before being amplified by the column amplifier block. The 4T architecture allows a fully noiseless charge transfer thanks to the p-n-p structure of the pinned photodiode. When the FD is exposed (after reset) to a voltage higher than (or equal to) the pinning voltage and the TG is on, the diode becomes fully depleted allowing the full noiseless charge transfer [4], [5]. Other features of the 4T architecture are: low noise, low dark current and high quantum efficiency [6].

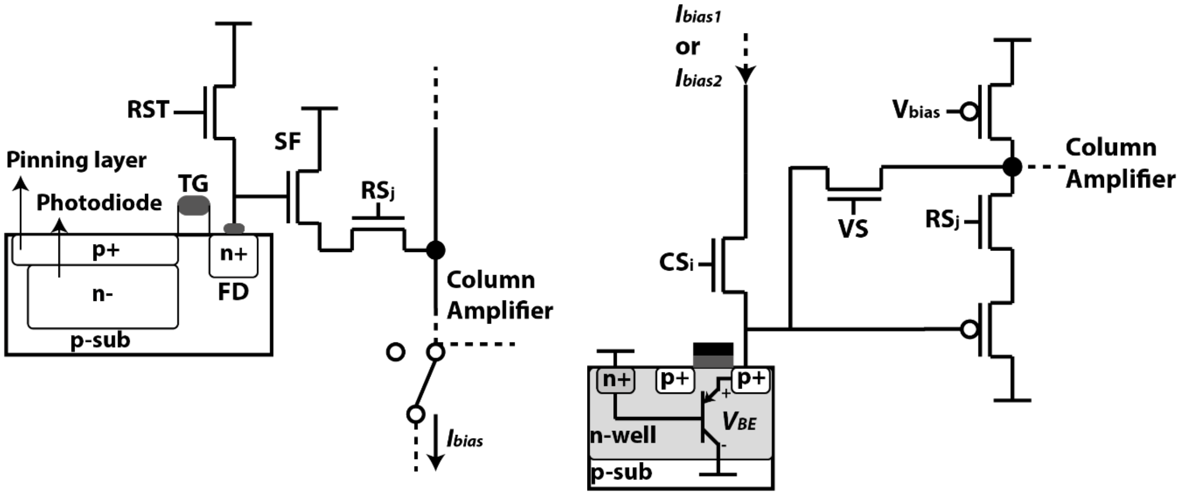

(a) (b)

Figure 4-1: (a) 4T image pixel architecture. (b) Tixel architecture based on BJT.

In the design used to test the Tixel concept, the size of an image pixel is 11×11 μm^2. The test array consists of 64 rows and 192 columns, which means that it contains 11,733 image pixels in total (excluding the 555 Tixels).

4.2.1.1 Parameter Simulations of the Pixel

The 4T pixel is biased by a current generated from a Gm-cell. The schematic of the Gm-cell is shown in Figure 4-2.

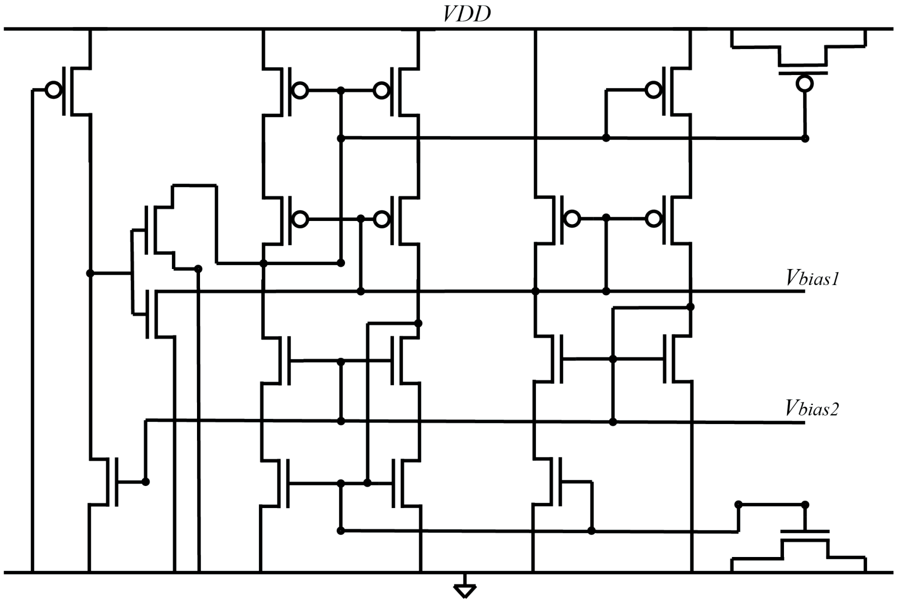

Figure 4-2: Gm-cell used to bias the pixels.

The Gm-cell is used to tune the conversion gain of a pixel and, thanks to its low noise, provides a very stable bias current over time (exposure time) [7]. The bias current of the pixel (I_{pix}) over temperature is shown in Figure 4-3.

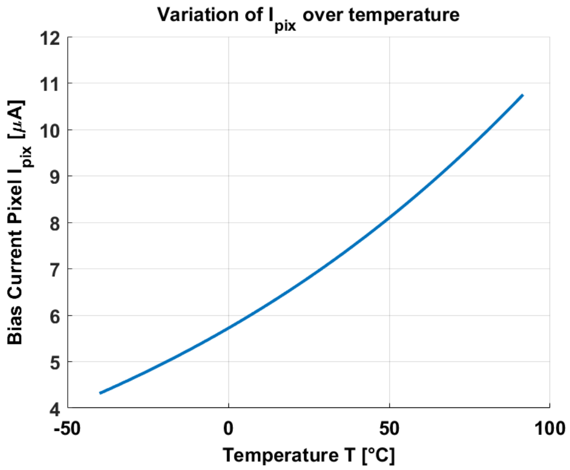

Figure 4-3: Bias current of the pixel over temperature.

Figure 4-3 shows that I_{pix} varies from 4 µA at -40 °C to 12 µA at 100 °C, with a value of 6.7 µA at room temperature.

The conversion gain was simulated over temperature, as shown in Figure 4-4.

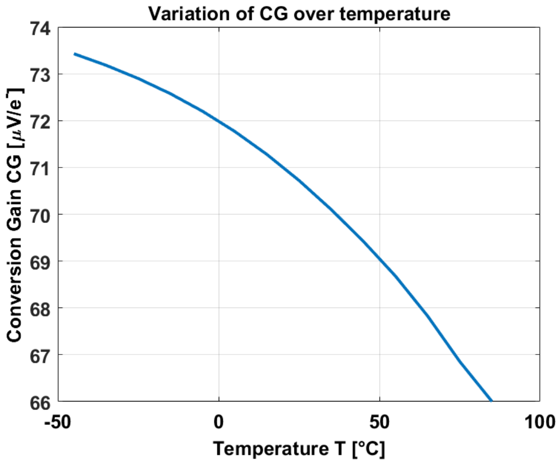

Figure 4-4: Conversion gain vs. temperature.

The simulated conversion gain decreases over temperature at a rate of approximately 0.0538 µV/e$^-$/°C. This value is in line with [8]. The conversion gain is used to express the pixel's parameters in terms of e^-, and it will be used to calculate the dark current of the pixel array.

4.2.2 Tixel Architecture

A Tixel consists of a parasitic Bipolar Junction Transistor (BJT), which is the core of the Tixel, as well as a column selector and a pMOS source follower, as shown in Figure 4-1 (b). In this case, a pMOS source follower is used instead of an nMOS source follower, as in the case of the pixels. Compared to the nMOS source follower used in the pixels, simulations show that the pMOS source follower exhibits better linearity over the output signal range of the Tixels. This is because of the base-emitter voltage of the BJT (V_{BE}) is close to 0.7 V and V_{BE} may drop to lower values close to the threshold of an nMOS transistor. This means that an nMOS SF would not work for the Tixel. Compared to MOS-based alternatives, a BJT-based temperature sensor exhibits better accuracy and lower process variations [9], [10].

The Tixel is selected (and turned on) by a column decoder that controls the CS_i transistor. When this transistor is on, the BJT can be biased by two different currents (I_{bias1} and I_{bias2}). The base-emitter signal is then buffered by the pMOS source follower before being amplified by the column amplifier. The schematic of the Tixel and the layout of the Tixel surrounding by pixels are shown in Figure 4-5.

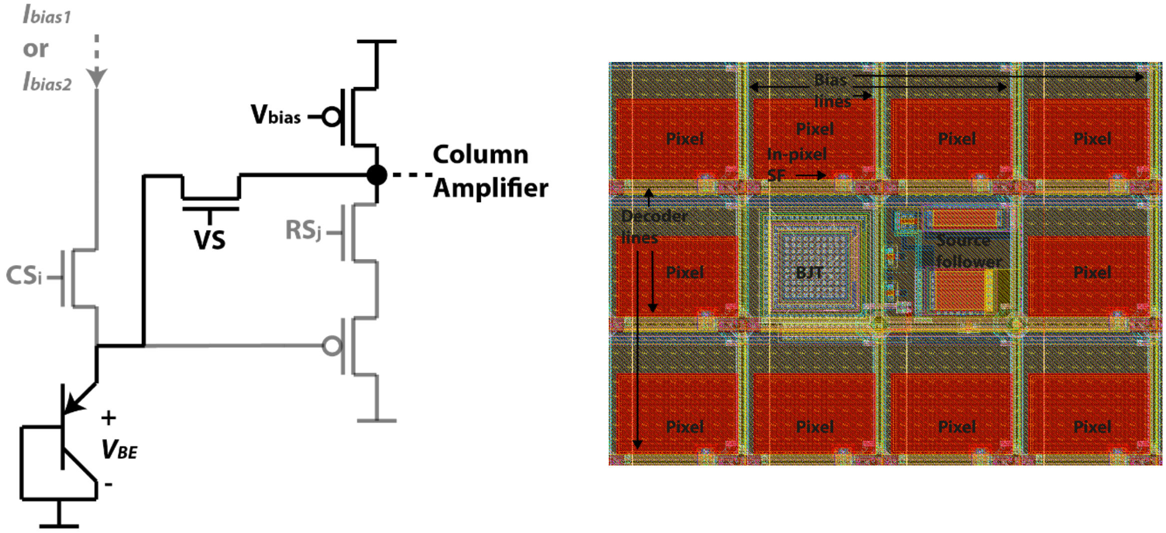

(a) (b)

Figure 4-5: (a) Schematic of the Tixel. (b) Layout of the Tixel and pixels.

The size of the Tixel is 11×22 μm^2, thus twice the size of a pixel. This is because of the extra transistors used in the Tixels to implement direct and indirect mode. 555 Tixels have been uniformly integrated in the same layer as the pixels, with approximately three Tixels per row and eight Tixels per column, as shown in Figure 4-6.

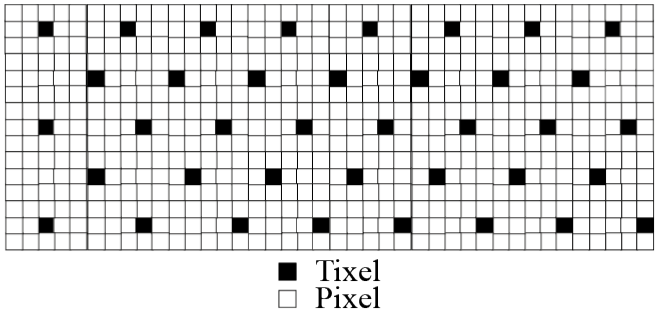

Figure 4-6. Diagram of the Tixel integration into a CMOS image sensor pixel array.

The test chips have been fabricated by a standard 0.18 μm CMOS Image Sensor (CIS) TowerJazz Technology.

BJT-based temperature sensors can be implemented either by a npn BJT or a pnp BJT. In this thesis, a pnp substrate parasitic BJT is used because the npn option is not available in this technology. A pnp substrate BJT in a diode connection is shown in Figure 4-7 (a).

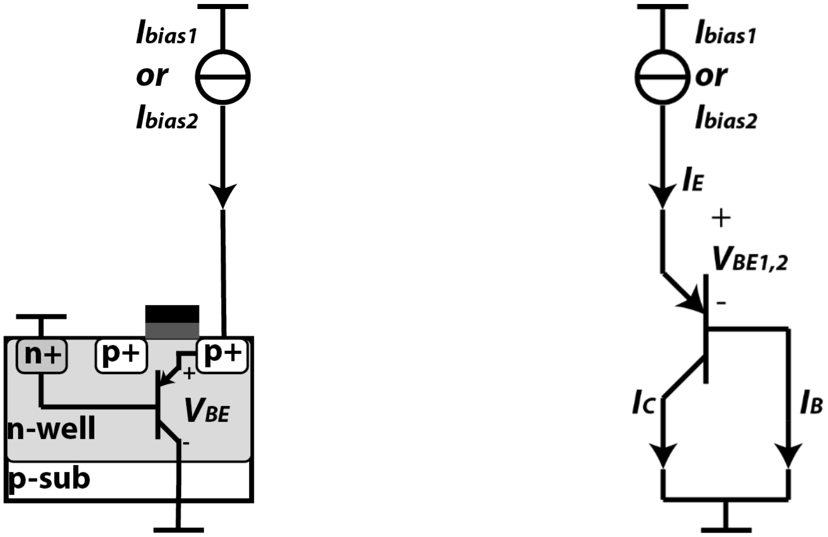

(a) (b)

Figure 4-7: (a) A pnp substrate parasitic BJT. (b) A pnp BJT in a diode connection. I_E is the emitter current, I_C is the collector current, and I_B is the base current.

When the BJT is biased by two different currents (Figure 4-7 (b)), the $I_E - V_{BE}$ characteristic of the pnp BJT in the exponential region can be expressed by the following equations (where I_E corresponds to $I_{bias1,2}$):

$$I_{bias1} = I_S \exp\left(\frac{qV_{BE1}}{kT}\right) \rightarrow V_{BE1} = \frac{kT}{q} \ln\left(\frac{I_{bias1}}{I_S}\right)$$

$$I_{bias2} = I_S \exp\left(\frac{qV_{BE2}}{kT}\right) \rightarrow V_{BE2} = \frac{kT}{q} \ln\left(\frac{I_{bias2}}{I_S}\right) \tag{4-1}$$

where I_S is the saturation current, q corresponds to the electric charge, k corresponds to the Boltzmann constant, T is the absolute temperature, and V_{BE1} and V_{BE2} correspond to the base-emitter voltages of the BJT when it is biased by I_{BE1} and I_{BE2}, respectively. Defining $r = I_{bias2}/I_{bias1}$ as the ratio between the two currents, temperature is determined via the differential base-emitter voltage (ΔV_{BE}), which is proportional to the absolute temperature (PTAT) [11], as Equation (4-2) shows:

$$V_{BE2} - V_{BE1} = \Delta V_{BE} = \frac{kT}{q} \ln(r) \rightarrow T = \frac{\Delta V_{BE}\, q}{k \ln(r)} \tag{4-2}$$

The current ratio r needs to be constant to generate a ΔV_{BE} that is accurately PTAT, as shown in Equation (4-2). However, the ground connection of the base-collector voltage results in a collector current that is smaller than the bias current applied to the emitter [12], as shown in Equation (4-3):

$$I_C = I_E - I_B = \alpha_F I_E = \frac{\beta_F}{1 + \beta_F} I_E \tag{4-3}$$

where α_F corresponds to the common-base current gain, and β_F is the common-emitter current gain. In order to obtain an accurate PTAT voltage, α_F (and consequently β_F) has to be current-independent, thus, an emitter-current ratio results in the same collector-current ratio:

$$\frac{r \cdot I_E}{I_E} = \frac{r \cdot I_C}{I_C}. \tag{4-4}$$

Otherwise, it will result in an error in the PTAT voltage as shown in Equation (4-5):

$$\Delta V_{BE} = \frac{kT}{q}\ln\left(\frac{I_{C2}}{I_{C1}}\right) = \frac{kT}{q}\ln\left(\frac{I_{E2}\beta_{F2}(\beta_{F1}+1)}{I_{E1}\beta_{F1}(\beta_{F2}+1)}\right) \tag{4-5}$$

where β_{F1} corresponds to the current gain at I_{E1}, and β_{F2} is the current gain at $I_{E2} = rI_{E1}$. From Equation (4-5), it is clear that the current gain needs to be constant for the chosen bias currents. Simulations will be performed to choose the right bias current in the region where β_F is current independent as well as the current ratio r.

4.2.2.1 Design and Simulations of the Tixel

The 0.18 µm TowerJazz CIS technology provides three standard libraries of BJTs with an emitter area of: 10×10 µm^2, 5×5 µm^2 and 2×2 µm^2. The BJT with an emitter area of 10×10 µm^2 is discarded because the Tixel (BJT + in-Tixel transistors) is intended to be fitted in one (or two) pixel area of 11×11 µm^2. The other two emitter area options are compared in terms of the current gain (β_F), the temperature coefficient (TC), and the non-linearity error.

The I-V characteristic of both BJTs (at room temperature) was simulated over a wide emitter current range in order to find the limits of the exponential region of the BJTs. This is shown in Figure 4-8.

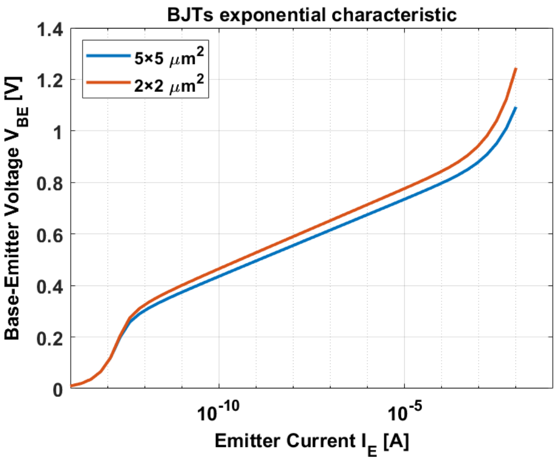

Figure 4-8: I-V characteristic of the BJTs with different emitter area at room temperature.

The exponential characteristic of both BJTs is achieved in the emitter current range of 1 pA to ~0.1 mA. In this range, the base-emitter voltage has values between 0.4 V and 0.8 V. Biasing the BJTs with emitter currents in the range of µA seems suitable as these values are almost in the middle of the exponential region of the BJTs. Also, it is worth mentioning that higher voltage values are achieved by using the BJT with an area of 2×2 μm^2 compared to the BJT with an area of 5×5 μm^2 when using the same emitter current. This is because of the saturation current (I_S). I_S is proportional to the emitter area of the BJT, as shown in Equation (4-6):

$$I_S = \frac{qAn_i^2\overline{D_p}}{W_B N_d} \tag{4-6}$$

where A is the emitter area, n_i is the intrinsic carrier concentration, $\overline{D_p}$ is the average diffusion constant of holes in the base, W_B is the base width, and N_d is the donor concentration. If Equation (4-6) is replaced in (4-1), it is clear that V_{BE} of a BJT with an area of 2×2 μm^2 is higher than V_{BE} of a BJT with an area 2×2 μm^2.

The current gain was simulated for various values of the emitter current in the temperature range of -40 °C to 100 °C (in 20 °C steps), as shown in Figure 4-9.

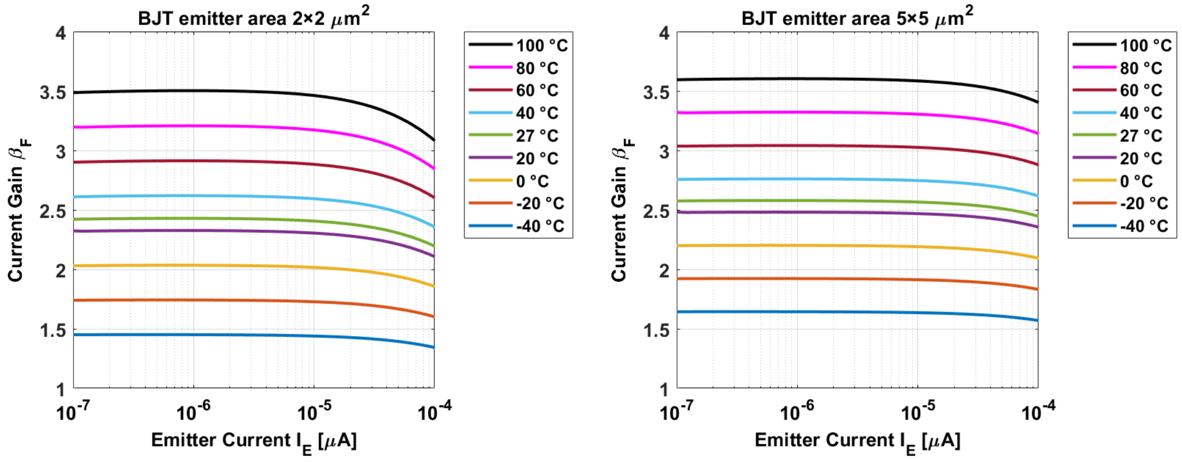

(a) (b)

Figure 4-9. (a) Current gain vs. emitter current in a BJT with an emitter area of 2×2 μm^2 as function of temperature. (b) Current gain vs. emitter current in a BJT with an emitter area of 5×5 μm^2 as a function of temperature.

The flat region of β_F extends up to ~10 μA (for all temperatures) in a BJT with an emitter area of 5×5 μm^2. In the case of a BJT with an emitter area of 2×2 μm^2, β_F exhibits a flat region between 0.1 μA and 6 μA. Therefore, the BJT with an emitter area of 5×5 μm^2 provides a wider bias current range to bias the BJT-based temperature sensor for this design. The Gm-based bias current (Figure 4-3) used for the pixels could be an option to bias the BJT. However, the Gm-based bias current already reaches a value of ~10 µA at 80 °C which is the limit of the flat region of β_F. This makes the Gm-based bias current not a suitable for the temperature sensor. An externally generated bias current of 1µA is chosen as a unit current to bias the Tixel because it is in the middle of the β_F flat region, which gives enough room in order to choose different current ratios, for example, even up to 10:1 (in the case of the BJT with an emitter area of 5×5 µm^2). The current ratio is generated by an on-chip current mirror (Figure 4-15).

From Equation (4-5), the following factor β_r is defined:

$$\beta_r = \frac{\beta_{F2} \cdot (1+\beta_{F1})}{\beta_{F1} \cdot (1+\beta_{F2})}. \tag{4-7}$$

In order to realize how β_r affects ΔV_{BE}, the variation of factor β_r over temperature for various current ratios was simulated and is shown in Figure 4-10.

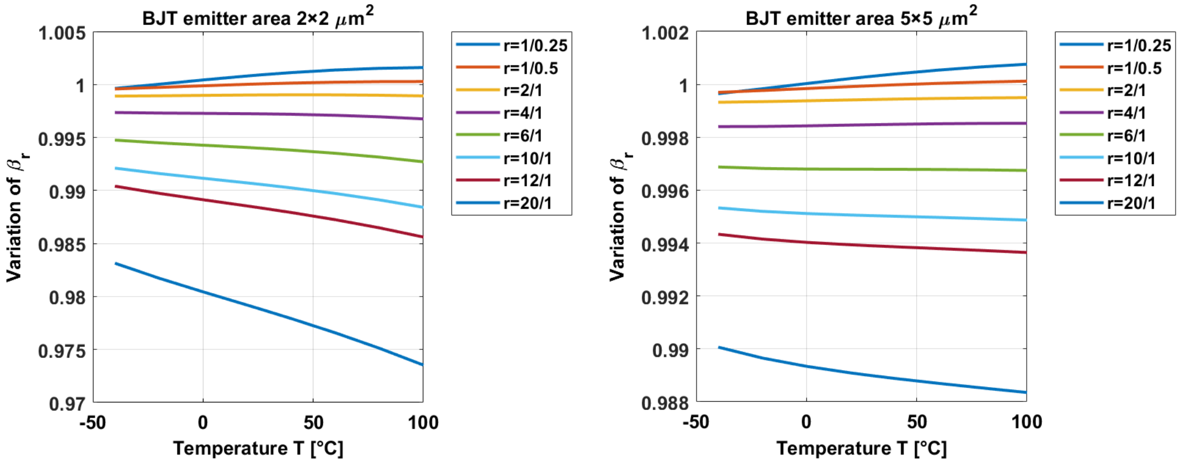

(a) (b)

Figure 4-10: (a) Variation of β_r vs. temperature in a BJT with an emitter area of 2×2 µm^2 as function of the current ratio. (b) Variation of β_r vs. temperature in a BJT with an emitter area of 5×5 µm^2 as a function of the current ratio.

The variation of β_r over temperature is larger in the case of the 2×2 µm^2 BJT than the BJT with an area of 5×5 µm^2. The variation of β_r increases with the ratio r, as shown in Figure 4-10 (a) and (b). In the case of the BJT with an area of 5×5 µm^2, the current gain variation remains almost constant for the current ratios: $r = 2/1$, $r = 4/1$, and $r = 6/1$. Of these three current ratios, when $r = 4/1$, the current gain variation exhibits the best (flat) performance over temperature. Thus, a current ratio $r = 4/1$ is the chosen to bias the BJT.

The temperature coefficient and the non-linearity error of both types of BJTs are compared in Figure 4-11. The BJTs were biased by using a current ratio $r = 4/1$ with a unit current of 1 µA. The non-linearity error was calculated by using a 1st order curve fitting over the range of 20 °C to 90 °C.

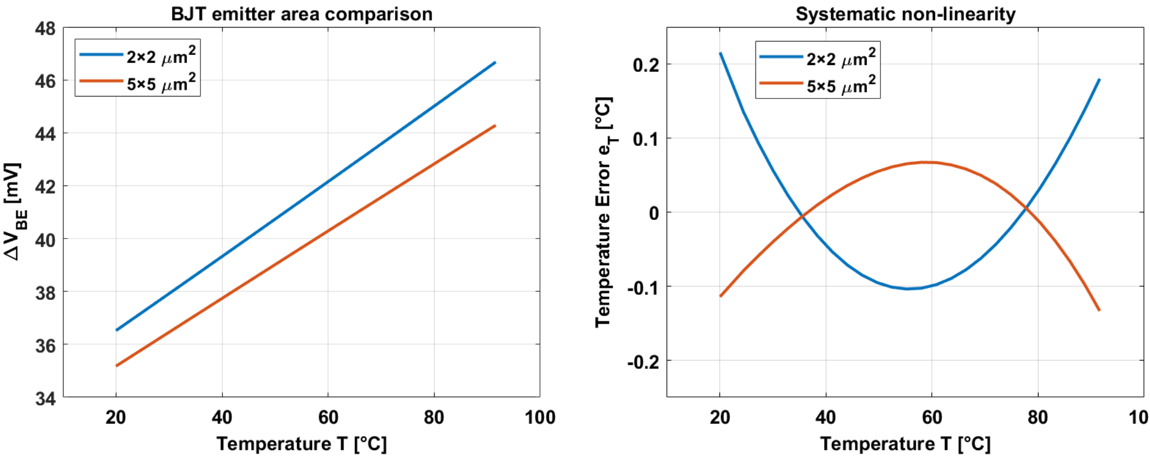

(a) (b)

Figure 4-11. (a) Differential base-emitter voltage vs. temperature for two BJT emitter areas. (b) Non-linearity error of both types of BJTs after a 1st order curve fitting.

The BJT with an emitter area of 2×2 µm^2 has a temperature coefficient of 0.14 mV/°C. This TC exhibits a higher sensitivity than the TC of the BJT with an emitter area of 5×5 µm^2, which is 0.13 mV/°C. This is because of the influence of the saturation current, as it was discussed previously in this chapter. However, after a 1st order fit, the non-linearity of the BJT 2×2 µm^2, which is ±0.25 °C, is higher than the non-linearity error of ±0.1 °C in the case of the BJT 5×5 µm^2.

Considering the current gain behavior and the non-linearity error, the BJT with an emitter area of 5×5 µm^2 is a better option than the 2×2 µm^2 emitter area. Therefore, a BJT with an emitter area of 5×5 µm^2 is the chosen as the core of the Tixel.

By using a BJT with an emitter area of 5×5 µm^2, a Monte Carlo simulation was performed in order to calculate the inaccuracy of the Tixel (BJT + in-Tixel transistors). In this simulation an ideal unit current of 1 µA and a current ratio 4:1 was used. Figure 4-12 shows the temperature coefficient (TC) and the systematic non-linearity over a temperature range of 20 °C and 90 °C. The process spread is first compensated by an individual linear fit, while the remaining nonlinearity is corrected by a fixed 5th order polynomial.

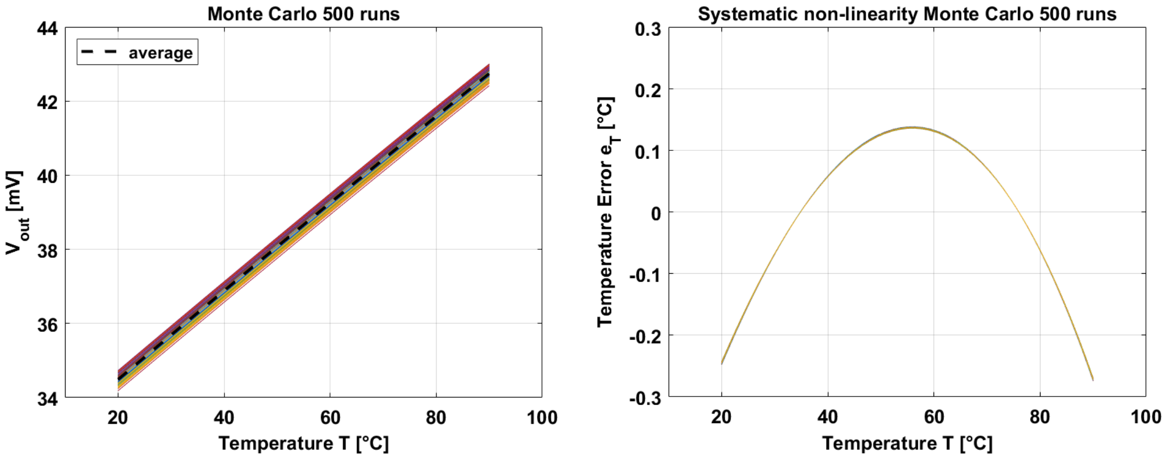

(a) (b)

Figure 4-12: (a) Temperature coefficient of the Tixel. (b) Systematic non-linearity error of the Tixel after a 1st order curve fitting.

The output voltage of the Tixel covers a range from 34 mV to 43 mV with an average temperature coefficient of 0.12 mV/°C, as shown in Figure 4-12 (a). The systematic non-linearity error of the Tixel corresponds to ±0.25 °C after a 1st order curve fitting and is shown in Figure 4-12(b). The inaccuracy of the Tixel is obtained by removing the systematic non-linearity error by applying a fixed 5th order polynomial.

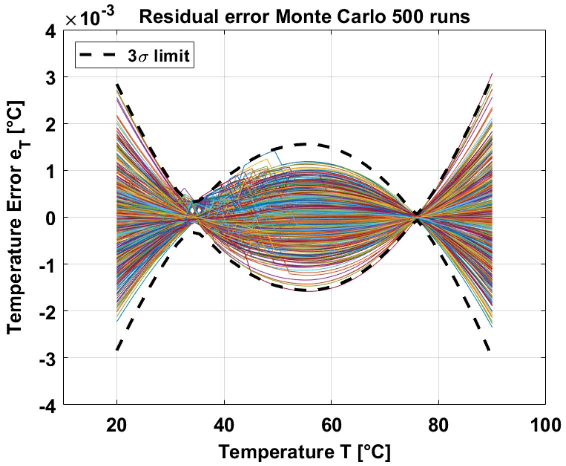

Figure 4-13: Inaccuracy of the Tixel after systematic non-linearity removal and a 5th order polynomial.

The inaccuracy of the Tixel corresponds to ±0.003 °C (3σ).

4.3 Readout System

The same control signals and readout structure are used by pixels and Tixels. The readout system consists of row and column decoders. These decoders generate the signals which select each element of the image array. They also generate signals that select the source followers and the column amplifiers.

A biasing block provides the bias currents to the Tixels. It generates a ratio of 4:1. The output signals of the pixels or Tixels are amplified by the column amplifier block (Figure 4-14). This block is composed of a Programmable Gain Amplifier (PGA), which performs the Correlated Doubling Sampling (CDS), a sample and hold circuit (S/H) and a buffer (these blocks are part of the standard libraries of the CMOS image sensor group at TU Delft and have been modified accordingly). The PGA provides five different gains (G): 1, 2, 4, 8, and 16. The CDS circuit is used to cancel the kTC noise of the image sensor [13], [14]. Then, the amplified signal (G$\cdot$ ΔV_{BE}, where G is the gain) is buffered by an output buffer circuit before being digitized by an off-chip 16-bit ADC [15]. A block diagram of the readout system is presented in Figure 4-14.

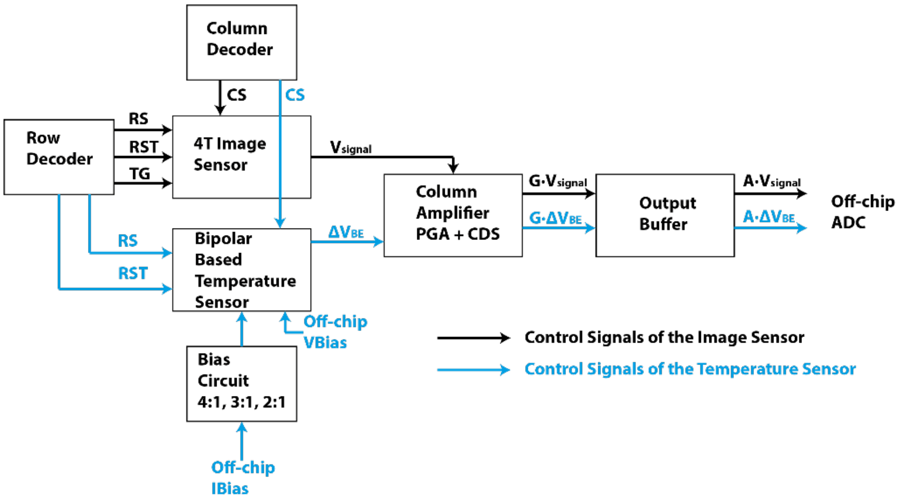

Figure 4-14: Block diagram of the readout system.

4.3.1 Current Mirror

The biasing currents are generated by an on-chip current mirror block which is biased by an external current (I_{ext}) of 1µA. The current mirror is shown in Figure 4-15.

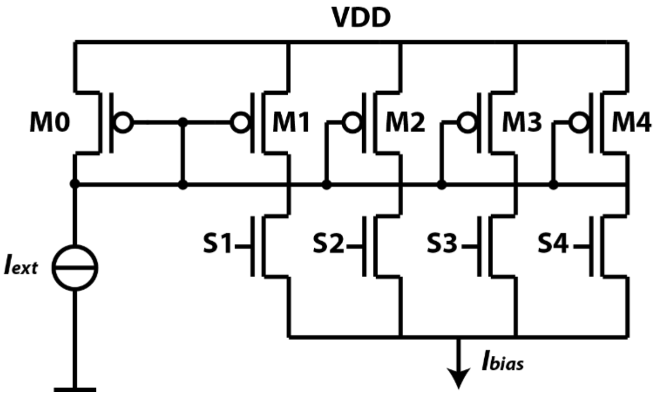

Figure 4-15: On-chip current mirror.

The current mirror provides the current ratio of 4:1 and there is one per row. This means that there are sixty four current mirrors in the design. The sixty four current mirror were implemented in order to achieve a better robustness. Each one is selected by using the row and column decoders (the same as for the pixels). The spread and the inaccuracy caused by the process variation of the current mirror is shown in Figure 4-16.

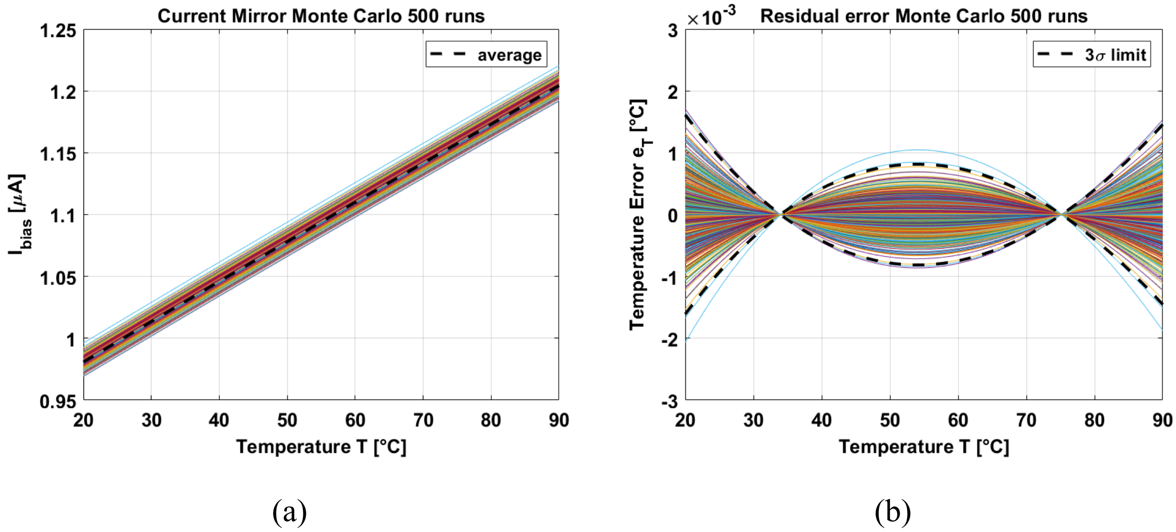

Figure 4-16: (a) Spread of the Tixel when biased by the current mirror. (b) Corresponding inaccuracy of the current mirror after systematic non-linearity removal and a 5th order polynomial.

The spread of the current mirror corresponds to ±1.3 % from the average when the external bias current is 1 µA (when the bias current is 4 µA, the spread is less). Also, the current exhibits a PTAT behavior over temperature, which helps to compensate for the curvature of the base-emitter voltage of the BJT [12]. The spread of the current mirror leads to a simulated temperature sensor inaccuracy of ±0.002 °C (3σ) after systematic error removal and a 5th order polynomial.

4.3.2 Column Amplifier

The schematic of the switch-capacitor correlated double sampling (CDS) column amplifier is presented in this section. The column amplifier is composed of a programmable gain amplifier (PGA), two banks of capacitors that set the gain of the PGA, a sample and hold circuit (S/H) with analog memories, and an output buffer. The schematic of the column amplifier, including the pixel and the off-chip ADC, is shown in Figure 4-17 .

The PGA provides five levels of gain 1×, 2×, 4×, 8×, and 16× by varying the ratio of the input and feedback capacitors C_1 and C_2, respectively. The gain corresponds to $G = C_1/C_2$ and it depends on the combination of the banks of capacitors C_1 and C_2. C_1 is a bank of sixteen capacitors of 100 fF in parallel and C_2 contains four capacitors of 100 fF in parallel. For instance, a gain of 16 is set by selecting all the capacitors in C_1 and only one in C_2. The gain is selected via a decoder. The analog memories of the S/H circuit corresponds to C_S (signal capacitor) and C_R (reference capacitor). The S/H circuit is controlled by signals *SHS* and *SHR* for the sample phase, and by signals *READS* and *READR* for the readout phase (off-chip ADC).

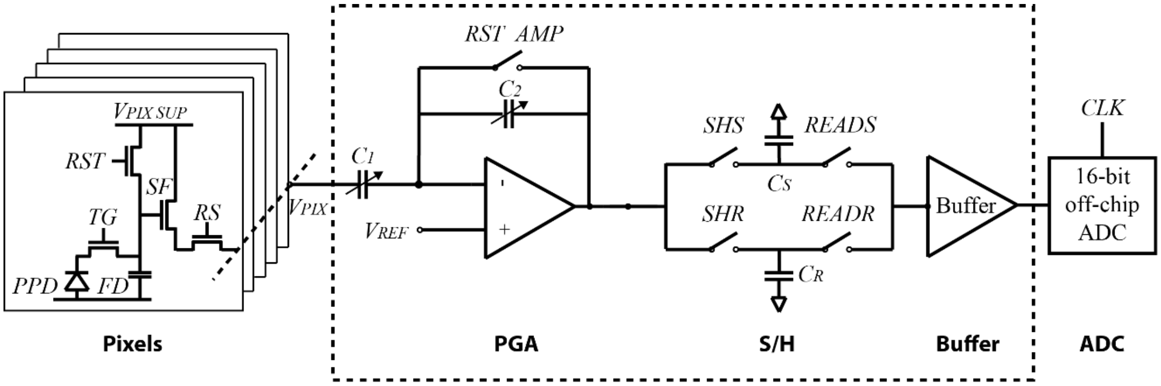

Figure 4-17. Schematic of the column amplifier.

The column amplifier realizes the CDS operation. When the pixel is used for imaging, the floating diffusion (*FD*) node is reset by turning on the reset transistor (*RST*) while the transfer gate (*TG*) transistor of the pinned-photodiode (*PPD*) is turned off. The reset level (V_{RST}) is available and stored in C_1 while V_{REF} and the offset of the amplifier (V_{OS}) are sampled and stored in capacitor C_R (*SHR* is on). After the first phase, the *TG* is turned on and the charge packet is transferred from the *PPD* to the *FD* node. In the *FD* node, the charge packet is converted into voltage and buffered by the source follower (*SF*). The video signal V_{PIX} is available in C_1 together with V_{RST}, obtaining the differential voltage $\Delta V = V_{PIX} - V_{RST}$ which is amplified by the gain $G = C_1/C_2$ and stored with $V_{OS} + V_{REF}$ in capacitor C_S when *SHS* in on. Finally, signals in capacitors C_R and C_S are readout by using control signals *READR* and *READS*, respectively. The output buffer helps to avoid considerable attenuation and fluctuation of the signal. An off-chip ADC digitizes both signals of the S/H circuit.

When the temperature sensors are used, for example the BJT, the output voltage V_{BE1} (biased at 1 μA) is stored in C_1 and the offset plus the reference voltage ($V_{OS} + V_{REF}$) are sampled and stored in the analog memory C_R in the S/H circuit. Then, in the next phase the output signal of the temperature sensor V_{BE2} (biased at 4 μA) is stored in C_1, obtaining the differential base-emitter voltage ($\Delta V_{BE} = V_{BE2} - V_{BE1}$) which is amplified by the gain $G = C_1/C_2$ and stored with ($V_{OS} + V_{REF}$) in C_S. In this way, subtracting the stored values in both analog memories cancels the offset: $V_{out} = (G \cdot \Delta V_{BE} + V_{REF} + V_{OS}) - (V_{REF} + V_{OS}) = G \cdot \Delta V_{BE}$.

In the column amplifier, a differential input and single ended output telescopic cascode OPA structure is used, as shown in Figure 4-18. The telescopic cascode OPA provides a high open-loop gain, low input referred noise, and a proper dynamic range for image sensor's applications, as shown in Table 4-1.

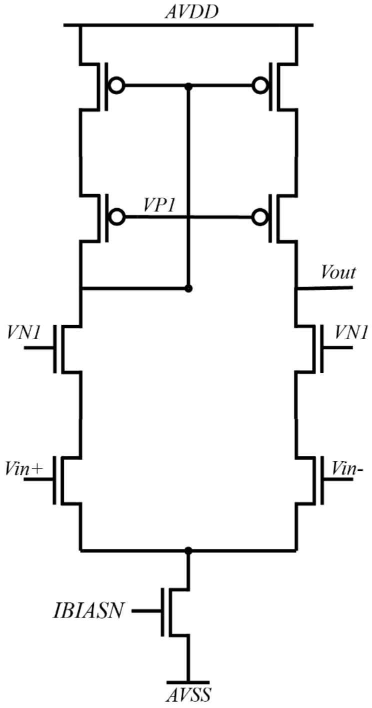

Figure 4-18. Telescopic cascode OPA, core of the PGA.

Table 4-1. Characteristics of the telescopic OTA.

Characteristic	Value
Power [μW]	99
Output Range [V]	1.5
Output Common Mode Voltage [V]	1.1
Open-loop Gain [dB]	85
-3dB Bandwidth [MHz]	2.4 @ gain 16
Gain Bandwidth [MHz]	50
Input Referred Noise [μV]	33 @ gain 16
Settling Time [ns]	150
PSRR	vs. Power Supply 60dB @ 2MHz vs. Ground 28 dB @ 2MHz

4.3.3 Simulation Temperature Sensor

The temperature coefficient, non-linearity and the inaccuracy (3σ) of the temperature sensor (Tixel + readout) was determined by a Monte Carlo simulation (500 runs). The average temperature coefficient of the temperature sensor is 1.22 mV/°C, as shown in Figure 4-19 (a).

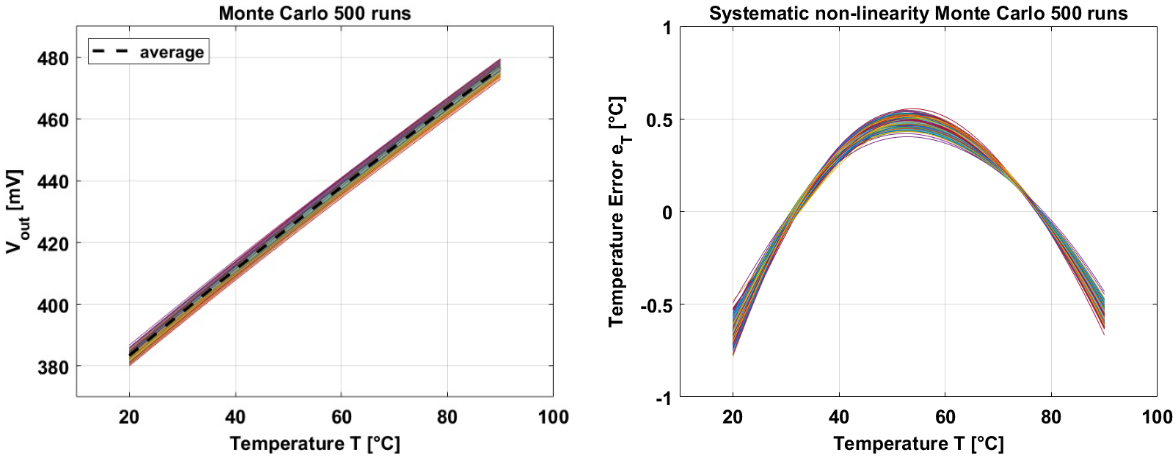

(a) (b)

Figure 4-19: (a) Temperature coefficient. (b) Systematic non-linearity error after a 1st order curve fitting.

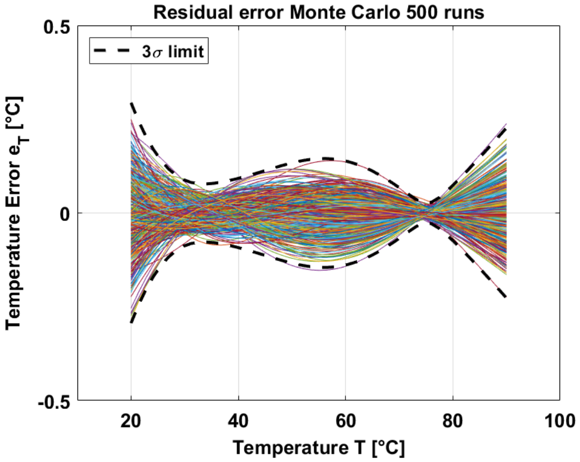

Figure 4-20: Inaccuracy of the temperature sensor after systematic non-linearity removal and a 5th order polynomial.

The systematic non-linearity of Figure 4-19 (b) was calculated after a 1st order curve fitting. The non-linearity is ±0.7 °C. When the systematic non-linearity is removed and a 5th order polynomial is applied, the inaccuracy of the temperature sensor is obtained, as shown in Figure 4-20. The inaccuracy has a value of ±0.25 °C.

4.4 Measurement Setup

The measurement setup consists of a PCB, FPGA, a PC with Quartus and LabView, and a temperature-controlled oven. The test chip is mounted on the PCB that both provides all the power supplied to the chip and contains the 16-bit ADC. The FPGA generates all the control signals for the chip and for the ADC. The FPGA is configured by using Quartus. The data of the chip is collected by utilizing LabView. Two different temperature-controlled ovens have been used depending on the temperature range. For the temperature range between 20 °C and 90 °C a Binder FP53 oven was used. On the other hand, for the temperature range between -40 °C and 90 °C a Vötsch VT7004 oven was used. Two different ovens were used depending on their availability.

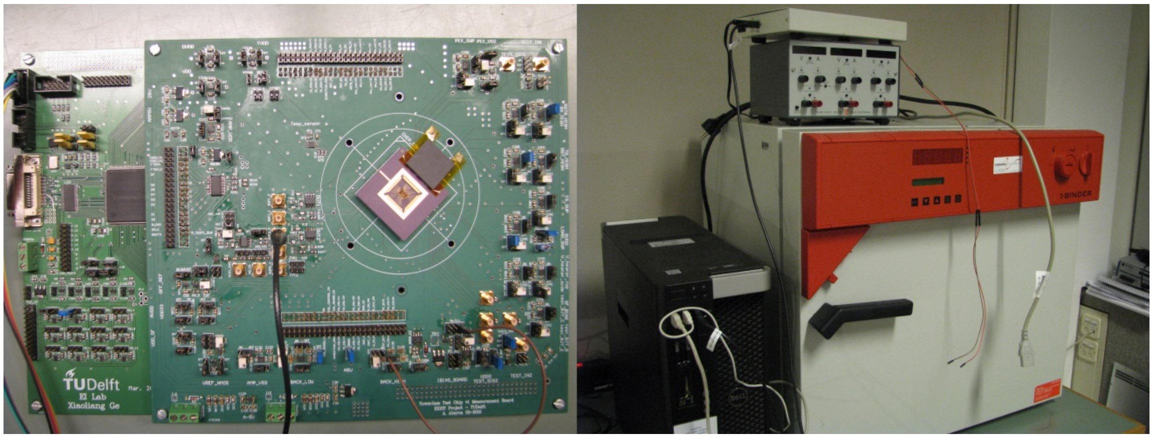

Figure 4-21: Measurement setup (PCB and oven).

4.5 Measurement Results

A micro-photograph of the chip is shown in Figure 4-22. The figure shows the different circuit blocks of the chip. The image sensor is located in the top middle part of the picture. Here it is possible to see the presence of the Tixels along the array (in light orange). Below the image sensor, the column amplifier and the output buffer are presented. Row and column decoders are placed to the left of the image sensor.

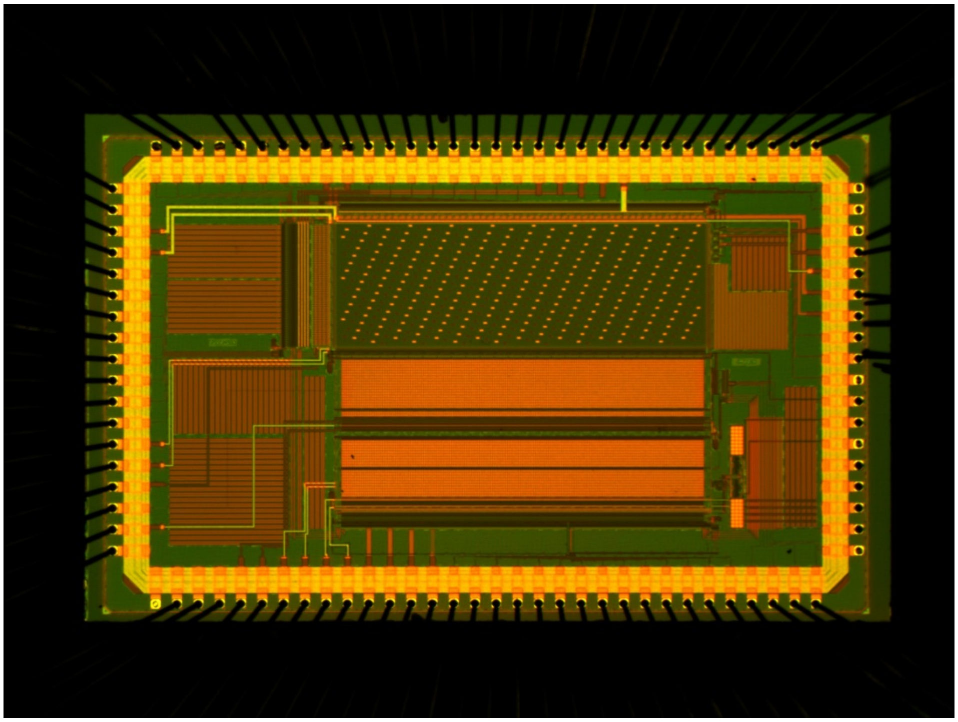

Figure 4-22: Micro-photograph of the chip.

4.5.1 Image Sensor

A picture taken by the image sensor is shown in Figure 4-23. The black dots prove the presence of the temperature sensors along the array. This picture essentially confirms that the image sensor as well as the readout system work.

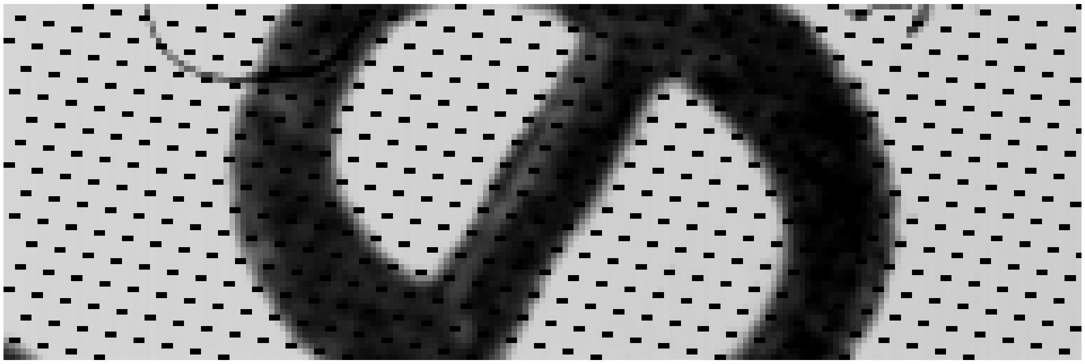

Figure 4-23: Picture taken by the image sensor.

One of the parameters that have been measured is the conversion gain. This measurement was done at room temperature (RT) under constant exposure to light. The value of the conversion gain is 71.57 µV/e^-, which is used to calculate the dark current of the image sensor in terms of electrons (e^-).

The dark current has been measured over time and temperature. The dark current was calculated by averaging 100 frames and the outputs of 10,000 pixels. It was obtained at 30 °C over the exposure time range of 0.05 s to 5 s. Figure 4-24 (a) shows the average dark signal vs. time. The dark current corresponds to the slope of S_{dark} and it has a value of 120 e^-/s at 30 °C.

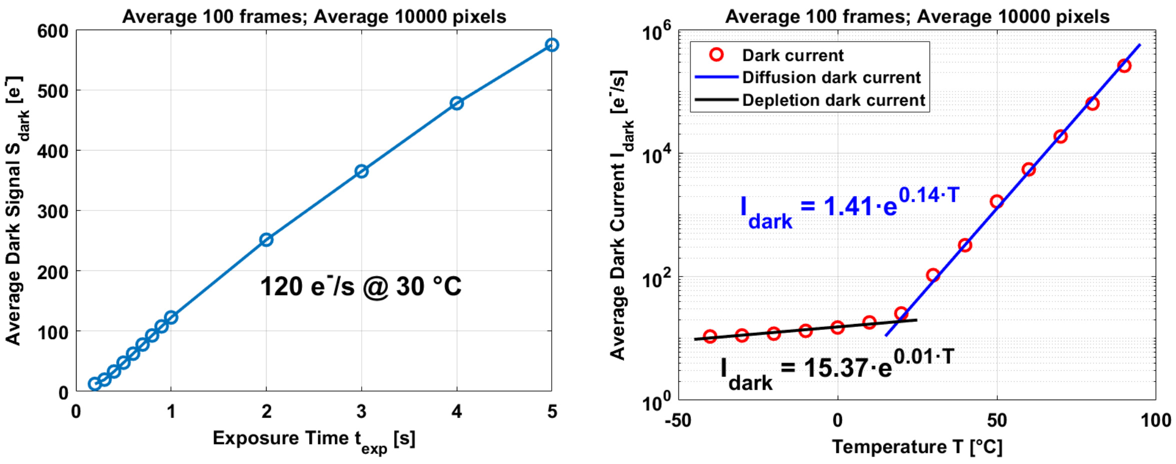

(a)

(b)

Figure 4-24: (a) Dark signal vs. time. (b) Dark current vs. temperature.

The dark current has been also measured in the temperature range of -40 °C to 90 °C in steps of 10 °C. By averaging 100 frames and 10,000 pixels. The average dark current exhibits two different slopes, as shown in Figure 4-24 (b). Both curves increase exponentially but with a different rate depending on the temperature range. Between -40 °C and 10 °C, the dark current increases 1.09 times every 5 °C while in the range of 20 °C to 90 °C the dark current increases 2 times every 5 °C.

Usually, two dominant dark current mechanisms are considered: at low temperatures the depletion dark current dominates [16], [17]; and at high temperatures diffusion dark current is the dominant mechanism [17], [18]. In both regimes, the dark current exhibits exponential behavior: increasing ~1.5 times every 5 °C at low temperatures, while at high temperatures the dark current increases ~2 times every 5 °C [16], [18], [19]. At temperatures higher than 10 °C, the pixel-Tixel sensor shows a specific type of behavior where the diffusion dark current dominates. However, at low temperatures it seems that the depletion dark current is not the only (or the dominant) mechanism involved because the increment is only 1.09 times per 5 °C instead of ~1.5 times per 5 °C. Also, if the dark current is extrapolated for low temperatures (by using the values at high temperature and following the behavior of 1.5 times per 5 °C), the extrapolated results are considerably lower than the measured values. The cause of the higher dark current values and the lower increment in temperature might be due to two different effects: It has been observed that during measurements in dark (between -40 °C and 90 °C), pixels next to Tixels have a higher output signal compared to those farthest from the Tixels, as shown in Figure 4-25 (a). A similar effect has been reported when BJTs or diodes next to the image array generate charge that cause an increment in the output signal of the pixels [20], [21]. Additionally, the voltage dependency of the dark current on the level of the floating diffusion has been measured at -20 °C and at four different voltage levels: 2.5 V, 2.8 V, 3.0 V, and 3.3 V. Figure 4-25 (b) shows the voltage dependency of the dark signal, which increases as the voltage level increases. This could point to the presence of tunnelling current at the floating diffusion level. These two effects might add extra signal to the depletion dark current at low temperatures, leading to higher levels of dark current and an increment of only 9% every 5 °C (Figure 4-24 (b)).

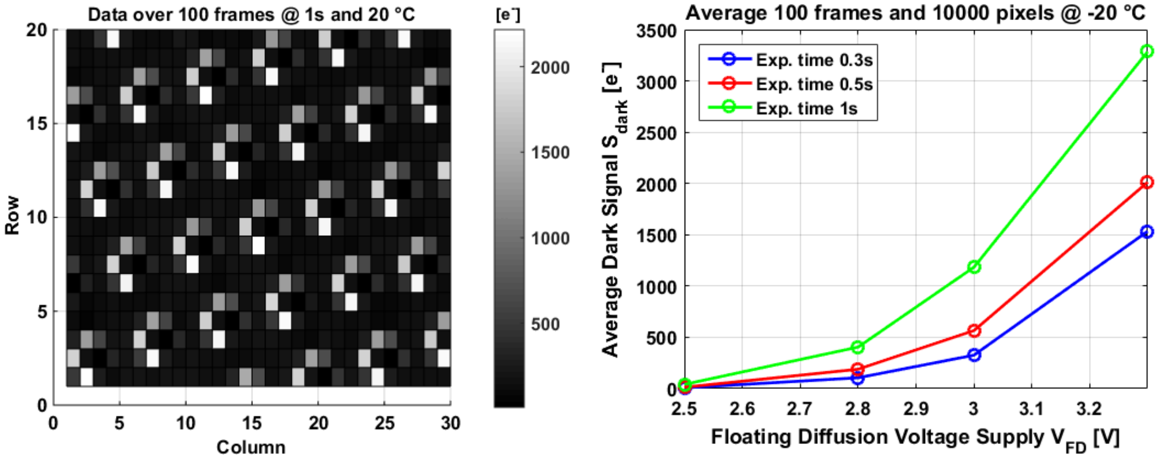

(a) (b)

Figure 4-25: (a) Presence of hot pixels next to the Tixels. (b) Dark current dependency on the level of the FD voltage supply.

4.5.2 Temperature Sensor

Temperature measurements have been carried out using two different temperature control ovens: a Binder FP53 over the temperature range of 20 °C to 90 °C in steps of 10 °C; and a Vötsch model VT7004 over the temperature range of -40 °C to 90 °C in steps of 10 °C. In both cases the chip was placed on top of a massive aluminium block to stabilize the temperature, reaching a stability of 0.015 °C. As a reference the temperature of the chip-Al block was measured/controlled by a calibrated Pt-100 thermistor (used in both ovens to avoid errors in the reference temperature data). Two different gains of the on-chip PGA were used: Gain 16 (G16) and Gain 8 (G8). Four different chips were tested (C1, C2, C3, and C4). In order to cancel thermal noise, 100 frames were taken and averaged to obtain the temperature coefficient and the inaccuracy.

All Tixels of chip sample C1 have been plotted between 20 °C and 90 °C in Figure 4-26 (a). Figure 4-26 (a) shows that the output signal (V_{out}) of all Tixels is linear between 20 °C and 90 °C. The V_{out} - temperature coefficient of the Tixels is between 1.21 mV/°C and 1.23 mV/°C. Its standard deviation is 0.7% from the average value of 1.22 mV/°C. All Tixels have almost the same relative temperature variation. This means that it would be possible to measure temperature variations with any Tixel in the pixel array.

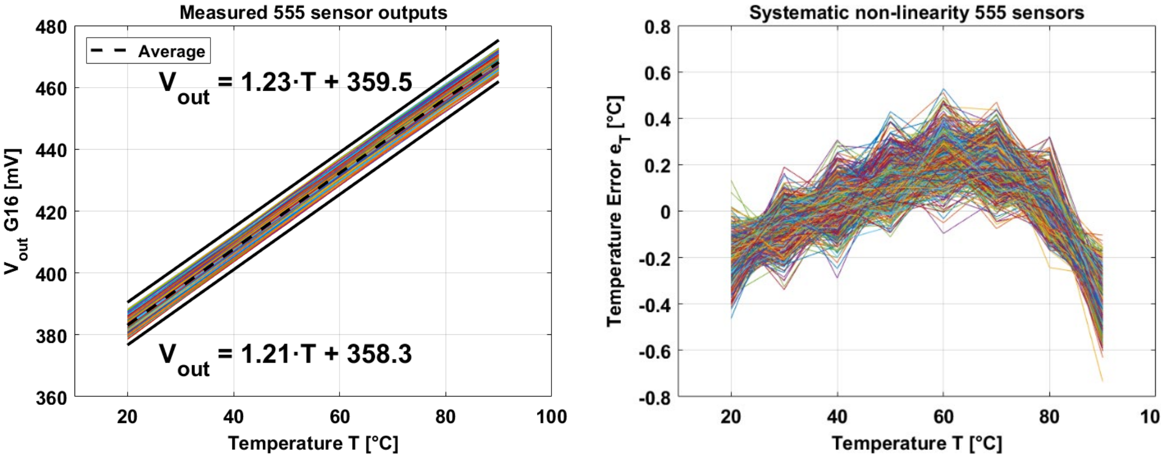

(a) (b)

Figure 4-26: (a) Temperature behavior of the 555 Tixels of chip C1 using a gain of 16. (b) Systematic non-linearity error of chip C1 after 1st order curve fitting.

The systematic non-linearity of the Tixel after a 1st order curve correction is shown in Figure 4-26 (b). The non-linearity has a value of ±0.8 °C, which is similar to simulations.

The inaccuracy of the Tixels was calculated after correction of the non-linearity and applying a 5th order polynomial. This result is shown in Figure 4-27.

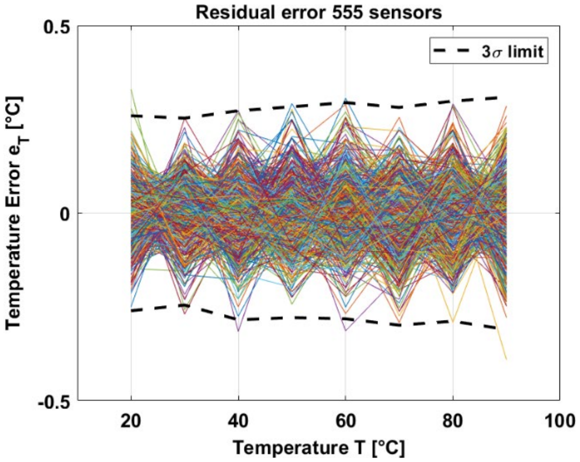

Figure 4-27: Inaccuracy of the temperature sensors after systematic non-linearity removal and a 5th order polynomial.

The 555 Tixels of C1 exhibits an inaccuracy (3σ) of ±0.3 °C. This is comparable to simulations. This level of inaccuracy implies that it is possible to obtain the temperature distribution of the pixel array in order to compensate for dark current.

Four different chips have been measured between 20 °C and 90 °C by using G16 and G8. In the case of G16, and averaging 555 Tixels per chip, the four chips show a high linearity in this temperature range (Figure 4-28 (a)). The temperature coefficient of all the chips has an average value of 1.22 mV/°C with a standard deviation of 0.8% from the average coefficient. The non-linearity error has been calculated by using a 1st order curve fitting (Figure 4-28 (b)).

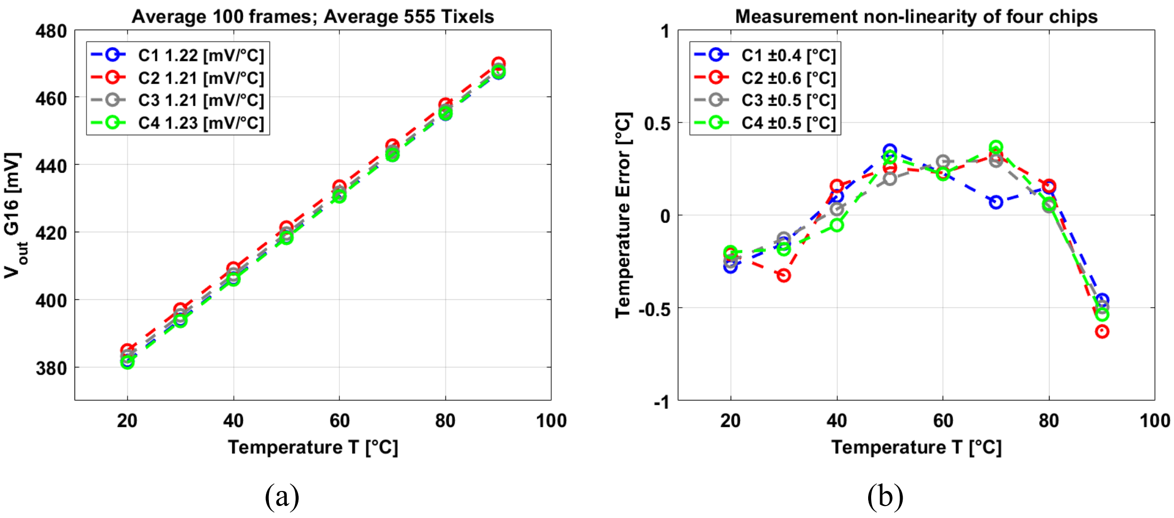

Figure 4-28: (a) Temperature behavior of four chips averaging 100 frames and 555 Tixels using a gain of 16. (b) Systematic non-linearity error after a 1st order curve fitting.

The non-linearity error of the four chips shows a similar behavior, with a maximum error of ±0.6 °C for chip C2. The inaccuracy of the four chips was calculated and is shown in Figure 4-29.

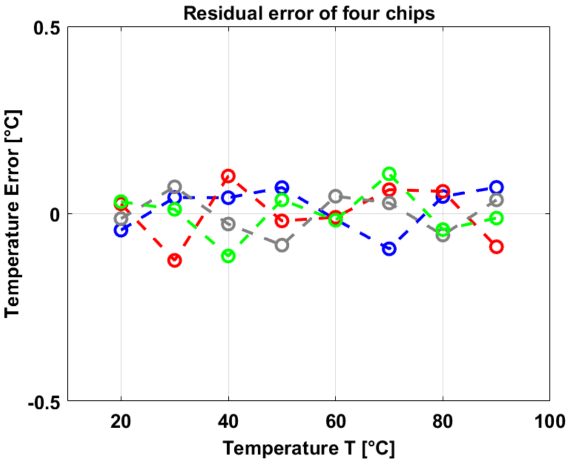

Figure 4-29: Inaccuracy of the four chips after systematic non-linearity removal and a 5th order polynomial, using a gain of 16.

The four chips exhibits an inaccuracy of ±0.12 °C after systematic non-linearity removal and applying a 5th order curve fitting.

The same measurements have been done but using G8. In this case, the V_{out} - temperature curve also exhibits high linearity (Figure 4-30 (a)). The average temperature coefficient of the four chips has a value of 0.66 mV/°C with a deviation of 2% from the average. This deviation of 2% from the average might be due to fabrication process variation. When comparing the deviations of G16 and G8, applying a higher gain in the first stage of the column amplifier helps to reduce the temperature coefficient deviation when comparing different chips.

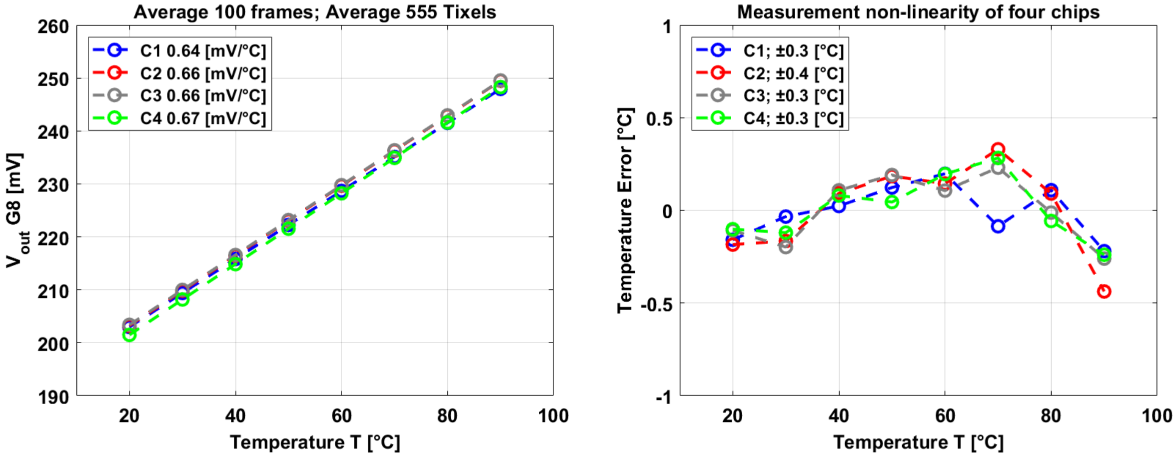

(a) (b)

Figure 4-30: (a) Temperature behavior of four chips averaging 100 frames and 555 Tixels using a gain of 8. (b) Systematic non-linearity error after a 1st order best curve fitting.

The maximum non-linearity error after a 1st order best curve fitting is 0.4 °C for chip C2. Also, the inaccuracy of the four chips using gain 8 was calculated and is shown in Figure 4-31.

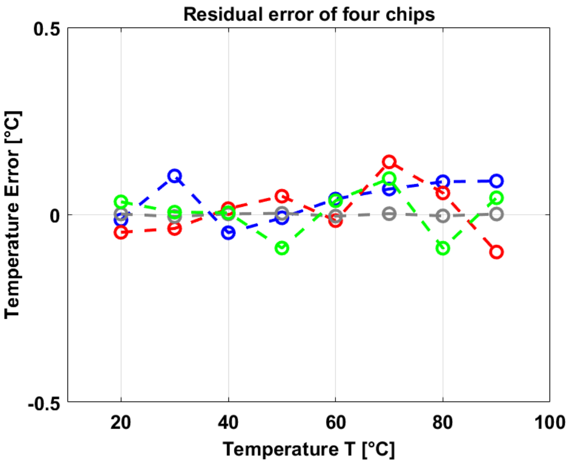

Figure 4-31: Inaccuracy of the four chips after systematic non-linearity removal and a 5th order polynomial, using a gain of 8.

The four chips exhibits an inaccuracy of ±0.12 °C after the systematic non-linearity removal and applying a 5th order curve fitting. In each chip, the 555 Tixels were averaged.

The results from comparing four chips imply that the dark current can be compensated in each chip obtaining a similar level of compensation.

4.5.2.1 Resolution of the Temperature Sensors

In this design an off-chip 16-bit ADC was used [15]. This ADC is especially designed for CMOS image sensor applications. The dynamic range of the ADC used in these measurements corresponds to 2 V. This means an LSB is equal to $2/2^{16} \approx 30\mu V$. If the temperature coefficient of 1.2 mV/°C is used, then an LSB is equal to $30\mu V = 0.025$°C. Thus, 1 digital number (DN) corresponds to $30\mu V$ (or 0.025°C).

The resolution was obtained by using the temperature measurements (at 30 °C) over time (frames). There are 100 frames and each frame contains 555 temperature sensors. Each frame is obtained every 278 ms (thus 100 frames in 27.8 s). This means a conversion time of 0.5 ms per temperature sensor. Figure 4-32 (a) shows the temperature measurement over time (100 frames) of a single temperature sensor after averaging multiple times (100).

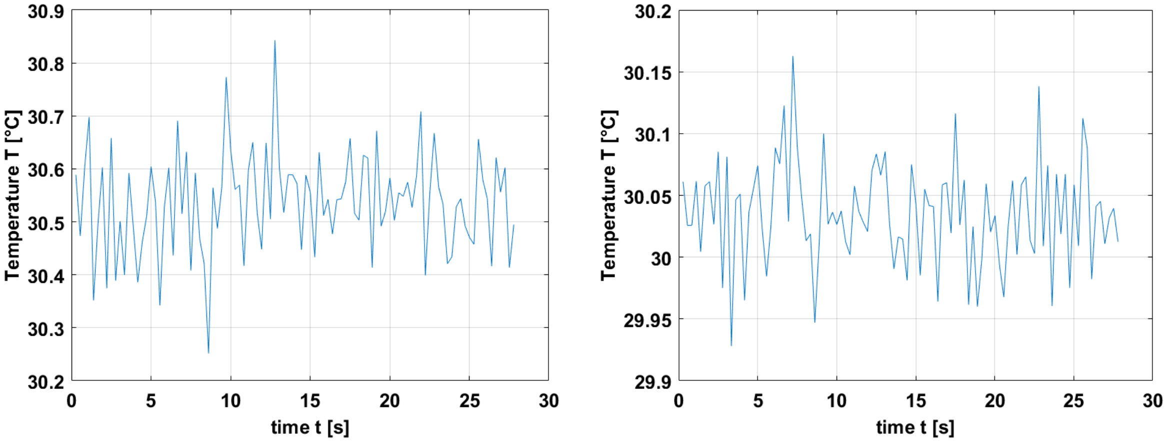

(a) (b)

Figure 4-32: (a) Temperature over time of a single sensor. (b) Temperature over time averaging 555 sensors.

The standard deviation of Figure 4-32(a) corresponds to 0.1 °C. This value corresponds to the resolution. Figure 4-32 (b) shows the temperature over time when 555 sensors were averaged. In this case, the standard deviation corresponds to 0.043 °C. However, the conversion time is 278 ms instead of 0.5 ms.

The main characteristics of the Tixel are shown in Table 4-2.

Table 4-2: Characteristics of the Tixel from 20 °C to 90 °C.

Characteristic	Value
Resolution (°C)	0.1
3σ Inaccuracy (°C)	±0.3
Range (°C)	20 to 90
Conversion Time (ms)	0.5
Area (μm^2)	11 × 22
Technology (μm)	0.18 CIS
Power (μW)	110
Energy per Conversion (nJ)	55

4.6 Conclusions

Temperature sensors have been integrated in an image array with 555 Tixels uniformly distributed along the array. The Tixels are based on parasitic BJTs. Results have shown that both sensors work by using the same readout system as well as the same control signals to collect the data of the regular pixels. The image sensor has a dark current of 120 e^-/s at 30 °C. The dark current of the image sensor increases 1.09 times every 5 °C in the temperature range of -40 °C to 10 °C and 1.9 times every 5 °C in the range of 20 °C to 90 °C. The dark current behavior at low temperatures seems to have other mechanisms involved (not only due to depletion dark current) as measurements show. These other mechanisms might be charge-generated in the Tixels and/or tunnelling current on the floating diffusion. These two effects could add extra signal to the dark current at low temperatures where they dominate over the depletion dark current. On the other hand, at high temperatures these two effects might also add extra signal to the dark current, but to a lesser extent than in the case of the depletion dark current. If the dark current (depletion + charge sharing + tunnelling) at low temperatures is extrapolated for high temperatures, then these extrapolated values are much lower compared to the dark current measured at high temperatures. The dark current behavior at high temperatures is due to diffusion dark current as dominant mechanism.

The Tixels show high linearity between 20 °C and 90 °C, both individually and as a combined average. Individually, every Tixel in chip C1 can measure almost the same relative temperature variations across the array because their temperature coefficient only exhibits a standard deviation of 0.7% from the average. The average temperature coefficient in C1 is 1.22 mV/°C and the inaccuracy of the 555 Tixel across the pixel array is ±0.3 °C after systematic non-linearity removal and applying a 5th order polynomial.

Comparing four chips and using a gain of 16, the average conversion coefficient is 1.22 mV/°C with an inaccuracy of ±0.12 °C after systematic non-linearity removal and a 5th order polynomial. Using G8, the conversion coefficient is 0.66 mV/°C with an inaccuracy of ±0.25 °C.

These results have shown that the dark current can be compensated by using the Tixel measurements. On the one hand, this is possible because the dark current of this image sensor is temperature-dependent, and the absolute temperature and temperature distribution of the pixel array can be measured by the output signals of the Tixels.

Acknowledgements

The authors wish to acknowledge TowerJazz for the prototypes of the CIS devices. The research is part of the CISTERN project (a European ECSEL Joint Undertaken project), funded by the Dutch Government.

References

[1] X. Wang, "Noise in sub-micron CMOS image sensors," Ph.D. Dissertation, Delft University of Technology, pp. 46-68, 2008.

[2] P. S. Baranov, V. T. Litvin, D. A. Belous, and A. A. Mantsvetov, "Dark current of the solid-state imagers at high temperature," in *IEEE Conference of Russian Young Researchers in Electrical and Electronic Engineering (EIConRus)*, 2017: IEEE, pp. 635-638.

[3] S. W. Han and E. Yoon, "Low dark current CMOS image sensor pixel with photodiode structure enclosed by P-well," *Electronics Letters,* vol. 42, no. 20, pp. 1145-1146, 2006.

[4] R. Coath, R. Turchetta, J. Crooks, M. Wilson, and A. Godbeer, "Advanced pixel architectures for scientific image sensors," *Proceedings, Topical Workshop on Electronics for Particle Physics (TWEPP09),* pp. 57-61, 2009.

[5] A. Godbeer, "Investigation of 4T CMOS image sensor design and the effects of radiation damage," *MPhys Dissertation, Department of Physics, University of Surrey, United Kingdom,* pp. 14-15, 2010.

[6] E. R. Fossum and D. B. Hondongwa, "A Review of the Pinned Photodiode for CCD and CMOS Image Sensors," *IEEE Journal of the Electron Devices Society,* vol. 2, pp. 33-43, 2014.

[7] X. Ge and A. J. P. Theuwissen, "A 0.5erms− Temporal Noise CMOS Image Sensor With Gm-Cell-Based Pixel and Period-Controlled Variable Conversion Gain," *IEEE Transactions on Electron Devices,* vol. 64, no. 12, pp. 5019-5026, 2017.

[8] S. Xie and A. Theuwissen, "Compensation for Process and Temperature Dependency in a CMOS Image Sensor," *Sensors,* vol. 19, no. 4, pp. 870-885, 2019.

[9] K. Souri, Y. Chae, and K. A. A. Makinwa, "A CMOS Temperature Sensor With a Voltage-Calibrated Inaccuracy of ±0.15 °C (3σ) From -55 °C to 125 °C " *IEEE Journal of Solid-State Circuits,* vol. 48, no. 1, pp. 292-301, 2013.

[10] G. C. M. Meijer, G. Wang, and F. Fruett, "Temperature sensors and voltage references implemented in CMOS technology," *IEEE Sensors Journal,* vol. 1, no. 3, pp. 225-234, 2001.

[11] M. A. P. Pertijs, K. A. A. Makinwa, and J. H. Huijsing, "A CMOS smart temperature sensor with a 3σ inaccuracy of ±0.1 °C from -55 °C to 125 °C," *IEEE Journal of Solid-State Circuits,* vol. 40, no. 12, pp. 2805-2815, 2005.

[12] M. A. P. Pertijs and J. H. Huijsing, *Precision temperature sensors in CMOS technology*. Springer, 2006, pp. 11-46.

[13] J. Tan, "4T CMOS Active Pixel Sensors under Ionizing Radiation," Ph.D. Dissertation, Delft University of Technology, pp. 28-29, 2013.

[14] S. K. Mendis *et al.*, "CMOS active pixel image sensors for highly integrated imaging systems," *IEEE Journal of Solid-State Circuits,* vol. 32, no. 2, pp. 187-197, 1997.

[15] "AD9826." [Online]. Available: https://www.analog.com/media/en/technical-documentation/data-sheets/AD9826.pdf.

[16] R. Widenhorn, M. M. Blouke, A. Weber, A. Rest, and E. Bodegom, "Temperature dependence of dark current in a CCD," in *Sensors and Camera Systems for Scientific, Industrial, and Digital Photography Applications III*, pp. 193-201.

[17] W. C. Porter, B. Kopp, J. C. Dunlap, R. Widenhorn, and E. Bodegom, "Dark current measurements in a CMOS imager," in *Sensors, Cameras, and Systems for Industrial/Scientific Applications IX*, 2008, pp. 1-8.

[18] K. Yasutomi, Y. Sadanaga, T. Takasawa, S. Itoh, and S. Kawahito, "Dark current characterization of CMOS global shutter pixels using pinned storage diodes," in *Proc. Int. Image Sensor Workshop—IISW*, 2011, pp. 8-11.

[19] H. I. Kwon, I. M. Kang, B. G. Park, J. D. Lee, and S. S. Park, "The Analysis of Dark Signals in the CMOS APS Imagers From the Characterization of Test Structures," *IEEE Transactions on Electron Devices,* vol. 51, no. 2, pp. 178-184, 2004.

[20] G. Meynants, W. Diels, J. Bogaerts, and W. Ogiers, "Emission microscopy analysis of hot cluster defects of imagers processed on SOI," in *Proc. Int. Image Sensor Workshop—IISW*, 2013, pp. 1-4.

[21] K. Seo, S. Lee, P. Ahn, D. Kim, and K. Cho, "A study on photon effect to image plane," in *Proc. Int. Image Sensor Workshop—IISW*, 2017, pp. 176-179.

5 nMOS-BASED TEMPERATURE SENSORS IN A CMOS IMAGE SENSOR

This chapter of the thesis is based on the publications:

A. Abarca, A. Theuwissen, "In-Pixel Temperature Sensors with an Accuracy of ±0.25 °C, a 3σ Variation of ±0.7 °C in the Spatial Domain and a 3σ Variation of ±1 °C in the Temporal Domain," *Micromachines* 2020, vol. 11, no. 7, 665.

This chapter presents the use of the 4 transistor (4T) pixel, for both imaging and temperature measurement. Also, 20 BJT-based temperature sensors (Tixels) have been integrated into the CMOS image sensor in order to compare both types of temperature sensors and their effect on the dark signal of the pixel array. The intended use of these temperature sensors is the compensation of dark (current) fixed pattern noise (FPN) in a CMOS image sensor (CIS). The temperature sensors are based on a substrate parasitic bipolar junction transistor (BJT) and on an nMOS source follower of the pixel. Compared to the design presented in the previous chapter, the area of the BJT-based was reduced to one pixel area, while the nMOS-based incurs in no additional area. In order to achieve an inaccuracy compared to the previous chapter, different techniques are used: dynamic element matching (DEM), an on-chip temperature-compensated bias current, correlated double sampling (CDS), and using bandgap reference (BGR) to bias the gain amplifier. The average temperature coefficient of the BJT-based temperature sensor corresponds to 1.08 mV/°C, achieving an inaccuracy (3σ) of ±0.5 °C after systematic non-linearity removal and a 1st order best curve fitting. In the case of the nMOS-based temperature sensor, an average temperature coefficient of 1.07 mV/°C and an inaccuracy (3σ) of ±0.55 °C have been achieved. The temperature range is between −40 °C and 90 °C.

5.1 Introduction

Nowadays, CMOS image sensors are widely used in different applications such as astronomy, medicine, and above all in mobile phones [1], [2], [3]. For many years charge coupled devices (CCDs) dominated the field of image sensors in a variety of related applications. However, the active pixel sensor (APS) has emerged as a replacement for CCDs [4]. Over the last few decades, efforts have focused on improving the performance of the APS. Currently, the APS has several advantages over a CCD, such as: lower cost, lower power consumption, higher dynamic range, and higher integrability [5], [6], [7]. At the same time, CMOS-based temperature sensors are used in many applications such as on-chip thermal control, human body temperature monitoring, processor speed monitoring, and even in food monitoring [8], [9], [10]. The dark current or leakage current of the CIS is one of the major contributors of FPN and becomes significant under low light conditions and high temperature variations. The dark current linearly depends on the integration time of the pixels and exponentially on the temperature [11]. In fact, the dark current doubles every ~5–10 °C [12], [13], [14]. Different techniques are applied to compensate for the dark current. The most common one is to take a dark reference frame at the beginning of the picture acquisition, at a certain exposure time with closed mechanical shutter, and then subtracting this dark reference frame from the following images. However, the temperature must be kept constant during the acquisition, otherwise the dark current level changes and a new dark reference frame should be taken. Also, modifications of the photodetector at the physical level have been made to reduce the effect of the dark current, for instance, by adding a p-well layer around the pixel [15].

In the previous chapter, the concept of integrating BJT-based temperature sensors (Tixels) has been demonstrated. Nevertheless, Tixels replace a pixel in the pixel array, thus, resulting in a dead pixel. Also, the Tixel affects the dark signal of those pixels next to the BJT-based, exhibiting a higher dark signal compared to those pixels far from the Tixel. This chapter presents the use of the pixel itself as a temperature sensor, thus, no additional area is used and the dark signal is not affected. Also, improvements in the in-pixel temperature sensors by implementing DEM, CDS, and on-chip temperature-compensated bias current and voltage references, as well as sequential series-resistance compensation to increase the accuracy of the temperature sensors over a wider temperature range.

This chapter is organized as follows. Section 5.2 briefly explains the architecture of the sensor including the temperature sensors. In Section 5.3, sources of inaccuracy in temperature sensors are discussed. The circuits to overcome the sources of inaccuracy are presented in Section 5.4. In Section 5.5, measurement results are presented. A conclusion is given at the end of this chapter.

5.2 CMOS Image Sensor with In-Pixel Temperature Sensors

A block diagram of the prototype CIS device is shown in Figure 5-1. The sensor is composed of row and column decoders, a pixel array of 60 × 140 pixels, and a readout circuit. Temperature measurements can be performed either by the substrate parasitic bipolar or by the pixel itself via the source follower (SF) transistor. In the pixel array, 20 pixels have been replaced with Tixels, which can perform temperature measurements simultaneously as the pixels at the cost of one dead pixel at the location of each Tixel. In the case of the nMOS SF temperature sensor (nSFTS), it is the pixel itself that performs both temperature and video measurements, but in different phases, thus incurring a lost frame when all the pixels are used as temperature sensors. Pixels and Tixels use the same readout system (Figure 5-1) composed of a programmable gain amplifier (PGA), a sample and hold (S/H) circuit, an output buffer, and an off-chip 16-bit ADC.

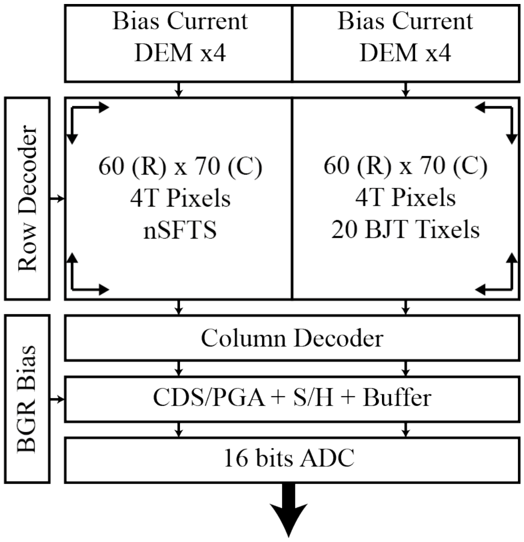

Figure 5-1: Block diagram of the CMOS image sensor being tested. There are 60 rows (R) and 140 columns (C).

5.2.1 Parasitic Bipolar Temperature Sensor

The Tixel is based on a substrate (or vertical) parasitic pnp BJT connected in a common collector configuration. The emitter area of the BJT corresponds to 5×5 μm^2. The Tixels are placed in the same layer as the pixels and they (Tixels and pixels) share the same readout system. The area of the Tixel was reduced to one pixel area of 11×11 μm^2 compared to the previous chapter with an area of 11×22 μm^2. The area was reduced by removing the source follower and using two switches to realize a readout scheme similar to that of a pixel. Its temperature information can be read at the same time as the pixels. Figure 5-2 (a) shows a schematic of the Tixel and Figure 5-2 (b) shows the layout of the Tixel surrounded by pixels.

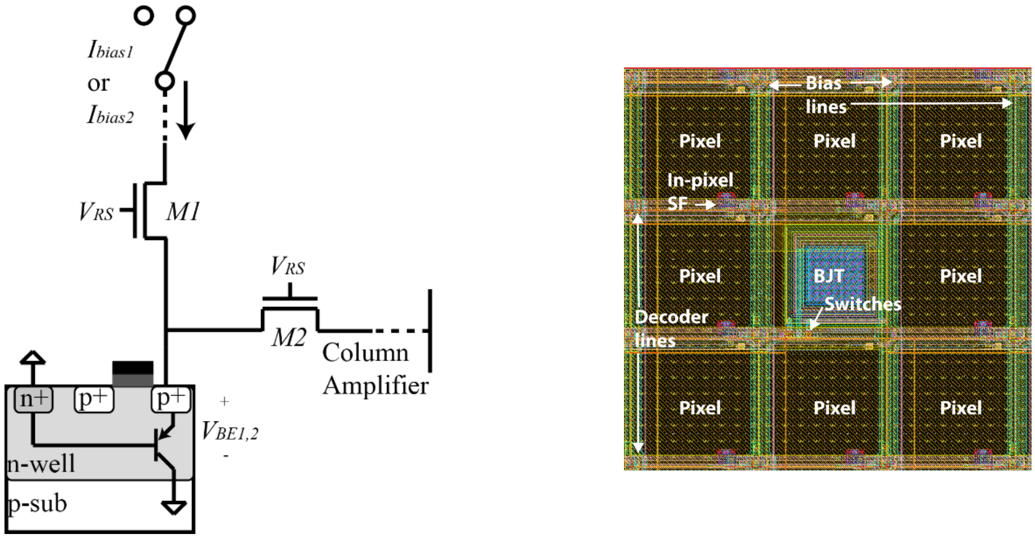

(a) (b)

Figure 5-2: (a) Schematic of the Tixel. (b) Layout of the Tixel surrounding by pixels.

In Figure 5-2 (a), I_{bias1} and I_{bias2} correspond to the bias currents of the BJT, and V_{RS} is the row select signal that controls the switches *M1* and *M2* turning the BJT on and off. The V_{RS} signal is the same for Tixels and pixels.

To avoid mismatch, only one BJT (instead of two) is used as a temperature sensor. The temperature is obtained via the differential base-emitter voltage (ΔV_{BE}) when the BJT is biased by two different currents in a ratio $N{:}1$ ($I_{bias2} = N \cdot I_{bias1}$). Equation (5-1) shows the ΔV_{BE}, which is proportional to absolute temperature (PTAT) [16]:

$$\Delta V_{BE} = \frac{kT}{q}\ln(N) \rightarrow T = \frac{\Delta V_{BE} \cdot q}{k \cdot \ln(N)} \tag{5-1}$$

where k is the Boltzmann constant, T corresponds to the absolute temperature, and q is the electric charge. The bias currents are generated by an internal DEM current mirror block together with an on-chip bias current, which provides 1 µA (Section 5.4.2).

5.2.2 nMOS Source Follower Temperature Sensor

The nMOS source-follower temperature sensor (nSFTS) is based on the pixel itself using the SF transistor as a temperature sensor. The use of CIS pixels for temperature sensing incurs in no additional area and does not affect the dark signal measurements, as in the case of the Tixels. The pixel is based on a classical 4T architecture and the size is 11×11 μm^2. Figure 5-3 (a) shows a schematic of the nMOS SF temperature sensor based on the 4T pixel architecture [17], [18]. The layout of the nMOS SF temperature sensor (and 4T pixel) is shown in Figure 5-3 (b).

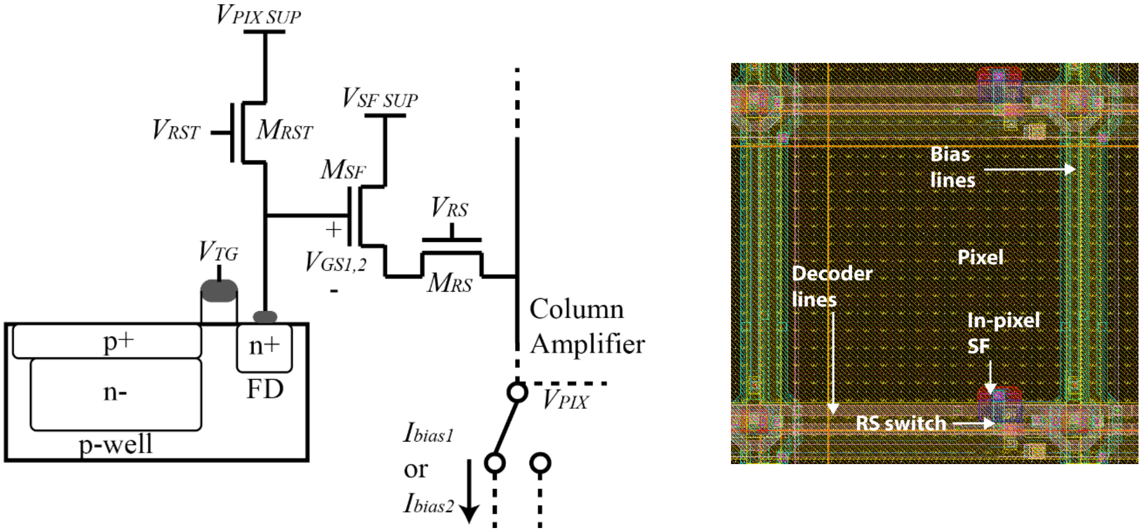

(a) (b)

Figure 5-3: (a) Schematic of the nMOS SF temperature sensor (and pixel). (b) Layout of the nMOS SF temperature sensor (and pixel).

The operating principle of the pixel when it is used as a temperature sensor is as follows: When the row select transistor (M_{RS}) is turned on and the transfer gate transistor (M_{TG}) is turned off (to avoid any light induced charge which might disturb the floating diffusion (FD) node voltage), and when the voltage $V_{RST} > V_{PIX\_SUP} + V_{TH\_RST}$, then the gate voltage of the SF transistor (M_{SF}) equals to V_{PIX_SUP} and hence the pixel output voltage $V_{PIX} = V_{PIX\_SUP} - V_{GS}$ (if ignoring the voltage drop across M_{RS}). When an nMOS transistor is biased in the subthreshold region, it has an exponential characteristic in the form of:

$$I = I_{DS} \cdot e^{\frac{V_{GS}-V_{TH}}{nV_T}} \rightarrow V_{GS} = nV_T \ln\left(\frac{I}{I_{DS}}\right) - V_{TH} \tag{5-2}$$

where I is the column biasing, I_{DS} is the saturation current, V_{TH} is the threshold voltage of the SF transistor, n is a process dependent factor, and $V_T = kT/q$. If the pixel is biased by sequential ratiometric currents , the differential gate-source output voltage (ΔV_{GS}) (which is PTAT) is:

$$\Delta V_{GS} = V_{GS2} - V_{GS1} = n\frac{kT}{q}\ln(N) \tag{5-3}$$

where V_{GS2} and V_{GS1} correspond to the gate-source voltage when the SF transistor is biased at currents I_{bias2} and I_{bias1}, respectively, and $N = I_{bias2}/I_{bias1}$.

5.2.2.1 Design and Simulations of the nSFTS

Inside the pixel, the nMOS SF transistor occupies an area of 0.5 × 0.8 μm^2. The area of the nMOS SF transistor was chosen to maximize the fill factor of the pixel (Section 2.2.2).

The pixel (when it is used for imaging) is biased by a current generated from a Gm-cell, as shown in Figure 4-2 (Section 4.2.1.1). The Gm bias current varies from 4 μA at -40 °C to 11 μA at 90 °C. As stated in the previous chapter, this current was not used to bias the Tixel because the Gm bias current was out of the flat current-gain region at high temperatures. In order to realize if this current can be used for the pixel (when it is used for temperature sensing), the I-V characteristic of the nSFTS was simulated and is shown in Figure 5-4.

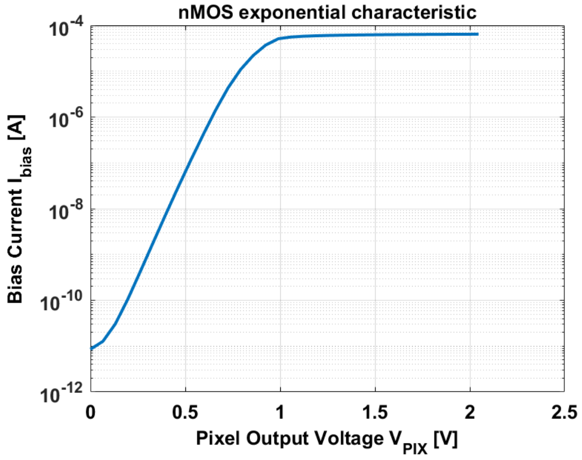

Figure 5-4: I-V characteristic of the nSFTS. V_{PIX} corresponds to V_{GS}.

The exponential characteristic of the nSFTS extends from 0.1 nA to 10 μA. The Gm bias current at room temperature is in the range of the exponential characteristic but at 90 °C is out of the exponential range. Also, to obtain ΔV_{GS}, the nSFTS has to be biased in a ratio N. For instance, if the ratio $N = 2$, then I_{bias2} should be 12 μA, which is out of the exponential range. In consequence, the Gm bias current will also not be used to bias the nSFTS (when it is used as temperature sensor).

The Tixel (of the previous chapter as well as in this chapter) is biased by a current mirror in the ratio 4:1 with a unit current of 1 µA. As the currents 1 µA and 4 µA are in the range of the exponential region of the nSFTS, it becomes natural to use the same currents to bias the nSFTS in order to compare both temperature sensors in similar conditions.

The temperature coefficient for various current ratios as well as the non-linearity after 1st order curve fitting are shown in Figure 5-5 (a) and (b), respectively.

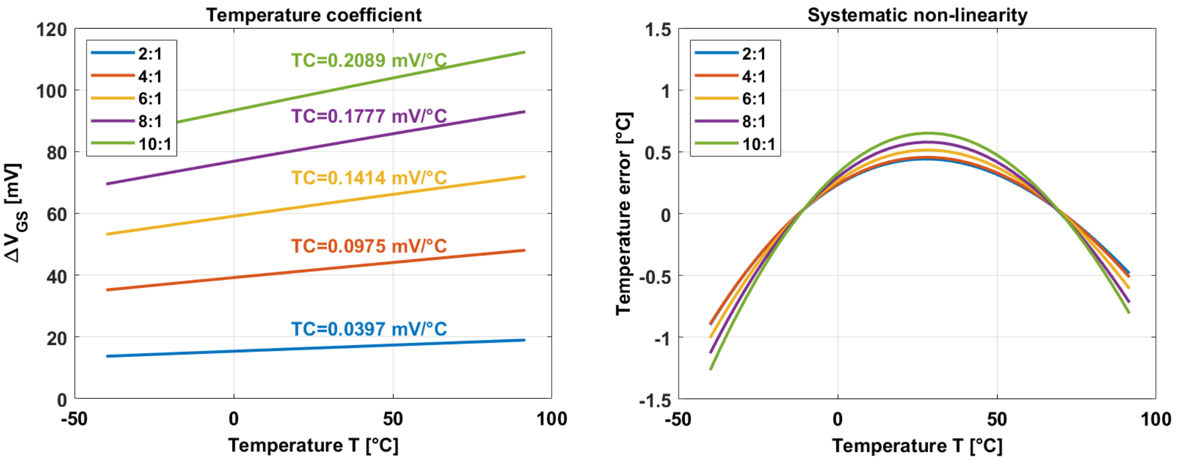

(a) (b)

Figure 5-5: (a) Temperature coefficient of the nSFTS for various current ratios with a unit current of 1 µA. (b) Systematic non-linearity error of the nSFTS after a 1st order curve fitting.

In Figure 5-5 (a), the temperature coefficient in the case of a current ratio 4:1 is ~1 mV/°C similar to the TC of the Tixel. Also, the systematic non-linearity error was calculated after applying a 1st order curve fitting. A 2:1 ratio would be better for linearity, but the difference with a 4:1 ratio is quite small. Besides, the 4:1 ratio offers a higher TC than the 2:1 ratio (comparable to the TC of the Tixel).

A Monte Carlo simulation was performed in order to determine the accuracy of the nSFTS (SF transistor + in-pixel transistors). In this simulation an ideal unit current of 1 µA and a current ratio 4:1 was used. Figure 5-6 shows the temperature coefficient and the systematic non-linearity over a temperature range of -40 °C and 90 °C.

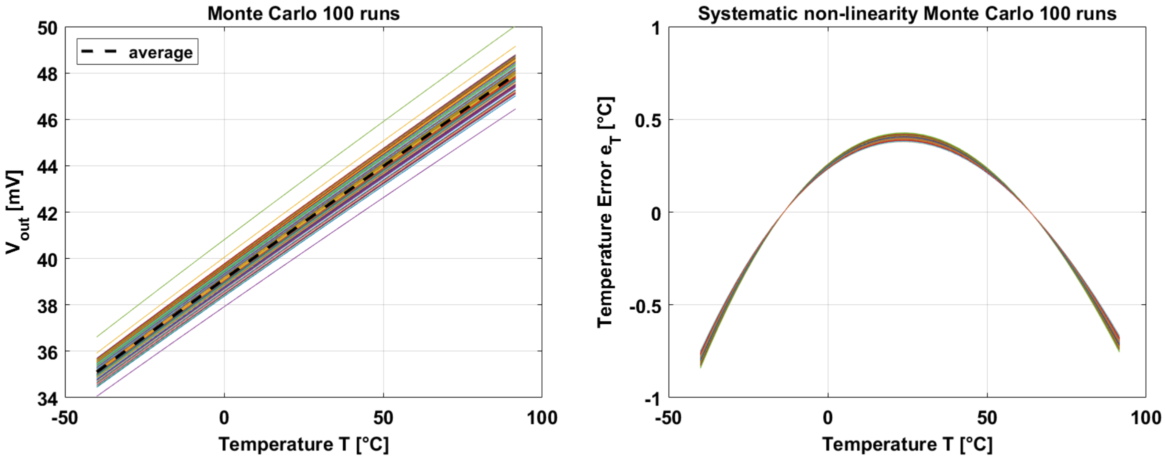

(a) (b)

Figure 5-6: Temperature coefficient of the nSFTS. (b) Systematic non-linearity error of the nSFTS after a 1st order curve fitting.

The output voltage of the nSFTS covers a range from 34 mV to 50 mV with an average temperature coefficient of 0.098 mV/°C, as shown in Figure 5-6 (a). The systematic non-linearity error of the nSFTS corresponds to ±0.8 °C after 1st order curve fitting and is shown in Figure 5-6 (b). After the systematic non-linearity correction, a 2nd order polynomial is applied in order to compensate for the remaining non-linearity and obtain the inaccuracy [19].

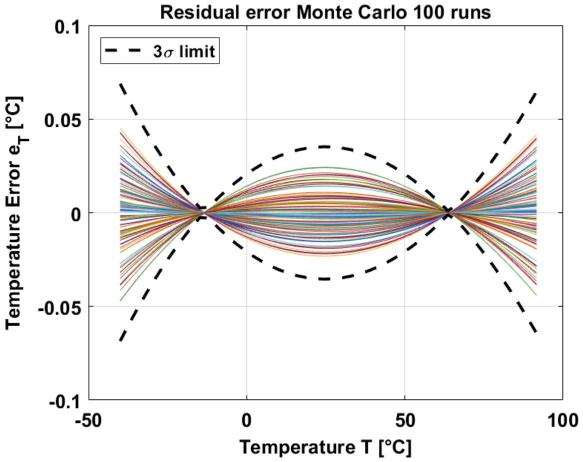

Figure 5-7: Inaccuracy of the nSFTS after systematic non-linearity removal and a 2nd order polynomial.

The inaccuracy of the nSFTS corresponds to ±0.065 °C (3σ).

5.3 Non-Linearities Affecting the Temperature Sensors

For both types of temperature sensors, non-linearities exist which affect the accuracy of the temperature measurement. In this section, the main sources of the inaccuracy are presented.

5.3.1 Sources of Inaccuracies in the BJT

As the temperature sensor is formed by only one BJT, it is the base-emitter voltage (V_{BE}) that is measured in every phase to calculate the PTAT ΔV_{BE}. The V_{BE} is highly influenced by the bias current I_{bias} and the saturation current I_S, as shown in Equation (5-4):

$$V_{BE} = \frac{kT}{q} \ln\left(\frac{I_{bias}}{I_S}\right). \tag{5-4}$$

From Equation (5-4), the influence of I_{bias} and I_S is clear, especially because they are both temperature-dependent [20], [21]. The influence of I_S can be trimmed out in a one-point calibration [21]. As in the previous chapter, the bias current is mirrored from a PTAT current source with a nominal value of 1uA at RT. When the sensors of the previous chapter were measured, an external current (on-PCB) biased the current mirror. However, due to the multiple bias of the chip, it was not possible to separate the main PCB from the socket of the chip. Thus, the complete PCB (chip + bias + FPGA) was also inside of the temperature controlled oven during temperature measurements. In consequence, the unit current source was also exposed to temperature variations. In order to reduce the temperature dependency of the unit current source, a more stable on-chip bias current generator was designed. The design of the bias current will be presented in Section 5.4.

5.3.2 Sources of Inaccuracies in the nSFTS

When the nMOS source follower-based temperature sensor is biased in the subthreshold region, the gate-source voltage V_{GS} follows Equation (5-5):

$$V_{GS} = n\frac{kT}{q} \ln\left(\frac{I_{bias}}{I_{DS}}\right) - V_{TH}. \tag{5-5}$$

Each nSFTS suffers from process variation due to the n factor, the small W/L size of each M_{SF} transistor, and the variations of I_{DS}. A technique to diminish the effect of the previous factors is proposed in [22], [23]. All the pixels in one column are selected to increase the actual device area of the nSFTS to mimic a larger parallel device by connecting the gates and sources to V_{PIX_SUP} and V_{PIX}, respectively. A larger device suffers less from process variations. Another consequence of this technique is the reduction in the output noise of the pixel, including thermal and flicker noise, due to the increment in the biasing current and W/L ratio of M_{SF} leading to a larger device area and hence increasing transconductance g_m.

The effect of mismatch between nMOS transistors is eliminated by using the fact that a single device instead of a differential pair is used for thermal sensing. However, the mismatches among the sensors still remain. This is caused by the following non-idealities (in addition to the I-V characteristic): the voltage drop across the M_{RS} switch, the body effect of V_{TH}, and the mismatches of the current mirrors. In the case of M_{RS}, the switch works in the linear region and its on-resistance is $1/\mu_n C_{ox}\left(V_{GS,RS} - V_{TH}\right)$ that varies with temperature and process. The body effect of V_{TH} is minimized by obtaining the differential gate-source voltage when the nSFTS is biased with sequential ratiometric currents. Besides, the proposed nSFTS outputs are normally close to the pixel supply voltage, e.g., around 2 V. This makes V_{SB} large and hence $\partial V_{TH}/\partial V_{SB} = \gamma/2\sqrt{2\Phi_F + V_{SB}}$ low [22]. The variation of the current mirrors can be overcome by using dynamic element matching.

As in the case of the BJT, the bias current has an impact on the value of V_{GS}. An accurate I_{bias} will be shown in Section 5.4.2.

5.3.3 Sources of Inaccuracies in the Readout System

The column amplifier adds a non-linearity to the output of the temperature sensor. One way to compensate for this temperature dependence is to derive all the biasing of the amplifier from bandgap references. Another source of inaccuracy is the reference voltage of the amplifier. If the reference is temperature-dependent, then the output signal is also affected when the temperature changes. The reference voltage has been replaced with an on-chip BGR. The architecture of the BGR bias voltage and reference voltage is explained in Section 5.4. Also, the offset in the column amplifier that can be canceled using CDS.

5.4 System Design

In Chapter 4, PTAT current mirror and CDS were used for the BJT-based temperature sensors. In this design, methods to compensate for the mismatch of the bias currents using DEM and a larger transistor area of the nSFTS are made. A block diagram of the temperature sensor is shown in Figure 5-8. This block diagram is valid for both types of temperature sensors (BJT and nMOS SF).

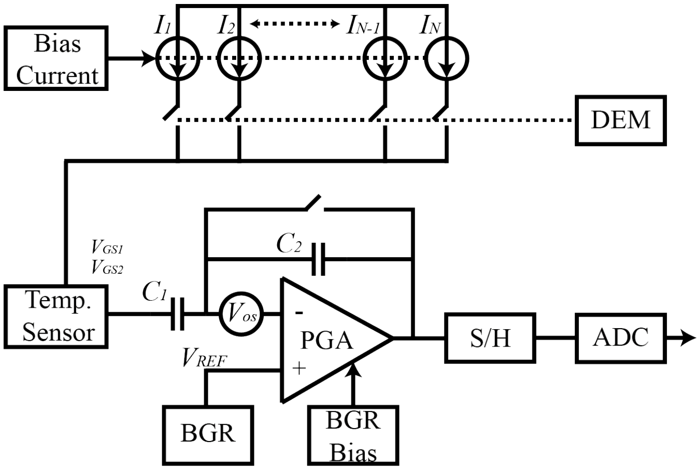

Figure 5-8: Block diagram of the system.

The system works as follows: the bandgap reference bias current (BGRBC) provides an on-chip bias current to the current mirror. As the temperature sensors (BJT and nSFTS) measure the temperature via the PTAT differential voltage, they need to be biased by two different currents in a ratio $N{:}1$. The current mirror composed of currents I_1 to I_N provides the current ratio for the temperature sensors. However, due to mismatch, the ratio is not exactly $N{:}1$, which leads to an error when comparing different temperature sensors of the same chip. The mismatch is canceled by using dynamic element matching, which averages the total current provided to the temperature sensor. By using DEM, the mismatch error can be reduced by at least one order of magnitude [21]. The output of the temperature sensor is read by a programmable gain amplifier (PGA), where a gain is applied. The PGA suffers from an offset voltage (V_{OS}) due to the mismatch of the transistors of the amplifier. To cancel V_{OS}, correlated double sampling (CDS) is applied by using the PGA and a sample and hold (S/H) circuit. Taking the nSFTS as an example, in one phase, the output voltage V_{GS1} is stored in C_1 and the offset plus the reference voltage ($V_{OS} + V_{REF}$) are sampled and stored in an analog memory in the S/H circuit. Then, in the next phase the output signal of the temperature sensor V_{GS2} is stored in C_1, obtaining the differential gate-source voltage ($\Delta V_{GS} = V_{GS2} - V_{GS1}$) which is amplified by the gain $G = C_1/C_2$ and stored with ($V_{OS} + V_{REF}$) in another analog memory in the S/H circuit. In this way, subtracting the stored values in both analog memories cancels the offset: $V_{out} = (G \cdot \Delta V_{GS} + V_{REF} + V_{OS}) - (V_{REF} + V_{OS}) = G \cdot \Delta V_{GS}$.

To reduce the temperature dependence of the PGA, bandgap references are used both to bias the PGA and as the reference voltage. In Section 5.4.3, a comparison between using the biasing of the previous chapter and the BGR bias will be shown.

5.4.1 Temperature-Compensated Resistor

In a BGR, resistors are used to set the proper temperature compensation for the output voltage. However, since resistors are also temperature-dependent, they affect the curvature of the output voltage and the total current.

The temperature-compensated resistor has been designed such that it reduces the effect of the temperature dependency of the resistors in the BGR. The resistor is shown in Figure 5-9 (a).

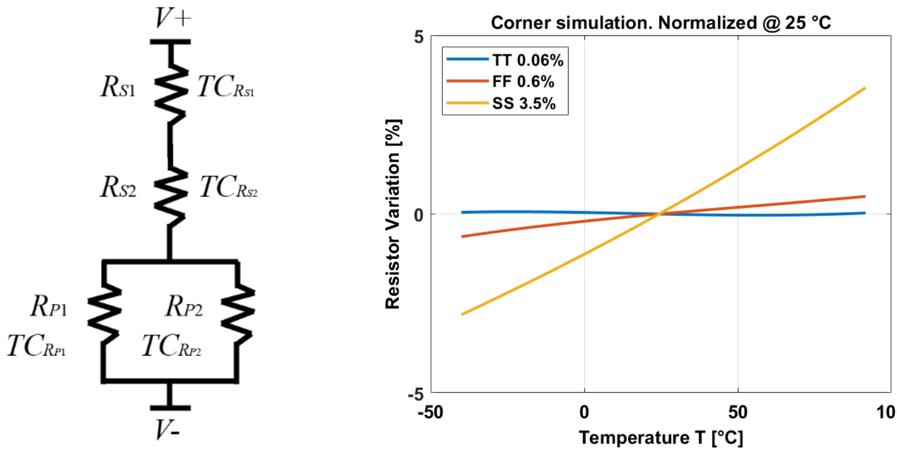

(a) (b)

Figure 5-9: (a) Schematic of the temperature-independent resistor. (b) Variation of the resistor in a temperature range between -40 °C and 90 °C.

The temperature-compensated resistor is composed of four resistors: two are in series (R_{S1} and R_{S2}) and the other two are in parallel (R_{P1} and R_{P2}). In both cases (series and parallel), resistors with different and opposing temperature coefficients (TCs) are used and connected to compensate each other. Resistors R_{S1} and R_{P1} are made by using the same highly doped polysilicon with a negative TC: $TC_{R_{S1}}$ and $TC_{R_{P1}}$, respectively (where $TC_{R_{S1}} = TC_{R_{P1}}$). Resistors R_{S2} and R_{P2} correspond to the same lowly doped polysilicon resistor with a positive TC: $TC_{R_{S2}}$ and $TC_{R_{P2}}$, respectively (where $TC_{R_{S2}} = TC_{R_{P2}}$). The total resistance (R_T) and the total TC are shown in Equations (5-6) and (5-7), respectively:

$$R_T = R_{S1} + R_{S2} + \frac{R_{P1}R_{P2}}{R_{P1} + R_{P2}} \tag{5-6}$$

$$\frac{\partial R_T}{\partial T} = 0 = R_{S1}TC_{R_{S1}} + R_{S2}TC_{R_{S2}} + \frac{R_{P1}R_{P2}\left(R_{P1}TC_{R_{P2}} + R_{P2}TC_{R_{P1}}\right)}{(R_{P1} + R_{P2})^2}. \tag{5-7}$$

Treating the series and the parallel resistors separately, the value of the resistors can be chosen by Equations (5-8) and (5-9):

$$\frac{R_{S1}}{R_{S2}} = \frac{TC_{R_{S2}}}{TC_{R_{S1}}} \tag{5-8}$$

$$\frac{R_{P1}}{R_{P2}} = \frac{TC_{R_{P1}}}{TC_{R_{P2}}}. \tag{5-9}$$

The curvature of the resistors in series is convex while the curvature of the resistors in parallel is concave. Combining both curvatures, the variation of the resistance over a -40 °C to 100 °C range results in a variation of 0.06 % in the TT corner, while the worst case is produced in the SS corner with a variation of 4 %, as shown in Figure 5-9 (b).

5.4.2 Bandgap Reference with Temperature-Compensated Resistors

A bandgap reference (BGR) is used to implement the bias current of the temperature sensors of the current mirrors, as well as both the bias and the reference of the PGA. The bandgap circuit is based on [24], [25]. The circuit of the BGR is shown in Figure 5-10 and the circuit of the OPA used in the BGR is shown in Figure 5-11.

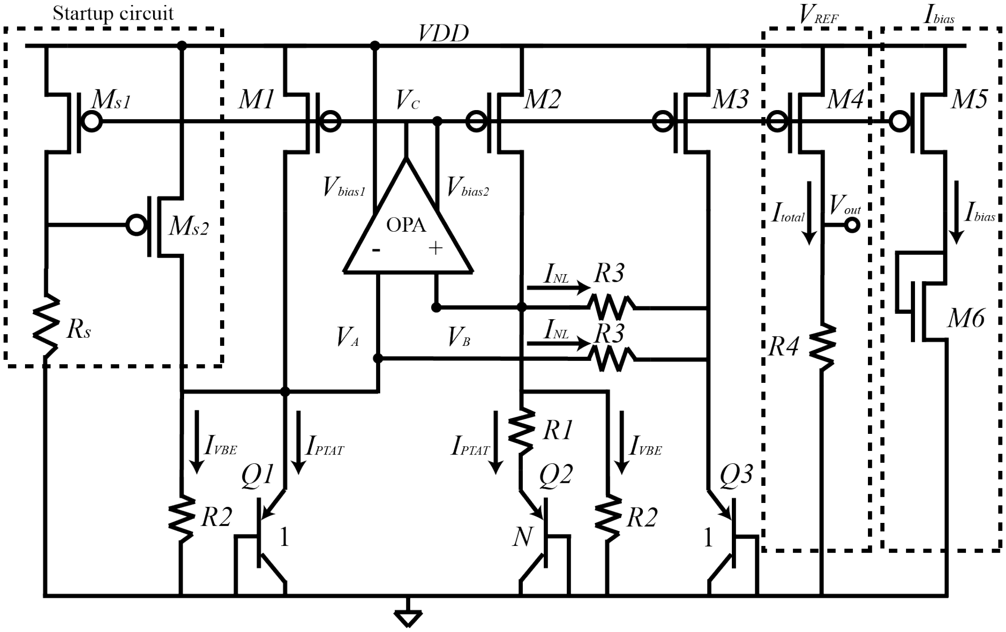

Figure 5-10: Block diagram of the bandgap reference used to generate temperature-independent voltages and temperature-independent bias current.

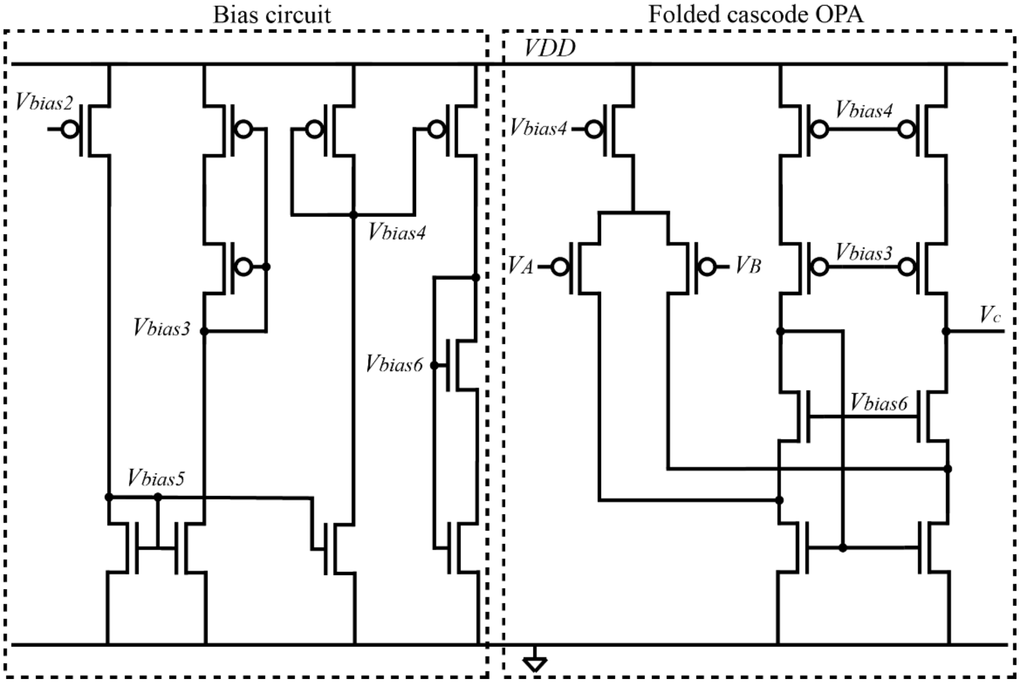

Figure 5-11: Folded cascode OPA used in the BGR.

The BGR of Figure 5-10 is based on the idea of properly combining currents that compensate each other to generate a temperature-compensated current at the output through the transistors *M4* (for output voltage) and *M5* (for output bias current). The BGR works as follows: the OPA forces voltages V_A and V_B to be equal, resulting in equal currents through transistors *M1* and *M2*. Transistors *Q2* and *Q1* have an emitter area ratio of N, generating a differential base-emitter voltage (ΔV_{BE}) and resulting in a PTAT current I_{PTAT} in $R1$. As resistors $R2.1$ and $R2.2$ are nominally identical, a current in $R2.1$ (and $R2.2$) (I_{VBE}) which is proportional to the base emitter-voltage of *Q1* (and *Q2*) is generated. The current I_{NL} is proportional to the differential base-emitter voltage between *Q1* and *Q3* in $R3.1$ ($R3.1 = R3.2$). Currents I_{PTAT} and I_{NL} are used to compensate the 1st order and higher order non-linearities of I_{VBE}, respectively. Therefore, the total current I_{total} in transistor *M4* is (for simplicity $R2.1 = R2.2 = R2$, and $R3.1 = R3.2 = R3$):

$$I_{total} = I_{VBE} + I_{PTAT} + I_{NL} = \frac{V_{BE}}{R2} + \frac{\Delta V_{BE}}{R1} + \frac{V_{BEQ1} - V_{BEQ3}}{R3} \tag{5-10}$$

where the value of I_{total} depends on the temperature behavior of resistors $R1$, $R2$, and $R3$.

This total current is temperature-compensated, which leads to a temperature-compensated output voltage as well. The output voltage V_{out} and its temperature coefficient are shown in Equations (5-11) and (5-12), respectively:

$$V_{out} = R4 \cdot I_{total} = R4\left(\frac{V_{BEQ1}}{R2} + \frac{\Delta V_{BE}}{R1} + \frac{V_{BEQ1} - V_{BEQ3}}{R3}\right) \tag{5-11}$$

$$\frac{\partial V_{out}}{\partial T} = 0 = R4\left(\underbrace{\frac{1}{R2}\frac{\partial V_{BEQ1}}{\partial T} + \frac{1}{R1}\frac{\partial \Delta V_{BE}}{\partial T}}_{first\ order} + \underbrace{\frac{1}{R3}\frac{\partial\left(V_{BEQ1} - V_{BEQ3}\right)}{\partial T}}_{higher\ order}\right). \tag{5-12}$$

Treating the 1st order TC and higher order TC of Equation (5-12) separately, the 1st order non-linearity is compensated by properly choosing the values of $R1$, $R2$, and N, satisfying Equation (5-13):

$$0 = \frac{1}{R2}\frac{\partial V_{BEQ1}}{\partial T} + \frac{1}{R1}\frac{\partial \Delta V_{BE}}{\partial T} = \frac{1}{R2}\,TC_{V_{BEQ1}} + \frac{1}{R1}\frac{k}{q}\ln(N) \tag{5-13}$$

$$\Rightarrow \frac{R2}{R1}\ln(N) = \frac{q}{k}\, TC_{V_{BE}} = 23.22$$

where $TC_{V_{BEQ1}}$ is the temperature coefficient of V_{BEQ1}, which is close to –2mV/°C.

On the other hand, the base-emitter voltage of a bipolar transistor can be also expressed as [26]:

$$V_{BE}(T) = V_{BG} - (V_{BG} - V_{BE0})\frac{T}{T_0} - (\eta - \alpha)V_T \ln\left(\frac{T}{T_0}\right) \tag{5-14}$$

where V_{BG} is the bandgap voltage of silicon, V_{BE0} corresponds to the base-emitter voltage at room temperature, T_0 corresponds to room temperature, η is a temperature constant dependent on technology (bipolar is around 4), α corresponds to the temperature dependence of the collector current (equal to 1 if the current is PTAT and equal to 0 if the current is temperature-independent [24]), and V_T is the thermal voltage equal to kT/q. The current I_{NL} can be expressed by using Equation (5-15):

$$I_{NL} = \frac{V_{BEQ1} - V_{BEQ3}}{R3} = \frac{V_T \ln\left(\frac{T}{T_0}\right)}{R3} \tag{5-15}$$

and the value of $R3$ can be chosen by comparing Equations (5-11) and (5-14), while using (5-15) [24]:

$$R3 = \frac{R2}{\eta - 1}. \tag{5-16}$$

The value of the resistors $R1$, $R2$, and $R3$ can be properly chosen by using Equations (5-13) and (5-16). The emitter area ratio of N is equal to 23, $R1$ = 50 kΩ, $R2$ = 400 kΩ, η is 4, and $R3$ = 135 kΩ.

5.4.3 Post-Layout Simulations of the BGR Current and BGR Voltage

The bias current is generated by properly scaling transistor *M5* in the BGR. In this way the bias current is: $I_{bias} = I_{total}/\frac{W}{L}$, where *W/L* is the size of transistor *M5*. A post-layout simulation shows that the BGR provides an almost constant current of 1 µA and temperature coefficient of 78.57 ppm/°C (TT corner) in the temperature range between −40

°C and 90 °C, as shown in Figure 5-12 (a). The worst case is produced in the SS corner, obtaining a temperature coefficient of 108.47 ppm/°C. Also, the corner simulation shows a difference of 0.3 μA from the nominal value of 1 μA.

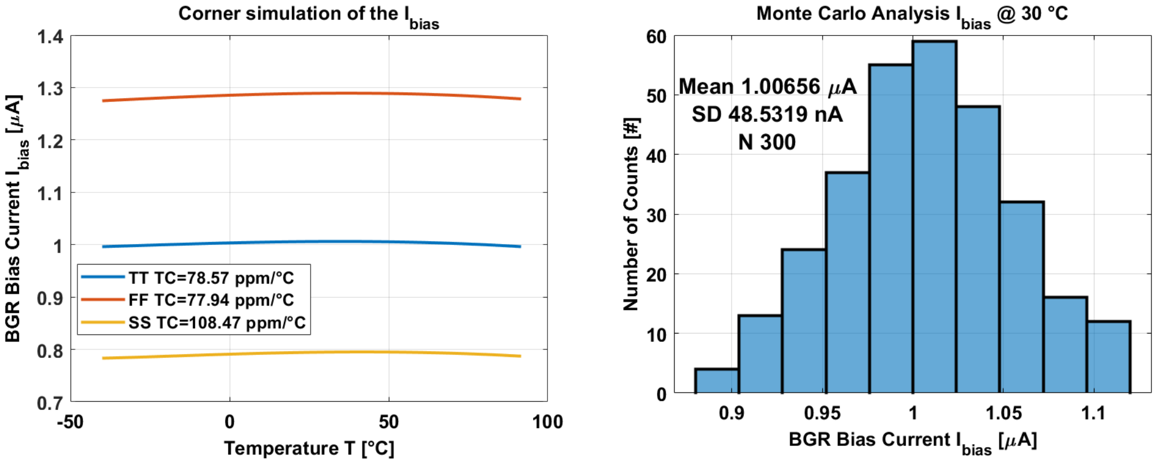

(a) (b)

Figure 5-12: (a) Simulation of the BGR bias current of the temperature sensors. (b) Monte Carlo analysis of the bandgap reference bias current.

Figure 5-12 (b) shows a Monte Carlo analysis of the BGR bias current. The analysis was done by running 300 simulations where the process and mismatch of all components of the BGR were analysed. Results show that the bias current varies by 5% around the mean value at 30 °C (worst case).

Three bias voltages of the PGA ($VP1$, $VN1$, and $IBIASN$; Figure 4-17) were generated by using the BGR as well as the reference voltage of the PGA (V_{REF}; Figure 4-16). Two different reference voltages were generated: 0.7 V and 1.1 V. Figure 5-13 shows one of the bias voltages (a) and its Monte Carlo simulation (b).

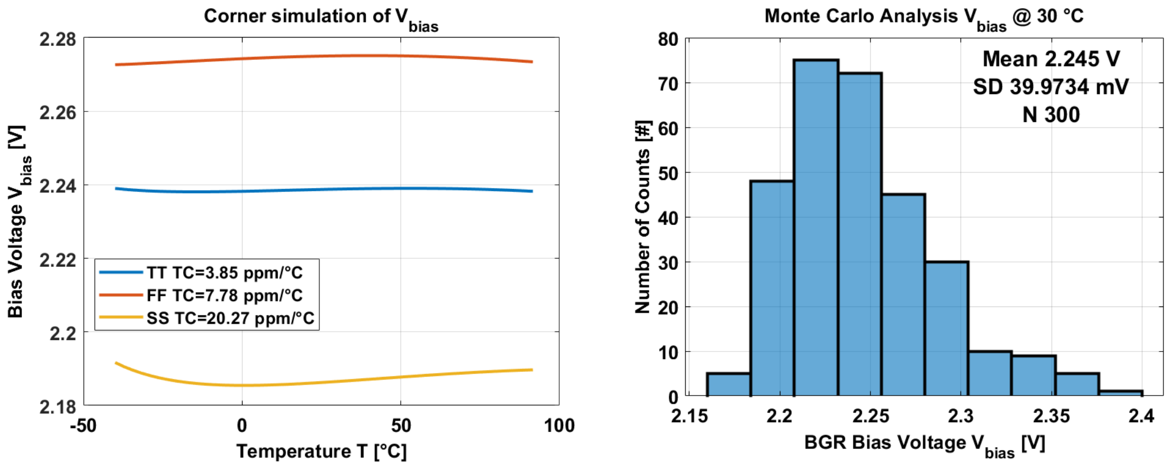

(a) (b)

Figure 5-13: (a) Post-layout simulation of the 2.2 V bias voltage of the PGA. (b) Monte Carlo simulation of the 2.2 V bias voltage of the PGA.

The different values of the bias voltages and the reference voltages of the PGA are shown in Table 5-1.

Table 5-1: Temperature coefficient and power consumption of the different bias voltages and the reference voltages used in the PGA.

Voltage [V]	TC [ppm/°C] TT	TC [ppm/°C] FF	TC [ppm/°C] SS	Power Consumption @ 25 °C [µW]
2.2 (V_{Bias})	3.42	7.76	11.81	56
1.1 (V_{Bias})	4.71	8.55	11.59	54
0.9 (V_{Bias})	4.81	8.91	11.43	52
1.1 (V_{REF})	5.17	9.24	12.52	54
0.7 (V_{REF})	5.25	9.90	12.96	54

A comparison between using the bias of the PGA in Chapter 4 (based on Gm-cell) and the bias based on the BGR is shown in Figure 5-14.

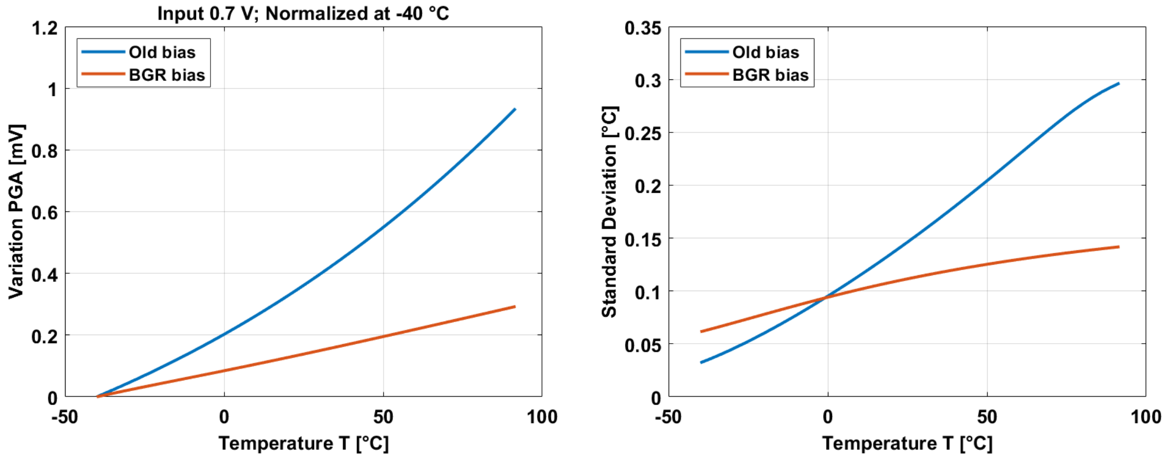

(a) (b)

Figure 5-14: (a) Temperature variation in the PGA when used in a source follower configuration. (b) Standard deviation of the PGA .

When the PGA (Section 4.3.2) is used in a source follower configuration and a constant input voltage of 0.7 V is applied, the voltage variation (after normalized at -40 °C) reaches up to 1 mV by using the old biasing of Chapter 4 compared to a variation of 0.3 mV by using the biasing based on a BGR, as shown in Figure 5-14 (a). If the TC of the temperature sensors is in the order of ~1 mV/°C, this means a variation of 1 °C for the old bias and 0.3 °C for the new bias. Figure 5-14 (b) shows the standard deviation of the PGA after a corner simulation. The standard deviation was calculated between corners at each temperature and the value was converted into Celsius degrees by using the TC of 1 mV/°C. The standard deviation is considerably reduced to a maximum of 0.15 °C by using the BGR bias compared to a maximum deviation of 0.3 °C when the old bias is used. In this way, the temperature dependence of the PGA is considerably reduced by using a BGR bias.

5.4.4 Simulation of the Temperature Sensors

Monte Carlo simulations (100 runs) of the Tixel and nSFTS were performed in order to determine the temperature coefficient, non-linearity and inaccuracy (3σ) over a temperature range between -40 °C and 90 °C.

5.4.4.1 Simulation of the Tixel

The average temperature coefficient of the Tixel corresponds to 1.26 mV/°C, as shown in Figure 5-15 (a).

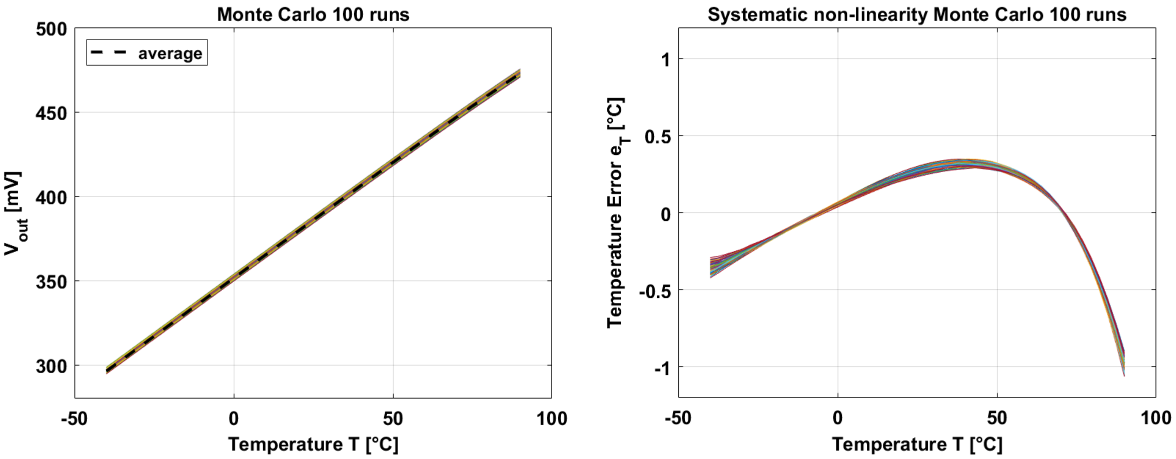

(a) (b)

Figure 5-15: (a) Temperature coefficient of the Tixel. (b) Systematic non-linearity error of the Tixel after a 1st order curve fitting.

The systematic non-linearity error was calculated after applying a 1st order curve fitting to each curve of the temperature coefficient and then obtaining the difference between the measurement and the fit. The non-linearity has a value of ±1 °C (Figure 5-15 (b)). The inaccuracy (3σ) of the Tixel was calculated after removing the systematic non-linearity from the TC curves and applying a 2nd order polynomial [19]. The inaccuracy reached by the Tixel is ±0.35 °C, as shown in Figure 5-16.

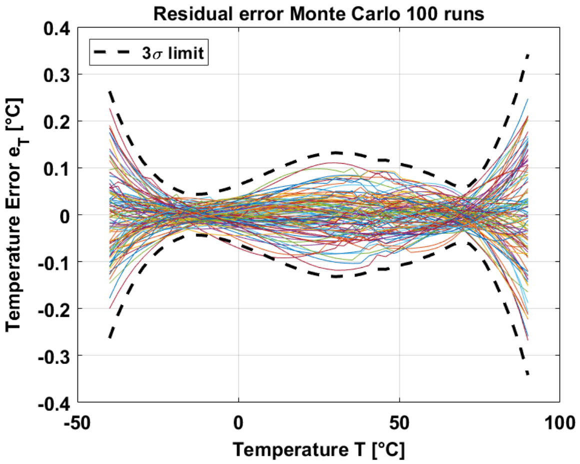

Figure 5-16: Inaccuracy of the Tixel after systematic non-linearity removal and a 2nd order curve fitting.

5.4.4.2 Simulation of the nSFTS

In the case of the nSFTS, the temperature coefficient corresponds to 1 mV/°C, as shown in Figure 5-17 (a).

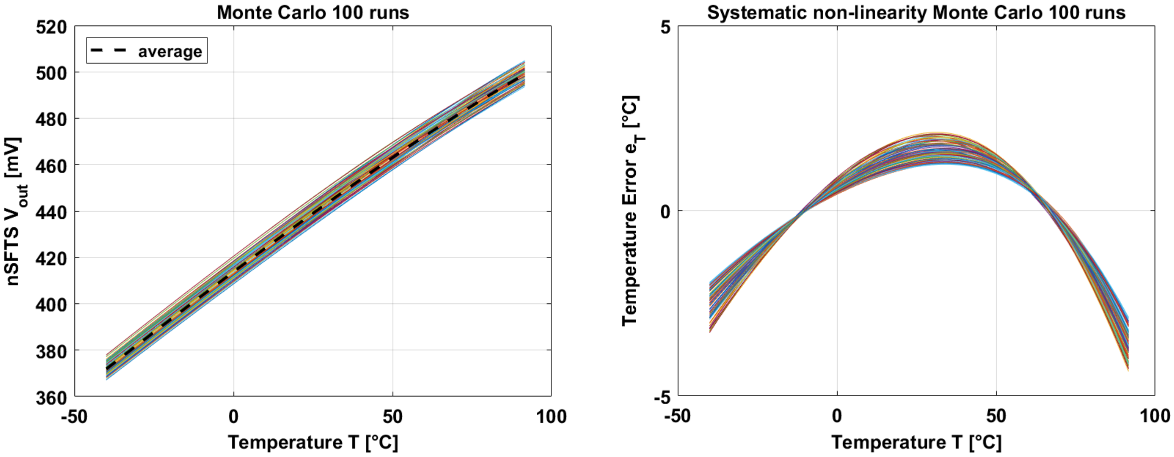

(a) (b)

Figure 5-17: (a) Temperature coefficient of the nSFTS. (b) Systematic non-linearity error of the nSFTS after a 1st order curve fitting.

The systematic non-linearity error was calculated after a 1st order curve fitting and it corresponds to ±4 °C (Figure 5-17 (b)). After compensating for the systematic error and applying a 2nd order polynomial [19], the inaccuracy (3σ) of the nSFTS has a value of ±0.5 °C, as shown in Figure 5-18.

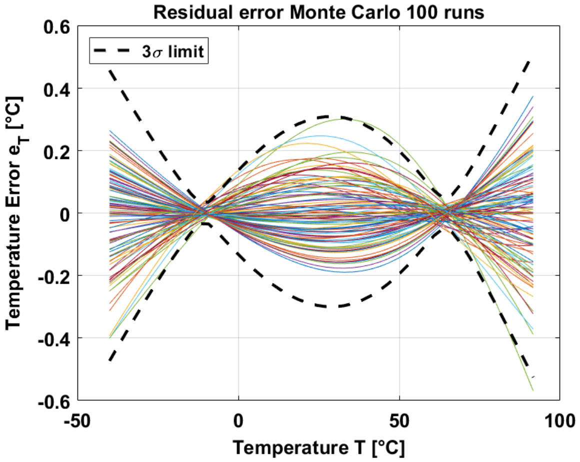

Figure 5-18: Inaccuracy of the nSFTS after systematic non-linearity removal and a 2nd order polynomial.

5.5 Measurement Results and Discussion

The measurement setup was composed of a PCB that provided the main power supplies of the chip, an FPGA generating all control signals, a temperature-controlled oven model VT7004, a reference calibrated temperature sensor Pt-100, and a PC with LabView and Matlab for processing. To reduce the drift of the oven, the PCBs were placed in a massive aluminium box, with all other components inside the oven. The temperature of the oven was controlled by a feedback loop with the Pt-100 as the temperature controller.

The measurements were done over a temperature range between −40 °C and 90 °C in steps of 10 °C. For both types of temperature sensors, 100 frames were taken and averaged to obtain the temperature coefficient and the inaccuracy.

The sensor was fabricated in a standard CIS 0.18 µm TowerJazz technology.

5.5.1 Tixel Measurement Results

The image sensor has 20 Tixels integrated in the array. The results of the temperature coefficient and the systematic non-linearity error are shown in Figure 5-19. The average temperature coefficient of the Tixel corresponds to 1.08 mV/°C and the curvature is in the order of 0.04%. After applying a 1st order curve fitting, the systematic non-linearity error is calculated and it is ±1.5 °C.

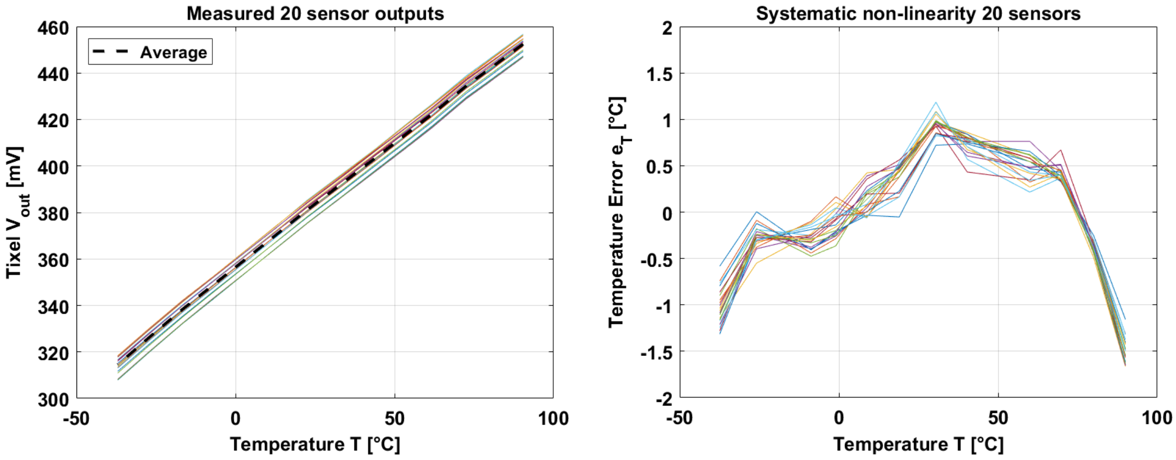

(a) (b)

Figure 5-19: (a) Temperature behavior of the 20 Tixels using a gain of 16. (b) Systematic non-linearity error after a 1st order curve fitting.

An inaccuracy of ±0.5 °C was reached by the Tixels after systematic non-linearity compensation and a 2nd order curve fitting, as shown in Figure 5-20. Results are aligned with simulations.

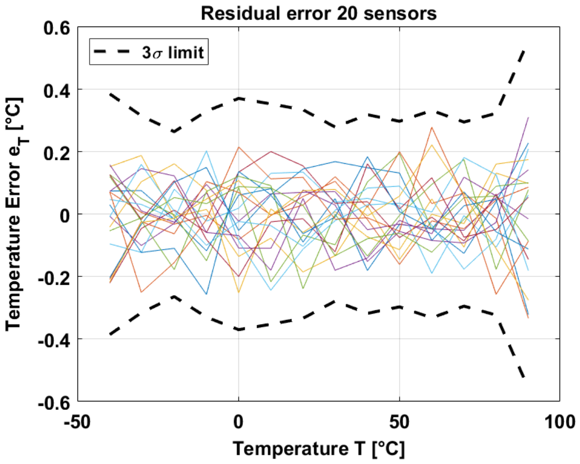

Figure 5-20: Inaccuracy of the Tixels after systematic non-linearity removal and a 2nd order polynomial.

5.5.2 nSFTS Measurement Results

The average output voltage exhibits a curvature in the order of 0.15% and an average temperature coefficient of 1.07 mV/°C in the temperature range of −40 °C to 90 °C, as shown in Figure 5-21. The systematic non-linearity error of the nSFTS corresponds to ±4 °C, after a 1st order curve fitting.

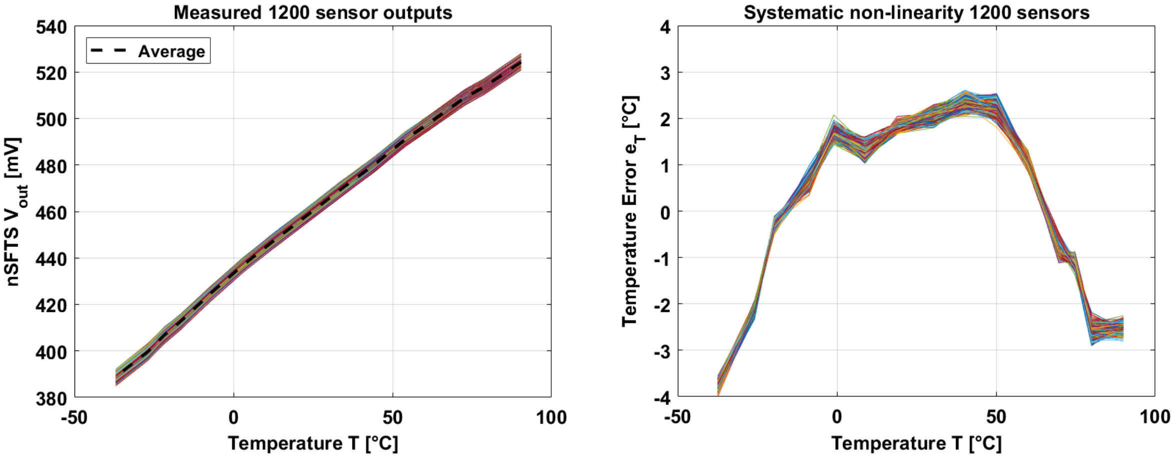

(a) (b)

Figure 5-21: (a) Temperature behavior of the 1200 nSFTS using a gain of 16. (b) Systematic non-linearity error after a 1st order curve fitting.

The inaccuracy (3σ) was calculated after systematic non-linearity removal and applying 2nd order polynomial and it is ±0.55 °C.

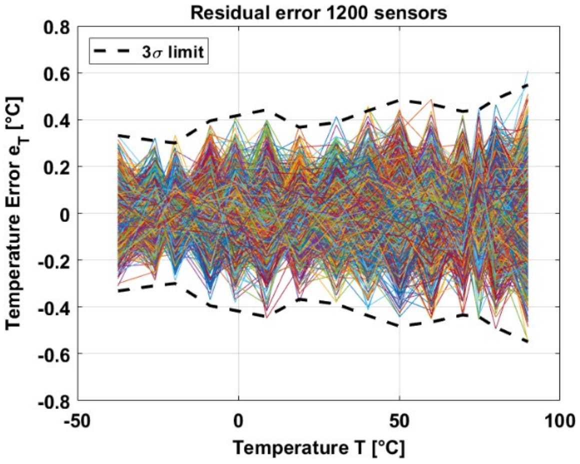

Figure 5-22: Inaccuracy of the nSFTSs after systematic non-linearity removal and a 2nd order polynomial.

The results of the temperature sensors have been compared with our previous work in Table 5-2.

Table 5-2: Comparison with previous work.

Item	[27]	[22]	[19]	This Work	This Work
Year	2018	2020	2018	2020	2020
Type	BJT	nMOS	BJT	BJT	nMOS
Resolution (°C)	0.1	0.13	0.09	0.1	0.1
3σ Inaccuracy (°C)	±0.3	±1.2	±1.1	±0.5	±0.55
Range (°C)	20 to 90	−20 to 80	−20 to 80	−40 to 90	−40 to 90
Area (μm^2)	242	121	121	121	121
Technology (μm)	0.18 CIS	0.18 CIS	0.18 CIS	0.18 CIS	0.18 CIS
Power (μW)	15	36	36	15	20

5.5.3 Dark Current Measurements

The average dark signal has been measured as a function of the exposure time. As half of the pixel array only contains pixels and the other half contains pixels + Tixels, the dark signal and dark current have been calculated for each part of the pixel array. The part of the array with only pixels exhibits a lower dark signal than the part with the Tixels, as shown in Figure 5-23 (a). The dark current at 30 °C without Tixels is 33.5 e^-/s, while the dark current with Tixels corresponds to 63.8 e^-/s. The influence of the Tixels almost doubles the normal dark current of the pixel array.

The influence of the Tixels is also observed when the dark current is plotted over temperature, as shown in Figure 5-23 (b). The temperature behavior of the dark current exhibits two different curves depending on the temperature range. It is well known that, for low temperatures the depletion dark current dominates, while at high temperatures the diffusion dark current takes over [27], [28].

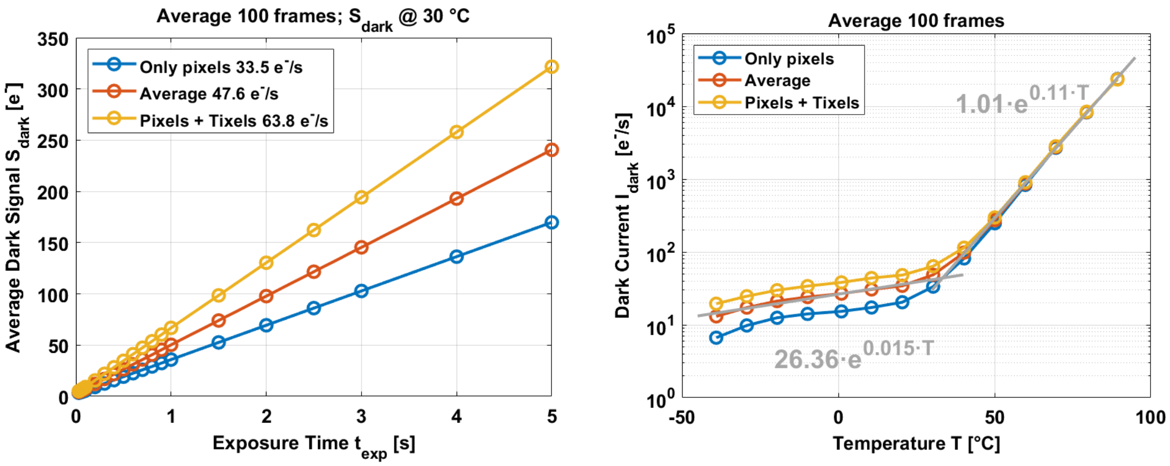

(a) (b)

Figure 5-23: (a) Variation in the dark signal with exposure time. (b) Variation in the dark current with temperature.

The influence of the Tixels is not only seen as an offset added to the dark current but also the slope of the dark current changes over temperature, especially at low temperatures. In the case of the pixel array without Tixels, the dark current increases 1.1 times every 5 °C for low temperatures and 1.8 times every 5 °C for high temperatures. In the case of the pixel array with Tixels, the dark current increases 1.05 times every 5 °C for low temperatures and 1.8 times every 5 °C for high temperatures. At temperatures higher than 25 °C, both parts of the array show the typical behavior where the diffusion dark current dominates. However, at temperatures below 20 °C, the temperature behavior is different depending on the part of the array (with or without Tixels). In the case of the array with Tixels, it seems the depletion dark current is not the dominant mechanism involved because the increment is only 1.05 times per 5 °C instead of ~1.5 times every 5 °C. This behavior was observed in Chapter 4 and it is attributed to a possible electroluminescence (EL) effect generated by the bipolars and tunnelling current. Thus, the measured dark current at low temperatures might be the result of adding the depletion dark current, EL, and tunnelling. In the case of the array without Tixels, the increment is 1.1 times per 5 °C. It might be that EL and tunnelling still affect the pixels (in a lower way) although they are far from the Tixels. In Chapter 6, a deeper analysis of the perturbation produced by the bipolars on the pixels close to the BJTs is presented.

As the output voltage (V_{out}) of the temperature sensors is a measure of the temperature, this can be used to predict the (average) dark current, especially at high temperatures. By ignoring the 2nd order term of the temperature sensors, the relation between the average dark current (at high temperatures) and the temperature sensors is obtained, as shown in Equation (5-17):

$$\begin{aligned} I_{dark\_Tixel} &= 1.01 \cdot e^{0.11\left(\frac{V_{out\_Tixel}-350.2}{1.08}\right)} \\ I_{dark\_nMOS} &= 1.01 \cdot e^{0.11\left(\frac{V_{out\_nMOS}-435.1}{1.07}\right)} \end{aligned} \tag{5-17}$$

5.6 Conclusion

The use of the pixel as a temperature sensor have been presented. The pixel can be used either for imaging or for temperature sensing. When the pixel is used as a temperature sensor, the pinned photodiode is switched off and the temperature is obtained by the differential gate-source voltage of the source-follower in-pixel transistor. Also, BJT-based temperature sensors been integrated in order to compare with the nSFTS. The size of the Tixel has been reduced to one pixel area compare to the previous chapter where the Tixel occupied two pixels area. Good inaccuracy of in-pixel temperature sensors have been achieved by using a bandgap reference circuit with temperature-compensated resistors. The BGR circuit can provide temperature-compensated current and temperature-compensated bias/reference voltage by using the same circuit. The temperature coefficient of the bias current is 78.57 ppm/°C in the TT corner (108.47 ppm/°C in the SS corner, worst case) while the temperature coefficient of the bias/reference voltage is in the order of 5 ppm/°C in the TT corner (~12 ppm/°C in the SS corner, worst case). The PGA is fully biased by using the BGR circuit, thus resulting in a reduction in the thermal dependence of the PGA from 0.3 °C to 0.15 °C. Also, through the use of DEM to cancel the mismatch of the current mirrors, a CDS circuit to cancel the offset of the PGA, and the technique of selecting multiple pixels, similar relative inaccuracy was achieved [27], [22]. The pixels and the temperature sensors have been characterized in a temperature range between −40 °C and 90 °C. The dark current shows two different types of exponential behavior with temperature. In the temperature range of −40 °C to 30 °C, the average dark signal increases only 1.08

times every 5 °C, which might be the result of a combination of depletion dark current and electroluminescence due to the presence of the Tixels. In the temperature range of 30 °C to 90 °C, the dark signal exhibits typical diffusion dark current-dominated behavior increasing 1.8 times every 5 °C. Tixels show an average temperature coefficient of 1.08 mV/°C and an inaccuracy (3σ) of ±0.5 °C, over the whole temperature range. In the case of the nSFTS, they show an average temperature coefficient of 1.07 mV/°C and an inaccuracy (3σ) of ±0.55 °C.

References

[1] S. Ay, M. Lesser, and E. Fossum, "CMOS Active Pixel Sensor (APS) imager for scientific applications," in *Astronomical Telescopes and Instrumentation*, 2002, vol. 4836, pp. 271-278.

[2] M. Schanz, C. Nitta, A. Bussmann, B. J. Hosticka, and R. K. Wertheimer, "A high-dynamic-range CMOS image sensor for automotive applications," *IEEE Journal of Solid-State Circuits,* vol. 35, no. 7, pp. 932-938, 2000.

[3] A. E. Gamal and H. Eltoukhy, "CMOS image sensors," *IEEE Circuits and Devices Magazine,* vol. 21, no. 3, pp. 6-20, 2005.

[4] E. Fossum, "Active pixel sensors: are CCDs dinosaurs?," in *Symposium on Electronic Imaging: Science and Technology*, 1993, vol. 1900, pp. 2-14.

[5] E. R. Fossum, "CMOS image sensors: electronic camera-on-a-chip," *IEEE Transactions on Electron Devices,* vol. 44, no. 10, pp. 1689-1698, 1997.

[6] B. Ackland and A. Dickinson, "Camera on a chip," in *1996 IEEE International Solid-State Circuits Conference. Digest of Technical Papers, ISSCC*, 1996, pp. 22-25.

[7] W. Shou-Gwo *et al.*, "A high performance active pixel sensor with 0.18um CMOS color imager technology," in *International Electron Devices Meeting. Technical Digest*, 2001, pp. 555-558.

[8] M. K. Law, A. Bermak, and H. C. Luong, "A Sub-μW Embedded CMOS Temperature Sensor for RFID Food Monitoring Application," *IEEE Journal of Solid-State Circuits,* vol. 45, no. 6, pp. 1246-1255, 2010.

[9] L. Yu-Shiang, D. Sylvester, and D. Blaauw, "An ultra low power 1V, 220nW temperature sensor for passive wireless applications," in *2008 IEEE Custom Integrated Circuits Conference*, 2008, pp. 507-510.

[10] A. Vaz *et al.*, "Full Passive UHF Tag With a Temperature Sensor Suitable for Human Body Temperature Monitoring," *IEEE Transactions on Circuits and Systems II: Express Briefs,* vol. 57, no. 2, pp. 95-99, 2010.

[11] K. Hyuck In, K. In Man, P. Byung-Gook, L. Jong Duk, and P. Sang Sik, "The analysis of dark signals in the CMOS APS imagers from the characterization of test structures," *IEEE Transactions on Electron Devices,* vol. 51, no. 2, pp. 178-184, 2004.

[12] X. Wang, "Noise in sub-micron CMOS image sensors," Ph.D. Dissertation, Delft University of Technology, pp. 46-68, 2008.

[13] P. S. Baranov, V. T. Litvin, D. A. Belous, and A. A. Mantsvetov, "Dark current of the solid-state imagers at high temperature," in *IEEE Conference of Russian Young Researchers in Electrical and Electronic Engineering (EIConRus)*, 2017, pp. 635-638.

[14] R. Widenhorn, M. Blouke, A. Weber, A. Rest, and E. Bodegom, "Temperature dependence of dark current in a CCD," in *Electronic Imaging*, 2002, vol. 4669, pp. 193-201.

[15] S. Han and E. Yoon, "Low dark current CMOS image sensor pixel with photodiode structure enclosed by P-well," *Electronics Letters,* vol. 42, no. 20, pp. 1145-1146, 2006.

[16] M. A. P. Pertijs, K. A. A. Makinwa, and J. H. Huijsing, "A CMOS smart temperature sensor with a 3σ inaccuracy of ±0.1 °C from -55 °C to 125 °C," *IEEE Journal of Solid-State Circuits,* vol. 40, no. 12, pp. 2805-2815, 2005.

[17] R. Coath, J. Crooks, A. Godbeer, M. Wilson, and R. Turchetta, "Advanced pixel architectures for scientific image sensor," in *Proceedings of the Topical Workshop on Electronics for Particle Physics*, 2009, pp. 57-61.

[18] E. R. Fossum and D. B. Hondongwa, "A Review of the Pinned Photodiode for CCD and CMOS Image Sensors," *IEEE Journal of the Electron Devices Society,* vol. 2, pp. 33-43, 2014.

[19] S. Xie and A. Theuwissen, "Compensation for Process and Temperature Dependency in a CMOS Image Sensor," *Sensors,* vol. 19, no. 4, p. 870, 2019.

[20] D. A. Neamen, *Semiconductor physics and devices: basic principles*, 3rd ed. McGraw-Hill, 2012, pp. 268-318.

[21] M. A. P. Pertijs and J. H. Huijsing, *Precision temperature sensors in CMOS technology*. Springer, 2006, pp. 11-46.

[22] S. Xie, A. A. Prouza, and A. Theuwissen, "A CMOS-Imager-Pixel-Based Temperature Sensor for Dark Current Compensation," *IEEE Transactions on Circuits and Systems II: Express Briefs,* vol. 67, no. 2, pp. 255-259, 2020.

[23] S. Xie and A. J. P. Theuwissen, "Suppression of Spatial and Temporal Noise in a CMOS Image Sensor," *IEEE Sensors Journal,* vol. 20, no. 1, pp. 162-170, 2020.

[24] P. Malcovati, F. Maloberti, C. Fiocchi, and M. Pruzzi, "Curvature-compensated BiCMOS bandgap with 1-V supply voltage," *IEEE Journal of Solid-State Circuits,* vol. 36, no. 7, pp. 1076-1081, 2001.

[25] X. Guan, X. Wang, A. Wang, and B. Zhao, "A 3 V 110 µW 3.1 ppm/°C curvature-compensated CMOS bandgap reference," *Analog Integrated Circuits and Signal Processing,* vol. 62, no. 2, pp. 113-119, 2010.

[26] Y. P. Tsividis, "Accurate analysis of temperature effects in IC-VBE characteristics with application to bandgap reference sources," *IEEE Journal of Solid-State Circuits,* vol. 15, no. 6, pp. 1076-1084, 1980.

[27] A. Abarca, S. Xie, J. Markenhof, and A. Theuwissen, "Integration of 555 temperature sensors into a 64 × 192 CMOS image sensor," *Sensors and Actuators A: Physical,* vol. 282, pp. 243-250, 2018.

[28] K. Yasutomi, Y. Sadanaga, T. Takasawa, S. Itoh, and S. Kawahito, "Dark current characterization of CMOS global shutter pixels using pinned storage diodes," in *Proc. Int. Image Sensor Workshop—IISW*, 2011, pp. 8-11.

6 HOT PIXELS IN THE PIXEL ARRAY CAUSED BY THE BJT-BASED TEMPERATURE SENSORS

An unusually high output signal in some pixels has been observed during dark current measurements. This high dark signal in some pixels is believed to be associated with the presence of BJT-based temperature sensors. Pixels placed next to the BJTs exhibit a very high dark signal level, while pixels not positioned next to the BJTs exhibit a normal dark signal level. This effect has been reported in the literature and it is attributed to the presence of an electroluminescence (EL) effect caused by recombination and/or hot carriers. A portion of the electrons and photons generated by the EL effect are absorbed by the photodiode while the rest recombine in the substrate. In Section 6.1 of this chapter an introduction of the effect of integrating bipolars in the pixel array is presented. In Section 6.2 the theory of the electroluminescence effect and how it is generated is given. A block diagram and architecture of the pixel array with the bipolars is given in Section 6.3. An analysis of the dark signal measurements of the pixel array is presented in Section 6.4. Finally, a conclusion of this chapter is given in Section 6.5.

6.1 Introduction

Measurements of the dark current of the test CIS device of Chapter 4 and Chapter 5 show an unusually high dark signal that occurs in some pixels across the pixel array. These “hot pixels” form a pattern along the array surrounding the position of BJT-based temperature sensors. As the hot pixels are next to the BJTs, the first assumption could be that the BJTs are causing the high dark signal in those pixels. This effect is seen either when the dark signal is measured over time (exposure time) or over temperature. Figure 6-1 shows how this pattern is repeated in the pixel array at two different temperatures (0 °C and 40 °C).

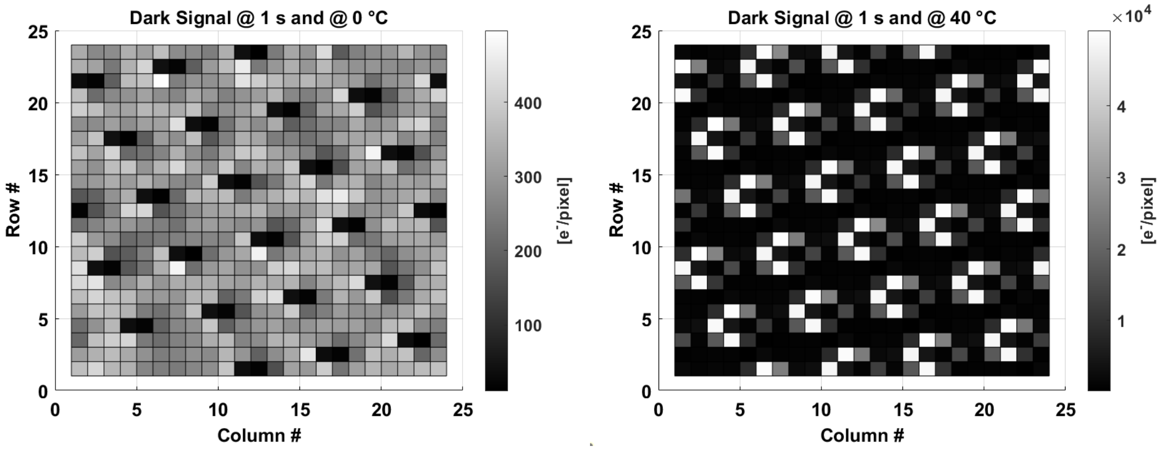

(a) (b)

Figure 6-1: (a) Dark signal of the pixel array at 1 s and at 0 °C. The black dots correspond to the BJTs. (b) Dark signal of the pixel array at 1 s and at 40 °C. At both temperatures it is possible to see the presence of the hot pixels next to the BJTs.

A similar effect has been observed in [1] and in [2]. In [1] the backside illumination SOI-based image sensor exhibits clusters of hot pixels across the pixel array. These hot pixels correspond to the EL effect produced by the n+/p-well junctions in the in-pixel transistors.

The EL effect, observed using emission microscopy (EMMI) system in the near-infrared spectrum, shows a correlation between the EL captured by the EMMI system and the positions of the hot cluster in the pixel array. In this case, the emitting p-n junctions are related to the in-pixel source follower and to the reset transistor. It has been observed that increasing the supply voltage of both transistors also increases the signal read by the EMMI system. The junctions of the source follower transistor and the reset transistor emit photons (EL effect), some photons of which are absorbed by the surrounding photodiodes. The EL effect can be attributed to the interband radiative recombination process or to hot carriers. Since the photon energy captured by the EMMI system is higher than the bandgap of Si, the research concludes that the hot carriers are responsible of the hot pixels.

On the other hand, in [2] a non-uniform image in dark has been observed. Some areas of the pixel array show a higher dark signal compared to the rest of the pixel array. According to [2], this phenomenon depends on the integration time but it is independent of temperature. It has been found that next to the high dark signal areas, two bipolar-based bandgap references (BGRs) appear. These two BGRs are at different distances from the pixel array; where the areas closer to the BGR exhibit a higher dark signal compared to those further from the other BGR. This leads to the hypothesis that the BGR circuits generate photons which cause these high dark signal spots. To confirm the photon emission, two experiments have been done. In the first one, the distance between the collector and the emitter of a lateral NPN bipolar was changed while keeping the emitter bias current constant. Results show that increasing the distance indicates a reduction in the collector current. Also, for distances between 300 µm and 800 µm, the collector current can be characterized by the standard BJT relationship. However, for distances greater than 800 µm, the collector current could not ideally follow the BJT equation ideal. The non-ideality in collector current was attributed to photon generation in the forward biased PN junction. The second experiment, involved changing the forward bias current of the p-n junction diodes. Results show that the bias current is proportional to the dark signal of the hot spots. A conclusion that can be drawn is that, this non-ideality is a consequence of photon generation in the forward biased p-n junction, where some photons are absorbed by the pixels.

6.2 Electroluminescence by Radiative Recombination

In this section some important concepts will be presented. These concepts help to define the phenomenon behind the hot pixels produced in the presence of BJTs.

6.2.1 Electroluminescence

Light emission from a p-n junction is a well-known phenomenon that was reported for the first time by Newman in 1955 [3]. Electroluminescence is one of the few phenomena in which a direct conversion of electric energy into non-thermal emitted light takes place. The phenomenon behind EL is related to radiative recombination. The EL effect can occur either in a forward biased p-n junctions or in a reverse biased p-n junctions [4], [5].

6.2.2 Radiative Recombination

Recombination is the process in which an electron of the conduction band re-occupies an energy state of a hole in the valence band. In this band-to-band transition, an electron can emit a photon (EL effect) while the transition takes places. This emitting process is called radiative recombination [6]. Non-radiative recombination also exists but instead of a photon, a phonon is emitted.

In the case of silicon, the radiative efficiency is low because silicon is an indirect bandgap material [7]. An indirect bandgap material refers to a material where the minimum energy state in the conduction band and the maximum energy state in the valence band are not aligned by its crystal momentum [8], [9]. Although Si is an indirect bandgap material, radiative recombination can occur assisted by crystallographic defects in the silicon. In this way, an electron from the conduction band can fall into the valence band passing through the defect in the Si and emitting a photon at mid-bandgap energy levels. This transition is shown in Figure 6-2 (a).

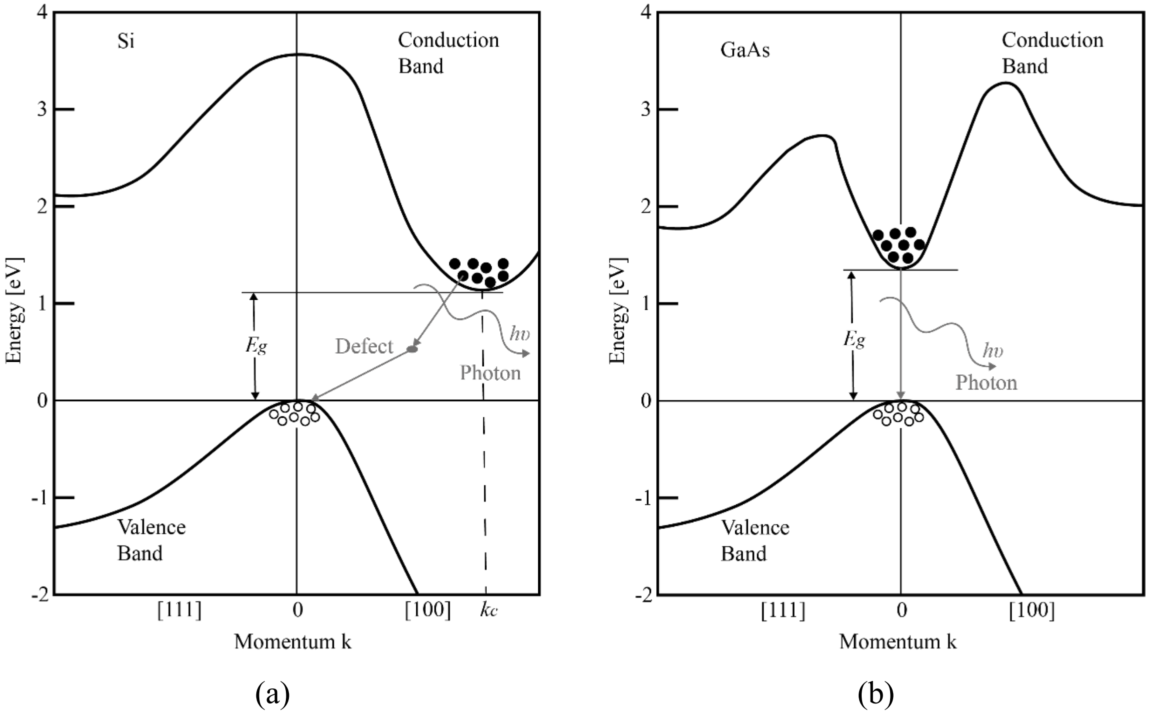

Figure 6-2: (a) Indirect bandgap transition in Si. The minimum and maximum energy states are not aligned. Radiative recombination through a midgap defect in Si emitting a photon. (b) Direct bandgap transition in GaAs. The minimum and maximum energy states are aligned. Radiative recombination without the need for a midgap defect in GaAs [9], [10].

In the case of an indirect bandgap transition, in order for the electron to recombine with a hole in the valence band, the energy of the electron must not only be above that of the bandgap energy of the material (E_g) but also change in momentum. On the other hand, in a direct bandgap transition, the energy of the electron is at least equal to E_g and there is no change in momentum for it to recombine with a hole in the valence band, as shown in Figure 6-2 (b). In both transitions, the electron loses energy which is emitted as a photon.

Apart from the indirect and direct bandgap transitions (also called interband transitions), intraband transitions can also occur. Intraband transitions refer to a transition in the same energy band (either in the conduction band or in the valence band). As the intraband transition occurs in the same band, it involves only either electrons (conduction band, Figure 6-3 (a)) or holes (valence band, Figure 6-3 (b)).

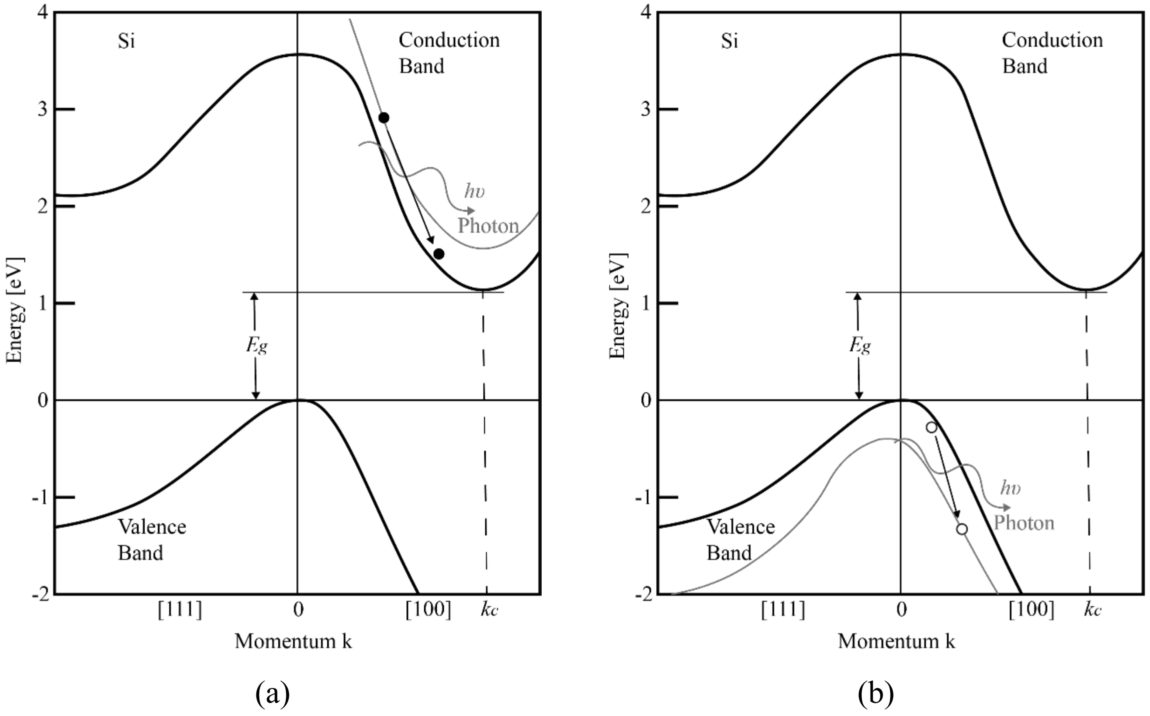

Figure 6-3: (a) Intraband transition in the conduction band. (b) Intraband transition in the valence band [9], [10].

The intraband transitions can be direct or indirect. In the case of an indirect intraband transition, it is assisted by a phonon or a defect in the material.

6.2.3 Carriers Injection due to Forward Biased p-n Junction

When a p-n junction is forward biased, a large population of electrons and holes are placed in close physical proximity. As electrons and holes are close each other, they emit photons while they recombine, as shown in Figure 6-4. The generated light has a spectrum centered around the bandgap of Si. This is a low voltage emission mechanism, thus, the emission spectrum is significantly narrow compared to the reverse biased p-n junction mechanism [11]. The emission spectrum of a forward and a reverse biased Si p-n junction are shown in Figure 6-5.

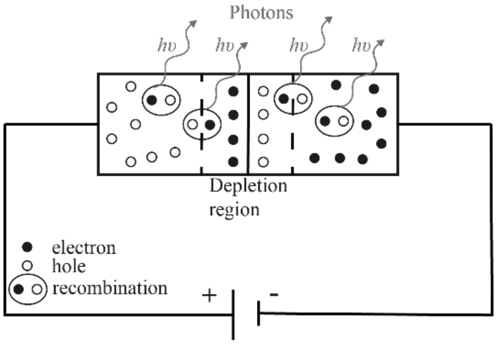

Figure 6-4: EL effect due to recombination in a forward biased p-n junction [11].

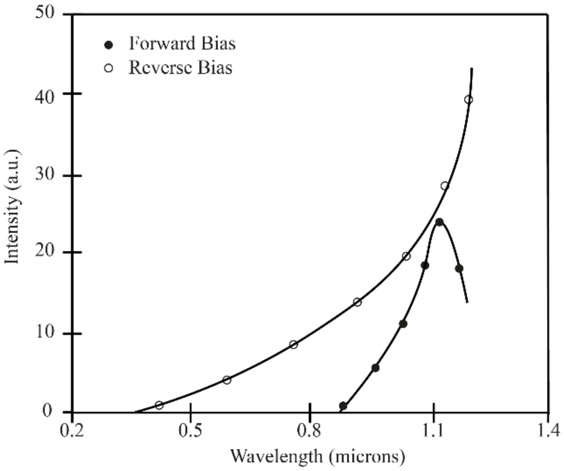

Figure 6-5: Emission spectra from forward and reverse biased Si p-n junction [11].

6.2.4 Hot Carrier Generation due to Reverse Biased p-n Junction

Apart from the forward biased p-n junction, hot carrier generation due to reverse biased p-n junction is also responsible for the EL effect. Hot carrier generation refers to electrons with enough energy to collide with atoms in the silicon creating electron-hole pairs. This effect is mainly caused under reverse biased condition where a strong electric field is generated [11]. This collision, also called impact ionization, can involve an avalanche effect when the electron-hole pair created acquires enough energy to create a new electron-hole pair. This avalanche effect can induce holes to participate in the substrate current and electrons to become minority carriers in the substrate. Impact ionization can arise when the system is not at the thermodynamic equilibrium [10].

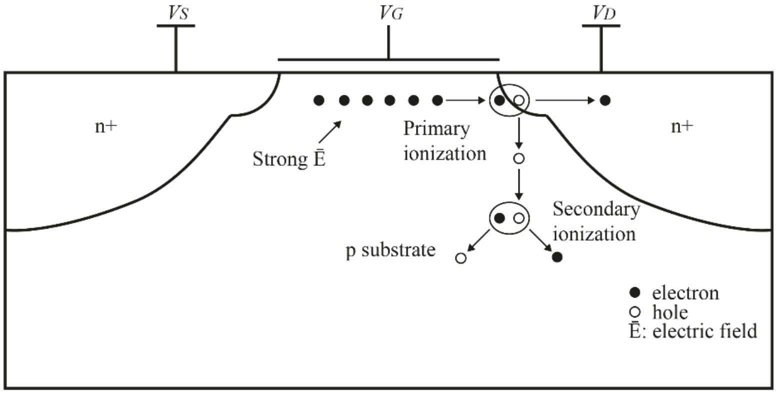

Figure 6-6: Impact ionization generated by hot carriers [10].

Figure 6-6 shows the avalanche effect in an nMOS transistor produced by impact ionization. An electric field accelerates the electrons in the channel leading to the collision with the atoms in the Si. The electric field is controlled by voltages V_{DS} and V_G. This is a high voltage emission mechanism, thus, the emission spectrum is considerably wider than in the case of forward biased, as shown in Figure 6-5.

6.3 Pixel Array with Bipolar-Based Temperature Sensors

The pixels located next to the substrate bipolar temperature sensors exhibit a higher dark current compared to those pixels far from the bipolars. The pixels and bipolars share the same p-substrate, as shown in Figure 6-7.

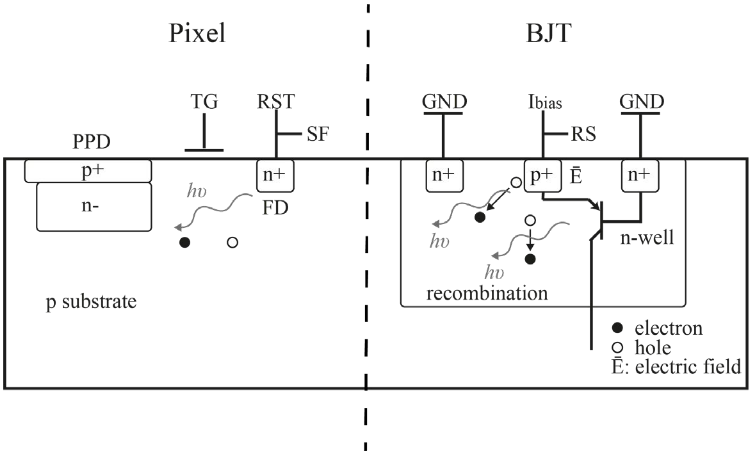

Figure 6-7: A 4T pixel and a BJT sharing the same substrate. Hole injection from the p-n junction and photon generation from recombination. Some photons and/or electrons-holes might reach the pinned photodiode.

This high dark signal might be associated with the holes injection or the hot carrier generation in the p-n junction of the bipolars when the bipolars are biased [2]. Hot carrier generation implies secondary minority carrier generation in the p-substrate. These minority carriers can flow through the substrate, reach the photosensitive area, and as a consequence affect the output dark signal of the photodiode. Also, holes recombine with electrons emitting photons (radiative recombination) that can be absorbed by the photodiode, affecting the dark signal as well.

The emitter of the bipolar (integrated in the pixel array) is connected to two different paths. One path corresponds to the bias current (I_{bias1}) through an nMOS switch (M1), while the other corresponds to the readout of the base-emitter voltage of the bipolar (switch M2).

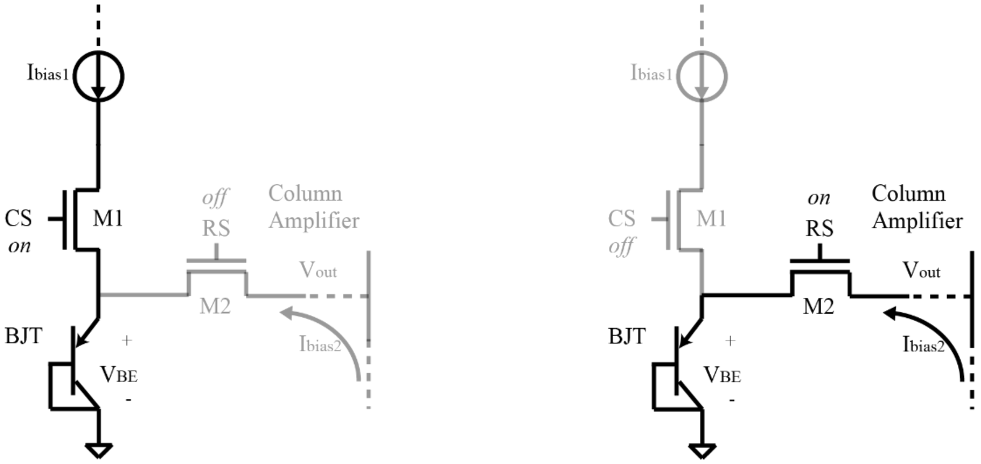

(a) (b)

Figure 6-8: (a) Regular bias path of the BJT when transistor M1 is on. (b) Leakage current coming from the readout path when transistor M2 is on.

The readout is connected to the row select (RS) nMOS transistor (M2) which in turn is connected to the column amplifier. The carriers can be generated either by the presence of the M1 path or by the M2 path. In the next section different measurements will be reported to confirm if there is any correlation between the presence of the bipolars and the high dark signal of the pixels and how it is related to the bias current or the readout path.

6.4 Measurements

The dark signal of the pixel array has been measured by changing different variables such as the exposure time, temperature, and the bias current of the bipolars. The first measurement, shown in Figure 6-9, corresponds to a comparison between the dark signal of the hot pixels and the normal pixels at two different temperatures while keeping the M1 transistor off and I_{bias1} equal to 0 µA (M1 and I_{bias1} in Figure 6-8).

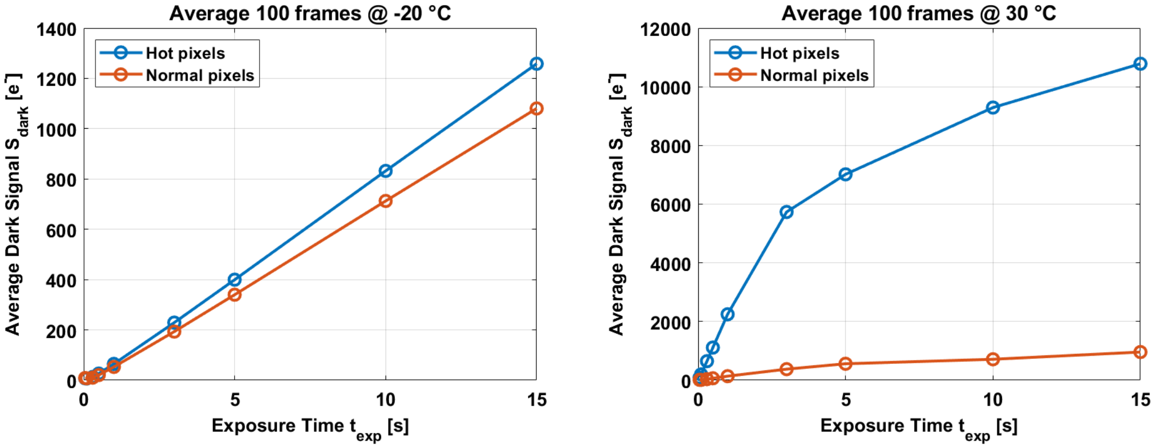

(a) (b)

Figure 6-9: (a) Comparison between the hot pixels and the normal pixels at -20 °C. (b) Comparison between the hot pixels and the normal pixels at 30 °C.

At -20 °C, the dark signal of the hot pixels is comparable to the dark signal of the normal pixels. In this case, the dark current of the hot pixels is 84 e^-/s compared to 72 e^-/s for the normal pixels (Figure 6-9 (a)). However, while this difference in the dark current can be attributed to the normal non-uniformity of the pixels, at 30 °C this difference in the dark current is considerably larger (Figure 6-9 (b)). The hot pixels at 30 °C exhibit a dark current of 1400 e^-/s compared to a dark current of 120 e^-/s for the normal pixels (10 times difference).

To prove that the presence of the bipolars is causing the hot pixels, the dark signal of the hot pixels is compared to the output signal of the temperature sensor pixels (Tixels). Figure 6-10 shows a comparison between the dark signal of the hot pixels (in e^-) and the output signal of the Tixels (in digital number DN).

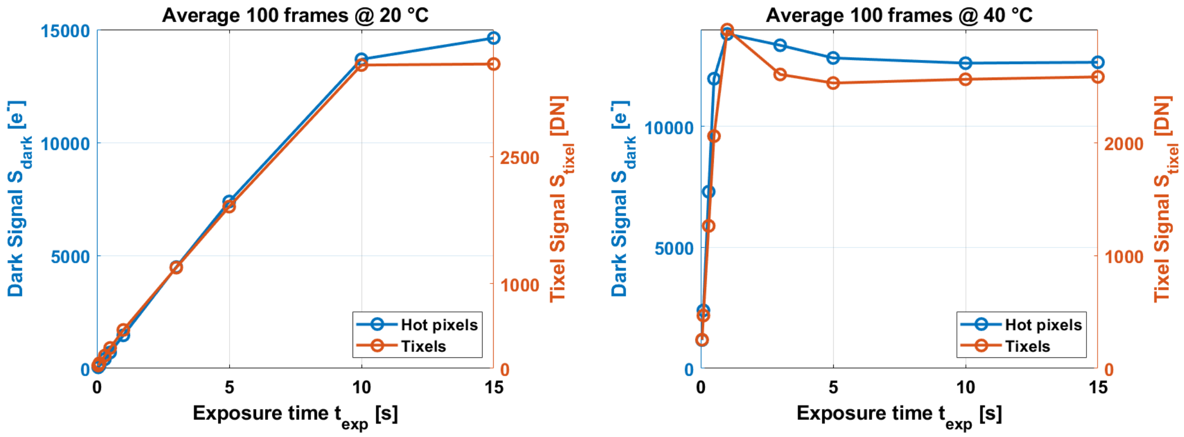

(a) (b)

Figure 6-10: (a) Comparison between the dark signal of the hot pixels and the output signal of the Tixels at 20 °C. (b) Comparison between the dark signal of the hot pixels and the output signal of the Tixels at 40 °C.

Figure 6-10 shows a correlation between the output signals of the hot pixels and the Tixels. At 20 °C, the signal of the Tixels shows a similar curve compared to the dark signal of the hot pixels (Figure 6-10 (a)). At an exposure time of 10 s, both curves begin to saturate following the same trend at longer exposure times. At 40 °C (Figure 6-10 (b)), the saturation begins at an exposure time of 1 s for both curves. In this case, there is stronger evidence of the correlation between the S_{dark} and the S_{tixel}. There is a peak in both signals at 1 s followed by a saturation of the signals at longer exposure time. For pixels located far from the Tixels, no correlation between the dark signal of the normal pixels and the output signal of the Tixels has been observed. The results shown in Figure 6-9 and in Figure 6-10 confirm that the presence of the Tixels affects the dark signal of the (hot) pixels situated next to the temperature sensors.

A measurement to find the cause of the hot pixels has been done by turning on the transistors M1 in only one column of the pixel array and controlling the I_{bias1} of the bipolars in that column. The other bipolars (other columns) remain off (M1 turned off) and I_{bias1} is kept at 0 µA. In one column there are approximately three Tixels. The bias current changes between 0 µA and 1.25 µA. Also, the temperature changes over a small range between 25 °C and 40 °C.

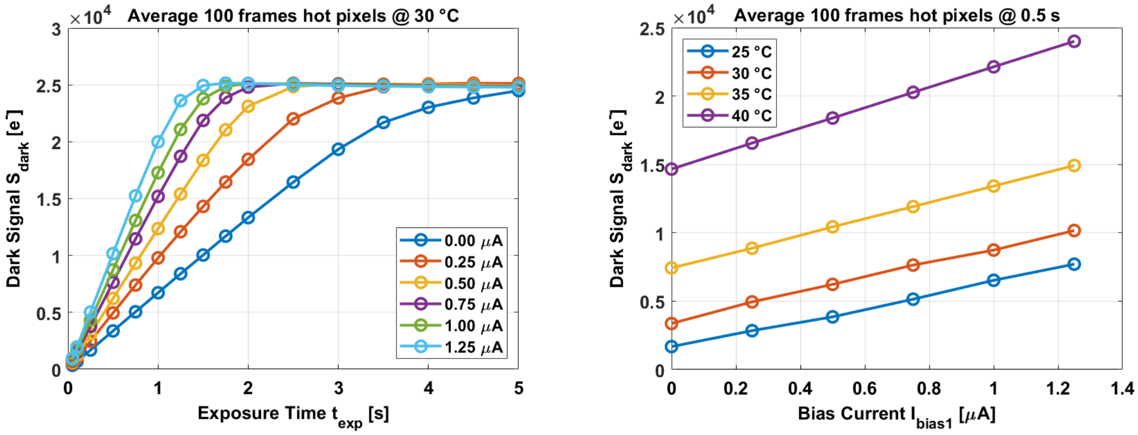

(a) (b)

Figure 6-11: (a) Dark signal vs. exposure time of the hot pixels for different bias currents at 30 °C. (b) Dark signal vs. the bias current of the hot pixels at an exposure time of 0.5 s.

Figure 6-11 (a) shows how the dark signal of the hot pixels changes depending on the bias current of the bipolars at 30 °C. For higher bias currents, the dark signal saturates earlier in time (exposure time). It is worth mentioning that the normal pixels in this column (those not affected by the Tixels) do not change their dark signal as the bias current varies. These results imply that the hot pixels are probably caused by the BJTs due to photon emission when the BJTs are forward biased. Recombination takes place in the base generating photons that can be absorbed by the photodiode. For an exposure time of 0.5 s, Figure 6-11 (b) shows the dark signal variation depending on the bias current at different temperatures. The dark signal at different temperatures exhibits linear behavior with the bias current. There is an offset (I_{bias1} = 0 µA) for every temperature, meaning that there might be leakage current flowing into the bipolars. This leakage current could be caused by the bias current through transistor M1 (Figure 6-8 (a)), even when the I_{bias1} = 0 µA. It is possible that the instrument measuring the I_{bias1} is not able to measure very low levels of I_{bias1}. The minimum current that the instrument is able to detect is 0.01 µA. However, when transistor M1 is turned off, there is still a higher dark signal in the hot pixels (Figure 6-9). Most likely this leakage current is coming from the readout path through transistor M2 (Figure 6-8 (b)). The way to read the data from the pixel array is by selecting one row and reading every column in that row. Then, the next row is selected and all the columns of that row are read and so on. When a row is selected in the pixel array, the M2 transistor is turned on (via RS control signal) allowing to some current flowing (or sinking) into the bipolar. This current might bias/charge the bipolar creating electron-hole pairs in the p-n junction leading to hot carriers and/or photon emission by recombination. The hot carriers produce an avalanche effect via impact ionization, some of the free electrons of which reach the active photodiode adding extra signal to the total dark signal of the pixels. Also, some holes recombine via radiative recombination emitting photons when losing energy (electroluminescence effect) and probably some of these photons are absorbed by the photodiode as well. To detect electroluminescence in the pixel array an infrared camera must be used. During the measurements different infrared cameras in the near infrared (800 nm – 1100nm) were utilized to detect EL in the pixel array in order to confirm if forward biased p-n junction or reverse biased p-n junction is the main cause of the hot pixels when switch M1 is off. The spectra of forward biased is narrower than the spectra of reverse biased, as shown in Figure 6-5. Unfortunately, no EL effect was observed during the measurements, even at the highest bias current of 1.25 μA. The reason might be that, the level of the bias current is still too low to generate powerful enough EL to be detected by the different infrared cameras. In [9] an EL intensity of 4×10^{-11} W/eV has been observed for a bias current of 1 mA. Also, in [12], [13] low intensities of EL have been observed for bias current in the order of milli-amperes. Another reason might that, the exposure time was not long enough in order to observe EL in the array. Exposure times up to 20 seconds were used.

The dark current generated by I_{bias1} (or I_{bias2} when I_{bias1} = 0 μA) has been modeled over temperature. In this case, the dark current of the normal pixels is subtracted from the total dark current of the hot pixels. Figure 6-12 shows the dark current over a temperature range of 25 °C to 40 °C.

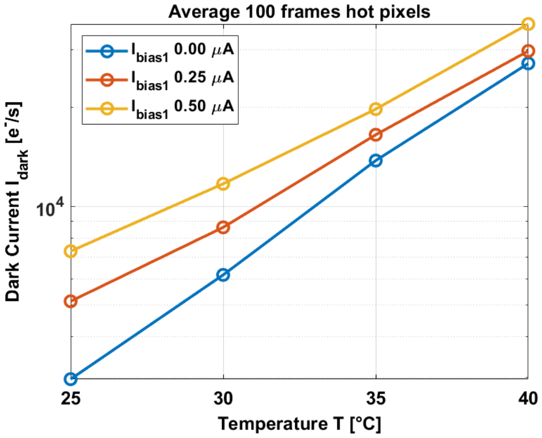

Figure 6-12: Temperature behavior of the dark current, subtracting the normal dark current from the total dark current of the hot pixels.

Figure 6-12 illustrates the typical exponential behavior of the dark current when the temperature is swept between 25 °C and 40 °C. The effect of I_{bias1} on the dark current manifests as an offset at all temperatures controlling the dark current level of the hot pixels.

In Chapters 4 and 5, the atypical temperature behavior of dark current at low temperatures was discussed. Theoretically, at temperatures below ~10 °C the dark current increases close to ~1.5 times every 5 - 10 °C. However, in this design the average dark current only increases ~1.08 times every 5 °C. In Chapter 4, this atypical behavior was suggested to be associated with a tunnelling current in the floating diffusion of the 4T pixel (Section 4.5.1). Also, this behavior was associated with the presence of the bipolars across the array generating photons due to forward biased and/or hot carriers reaching the photodiode (this was already discussed in this chapter). The design of the test chip presented in Chapter 5 [14] gives the possibility of measuring pixels without the presence of the bipolars as half of the array is composed only of 4T pixels.

The dark signal of the pixel array with and without bipolars has been measured in a temperature range between -40 °C and 90 °C. In Figure 6-13 the dark signal of both parts of the pixel array at two different temperatures is shown.

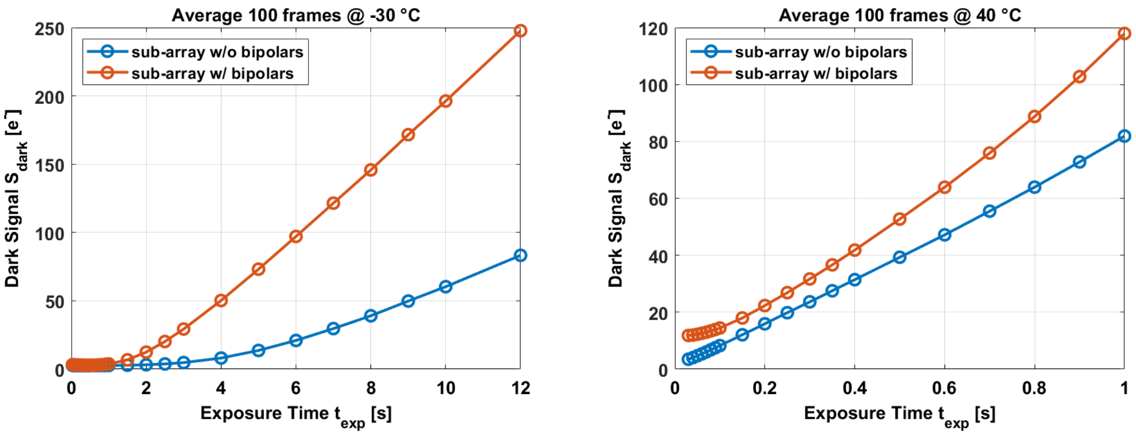

(a) (b)

Figure 6-13: (a) Dark signal of the pixel array with and without bipolars at -30 °C. (b) Dark signal of the pixel array with and without bipolars at 40 °C.

At both temperatures the dark signal of the sub-array with bipolars is higher than the dark signal of the sub-array without bipolars. At -30 °C, the dark current with bipolars is 24.71 e^-/s compared to 9.48 e^-/s without bipolars. This means that the bipolars contribute 62 % more electrons per second at -30 °C. This difference is less significant at 40 °C, where the dark current with bipolars is 106.26 e^-/s compared to 76.59 e^-/s without bipolars. This means a difference of 28 %.

In terms of the variation in dark current over temperature, Figure 6-14 (a) shows the behavior of dark current in the temperature range of -40 °C to 90 °C. At temperatures below 20 °C, the difference in dark current between the sub-array with and without bipolars is more significant than at temperatures above 20 °C. This is because at high temperatures the dark current is more affected by the temperature saturating the photodiode earlier than at low temperatures.

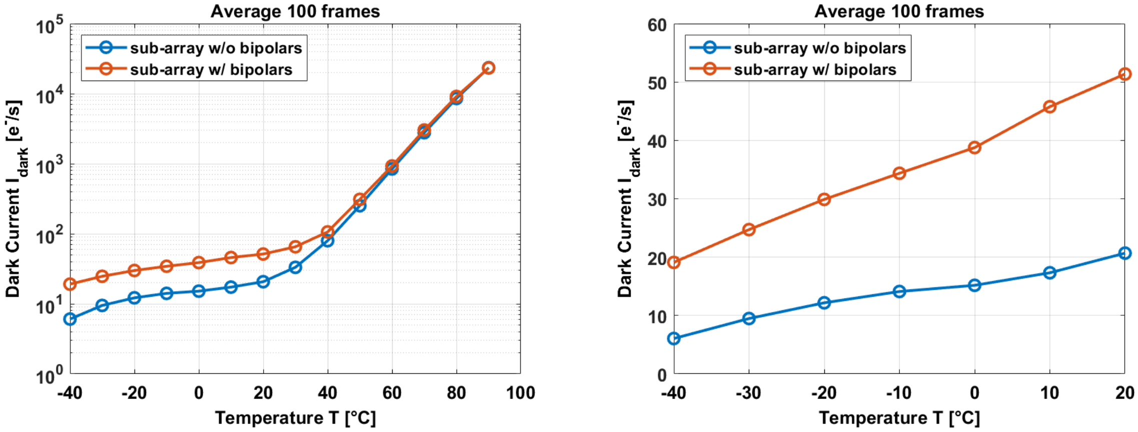

(a) (b)

Figure 6-14: (a) Dark current vs. temperature in the range of -40 °C to 90 °C. (b) Dark current behavior at temperatures below 20 °C.

Figure 6-14 (b) shows the dark current behavior at low temperatures. The integration of bipolars in the pixel array produces higher dark current than in the case without bipolars. In both cases, it is possible to fit a linear or exponential curve where the dark current coefficient with bipolars is 0.53 e^-/s/°C, and without bipolars corresponds to 0.22 e^-/s/°C, resulting in a difference of 60 %. The rate of increase of the pixel sub-array with bipolars is 1.05 times every 5 °C compared to 1.12 times every 5 °C for the pixel sub-array without bipolars. Although this is a small difference in the rate of increase, it suggests that the dark current of the pixel sub-array with bipolars is not only dominated by the depletion dark current itself, but it is also the sum of the depletion dark current plus electrons generated by photons and/or hot carriers generated by the bipolars. If the dark current is converted into a voltage, it reaches a level in the order of 500 μV. The noise level of the readout system is limited by the column amplifier and the external 16-bit ADC, obtaining a total noise level of ~200 μV. Also, the offset of the system can be controlled by an external reference, keeping it at the ground level. Thus, it is believed that the readout system does not limit the output signal of the pixels. Most likely the pixels themselves have a low rate of increase at low temperatures.

6.5 Conclusion

The presence of bipolar-based temperature sensors across the pixel array causes an unusually high dark signal in pixels placed next to the bipolars. This dark signal can be even ten times higher than in normal pixels. It has been shown that the output signal of the hot pixels and the bipolars correlate with each other reaching a maximum output signal at the same exposure time before saturating. The extra dark signal is most probably caused by the presence of photons due to forward biased of the p-n junction of the bipolars (Figure 6-11). However, when switch M1 is turned off and I_{bias1} is kept at 0 μA (Figure 6-8 (b)), there is still higher dark signal than normal. This suggests that some current is coming from the readout circuit via switch M2. Different NIR cameras were utilized to see the EL effect in the pixel array in order to confirm if the cause of this dark signal offset is due to a forward biased p-n junction or a reverse biased p-n junction. Unfortunately, no EL effect was detected by the cameras. One of the reasons could be that the small bias current produces extremely low levels of EL intensity that the cameras might not have been able to measure. Also, the exposure time might not enough to observe EL trough the cameras.

Additionally, measurements of pixel (sub-)arrays with and without bipolars have been performed. For temperatures below 20 °C, the dark current of the pixel sub-array with bipolars increases 1.05 times every 5 °C compared to 1.12 times every 5 °C in the sub-array without bipolars. This confirms that the bipolars affect the dark current increasing rate at low temperatures.

In order to block the photon-emission from the BJTs to the pixels, a wall between the BJTs and the pixels should be placed. Techniques to create this wall could be either deep trench isolation (DTI) or shallow trench isolation (STI). In the case of [2], a reflective STI metal wall was placed between the BJT region and the pixels. A reduction of 2.30 digital number (DN) in dark signal confirms the use of the metal wall in order to reduce the effect of the BJT in dark signal of the pixels. Also, the wafer manufacturing might help to reduce the photon-emission effect. As it was stated in [1], it seems that not all the impurities diffused into a gettering layer at the bottom of the wafer, where the impurities are trapped, due to the presence of the SOI layer that forms a barrier for the diffusion of the impurities. Thus, some impurities diffused into certain areas in the pixel until they are trapped. These observations were shared with the foundry, and new devices were made which do not exhibit hot pixels across the array.

References

[1] G. Meynants, W. Diels, J. Bogaerts, and W. Ogiers, "Emission microscopy analysis of hot cluster defects of imagers processed on SOI," in *Proc. Int. Image Sensor Workshop—IISW*, 2013, pp. 1-4.

[2] K. Seo, S. Lee, P. Ahn, D. Kim, and K. Cho, "A study on photon effect to image plane," in *Proc. Int. Image Sensor Workshop—IISW*, 2017, pp. 176-179.

[3] R. Newman, "Visible Light from a Silicon p-n Junction," *Physical Review,* vol. 100, no. 2, pp. 700-703, 1955.

[4] A. G. Chynoweth and K. G. McKay, "Photon Emission from Avalanche Breakdown in Silicon," *Physical Review,* vol. 102, no. 2, pp. 369-376, 1956.

[5] T. Ong, K. W. Terrill, S. Tam, and C. Hu, "Photon generation in forward-biased silicon p-n junctions," *IEEE Electron Device Letters,* vol. 4, no. 12, pp. 460-462, 1983.

[6] G. Deboy and J. Kolzer, "Fundamentals of light emission from silicon devices," *Semiconductor Science and Technology,* vol. 9, no. 5, pp. 1017-1032, 1994.

[7] D. K. Gautam, W. S. Khokle, and K. B. Garg, "Effect of absorption on photon emission from reverse-biased silicon p-n junctions," *Solid-State Electronics,* vol. 31, no. 6, pp. 1119-1121, 1988.

[8] P. A. Wolff, "Theory of optical radiation from breakdown avalanches in germanium," *Journal of Physics and Chemistry of Solids,* vol. 16, no. 3, pp. 184-190, 1960.

[9] P. Le Minh, "Silicon light emitting devices for integrated applications," Ph.D. Dissertation, University of Twente, pp. 30-45, 2003.

[10] S. Maestre, P. Magnan, F. Lavernhe, and F. Corbiere, "Hot carriers effects and electroluminescence in the CMOS photodiode active pixel sensors," in *Electronic Imaging 2003*, 2003, vol. 5017, pp. 59-67.

[11] D. L. Barton *et al.*, "Infrared light emission from semiconductor devices," presented at the ASM International symposium for testing and failure analysis, 1996.

[12] W. L. Ng, M. A. Lourenço, R. M. Gwilliam, S. Ledain, G. Shao, and K. P. Homewood, "An efficient room-temperature silicon-based light-emitting diode," *Nature,* vol. 410, no. 6825, pp. 192-194, 2001.

[13] X. A. Cao, S. F. LeBoeuf, and T. E. Stecher, "Temperature-dependent electroluminescence of AlGaN-based UV LEDs," *IEEE Electron Device Letters,* vol. 27, no. 5, pp. 329-331, 2006.

[14] A. Abarca and A. Theuwissen, "In-Pixel Temperature Sensors with an Accuracy of ±0.25 °C, a 3σ Variation of ±0.7 °C in the Spatial Domain and a 3σ Variation of ±1 °C in the Temporal Domain," *Micromachines,* vol. 11, no. 7, p. 665, 2020.

7 DARK CURRENT COMPENSATION

This chapter presents a novel technique to compensate for the dark current of a CMOS image sensor (CIS) by using in-pixel temperature sensors (IPTSs). The IPTSs are integrated in the same layer as the image pixels. Therefore, the real temperature variations in the pixel array can be measured as well as the thermal distribution of the pixel array. The dark current compensation can be carried out locally either by using the temperature measurements of the IPTSs to manipulate a pre-recorded dark reference frame, at a certain exposure time, or by creating a dark reference frame from the in-pixel temperature measurements and the temperature behavior of the dark current (previously calibrated). The compensated pre-recorded dark frame or the created dark reference frame is subtracted from the actual images to reduce/cancel the dark signal level of the pictures.

7.1 Introduction

Over the last few decades the growing market for portable devices has pushed the CMOS active pixel sensor (APS) industry to rapidly improve CMOS technology performance. The wide use of the APS is related to its high integrability, low cost, and low power consumption [1], [2]. CMOS APS image sensors are used in a variety of applications, ranging from medical to military, and nowadays they offer a viable alternative to charge coupled device (CCD) technology. Dark current is one of the key parameters which characterizes the performance of the APS, where a low dark current is preferred. However, the continuous downscaling of CMOS technology to sub-micron sizes while keeping dark current levels low is a challenge [3], [4].

Dark current is one of the major components of fixed pattern noise (FPN) in CMOS image sensors (CISs) as well as an important contributor to temporal random noise [4], [5]. Large dark currents in a CMOS image sensor lead to high noise, non-uniformity, and a reduced dynamic range [6]. The dark current exhibits linear behavior with over exposure time, and exponential behavior over temperature. In fact, the dark current doubles every ~5-10 °C [7], [8], [9]. A conventional technique to compensate for dark current is to take a dark reference frame during the picture acquisition at a certain exposure time with closed shutter, and subtract this dark frame from the images. However, the temperature must be kept constant during the acquisition to avoid any dark current variation. Also, some cameras (e.g. mobile phones) do not have a shutter, therefore obtaining the dark reference frame is not possible. A technique to compensate for dark current has been proposed by [10]. In [10] the compensation involves using a Miller differential amplifier with the non-inverting input connected to a dummy shielded photodiode and the inverting input connected to an active photodiode. The offset (dark current level) provided by the dummy shielded photodiode is sampled and subtracted from the video signal (including dark current from the active photodiode) compensating for the dark current of the active pixel. However, the mismatch between the active photodiode and the dummy shielded photodiode is not addressed in [10]. Another technique has been proposed by [11], where the dark current of hundreds of hot pixels is used as a temperature indicator along the pixel array. The dark current of the hot pixels is calibrated in a temperature range of -40 °C to 8 °C [11], and it is used to predict the dark current level of the remaining pixels. However, the compensation is limited to the temperature range of -40 °C to 8 °C and no information about the accuracy of the hot pixels acting as temperature sensors is provided.

We propose using the temperature information provided by in-pixel temperature sensors (IPTSs) to create a dark reference frame at a particular exposure time to compensate for dark current across the pixel array without the need for a shutter. Local temperature variations produce dark current non-uniformities along the pixel array. The temperature variations are mainly generated by the self-heating of the circuitry surrounding the pixel array. For instance, it is common to see local hot spots in the pixel array at locations next to the column readout. A temperature difference in the pixel array up to 2 °C has been reported in [12]. In-pixel temperature sensors distributed throughout the pixel array can detect these hot spots as well as the thermal distribution of the array. The temperature provided by the in-pixel temperature sensors can be used to locally compensate for dark current. The in-pixel temperature sensors have been presented in the previous chapters, where the use of the substrate parasitic bipolar temperature sensor pixel (Tixel) (Chapter 4, [13]), and the use of the imaging pixel itself as a temperature sensor (Chapter 5, [12], [14]) have been shown and proved.

In Section 7.2 a summary of the CIS design is explained as well as how the compensation technique works across the pixel array depending on the type of in-pixel temperature sensor. The compensation technique for both types of temperature sensors is shown, by using real data, in Section 7.3. Finally, a conclusion is given in Section 7.4.

7.2 System Design

The dark current compensation technique has been designed using the data obtained from the test CIS device of Chapter 5. As a summary, the test CIS device is composed of a 60 × 140 pixel array where two types of temperature sensors have been integrated, as shown in Figure 7-1. The right side of the array contains the temperature sensors based on the nMOS source follower (SF) of the pixel. Thus, the pixel itself is used to measure the local temperature, while in the left side of the array 20 pixels have been replaced by BJT-based temperature sensors. nMOS SF temperature sensors (nSFTS) can measure temperature per pixel, but not at the same time as the video signal (by using the same pixel). In comparison, not only do BJT temperature sensors measure temperature per zones in the pixel array, but they can be used at the same time as the pixels.

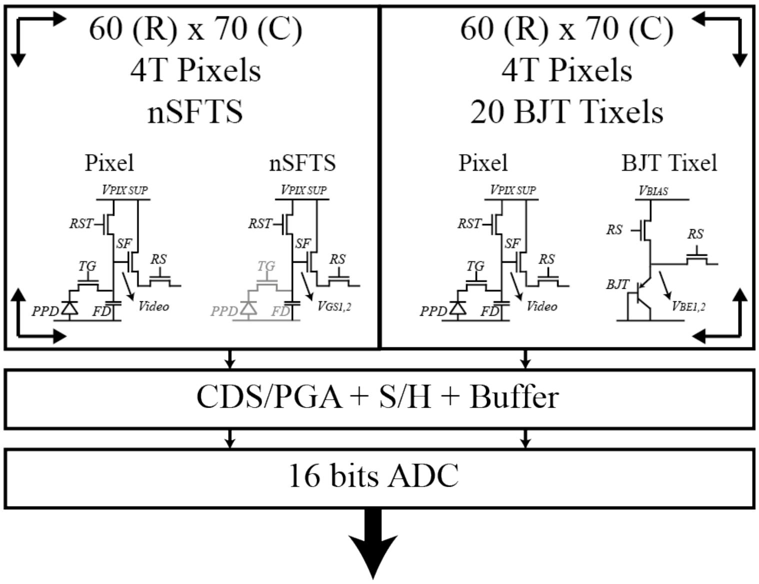

Figure 7-1: Block diagram of the pixel array. The left side of the array contains only 4T pixels. The right side of the array includes pixels and Tixels.

In the case of nSFTSs, a temperature frame (TF) could be taken, for instance, every 20 image frames, as shown in Figure 7-2 (a). However, this incurs in a frame lost (for imaging). Another way to measure the temperature is to use only one column as a temperature sensor (TCO: temperature column) while the rest of the columns are used as normal pixels, as shown in Figure 7-2 (b). For example, in the first frame, the temperature is measured by using column one while the rest of the columns are utilized as normal pixels. Then, in the second frame, the temperature is measured by using column two, and so on for the rest of the frames. In this way, the temperature can be measured per frame changing the temperature column without incurring a frame loss. The TF and the TCO provide the temperature information locally per pixel. Therefore, knowing the temperature of the frame and the temperature behavior of the dark current of the CIS allows the dark current level of each pixel to be estimated.

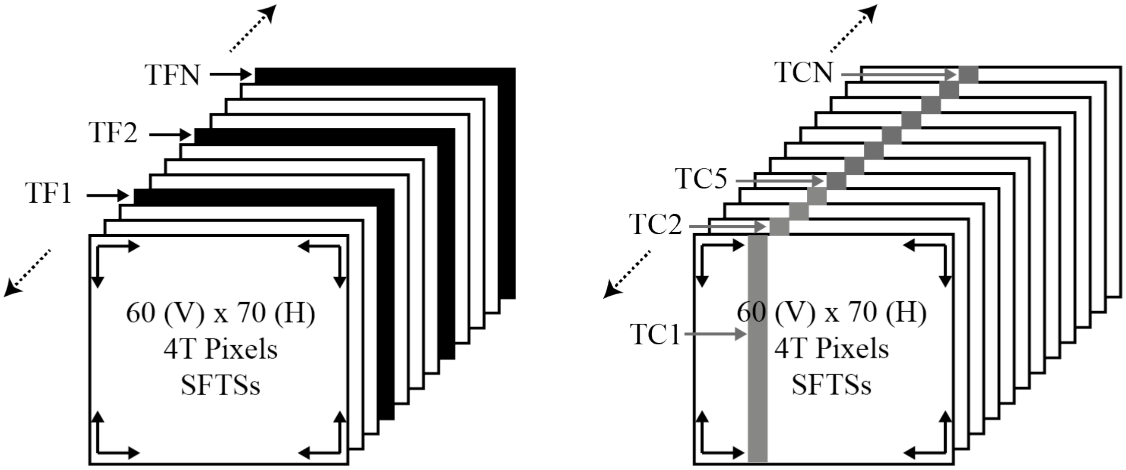

(a) (b)

Figure 7-2: (a) Temperature frames that are taken in between image frames. (b) Temperature columns that are taking in every image frame.

On the other hand, the BJTs can work together with the image pixels, thus, collecting temperature information per frame is also possible (as in the case of nSFTS when TCO are taken). In this case, the dark current can be calculated per pixel zones where each zone contains ~200 pixels in combination with a single BJT-based temperature sensor that estimates the temperature of that zone, as shown in Figure 7-3. In both cases (by using either the nSFTSs or the BJTs), the dark reference frame can be estimated by using the dark current value at a certain exposure time during the calibration of the sensor/camera.

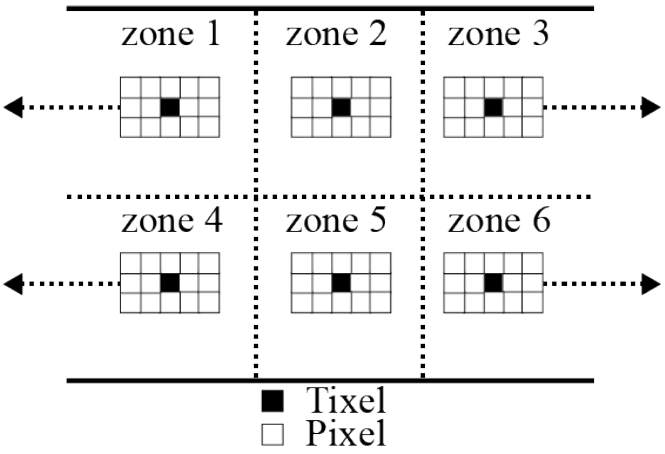

Figure 7-3: Each Tixel measures the temperature for a certain number of pixels in the pixel array (zones).

7.3 Dark Frame Compensation and Generation

After the calibration of the CIS over temperature, the dark current exhibits two types of temperature behavior depending on the temperature range, as shown in Figure 5-23 (b) (Chapter 5). At low temperatures, the average dark current increases 1.08 times every 5 °C, while at high temperatures it increases 1.8 times every 5 °C. Therefore, the dark current becomes more relevant at temperatures above 25 °C. The dark current over temperature is shown in Figure 7-4 (for temperatures above 25 °C).

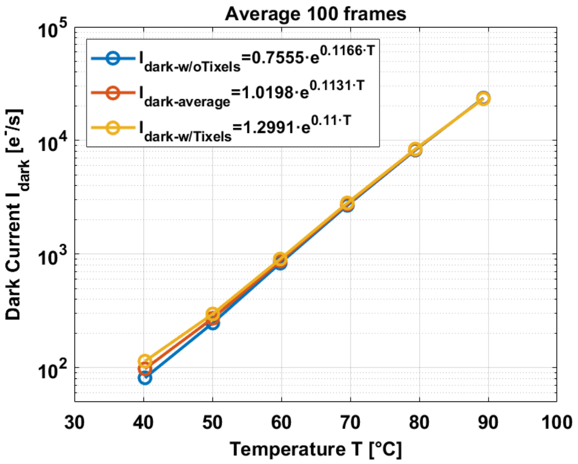

Figure 7-4: Dark current over temperature. The dark current exhibits 2 different behavior depending on the presence of Tixels in the pixel array.

The part of the array with Tixels exhibits a higher dark current than the part of the array without Tixels. When averaging all the pixels of the array without Tixels, the average dark current ($I_{dark-w/oTixels}$) at high temperatures can be fitted by Equation (7-1):

$$I_{dark-w/oTixels} = 0.7555 \cdot e^{0.1166 \cdot T} \tag{7-1}$$

where T corresponds to the absolute temperature.

In the case of the array with Tixels, the average dark current ($I_{dark-w/Tixels}$) at high temperatures can be fitted by Equation (7-2):

$$I_{dark-w/Tixels} = 1.2991 \cdot e^{0.11 \cdot T}. \tag{7-2}$$

On the other hand, both types of temperature sensors show high linearity and good accuracy in the temperature range of -40 °C to 90 °C. The nSFTS has an average temperature coefficient (TC) of 1.07 mV/°C (Figure 5-21 (a), Chapter 5), and an inaccuracy (3σ) of ±0.6 °C (Figure 5-22, Chapter 5). The output signal of the nSFTS corresponds to the differential gate-source voltage (ΔV_{GS}), which is related to the absolute temperature in Equation (7-3) (the average ΔV_{GS} is in mV and the T in °C):

$$\Delta V_{GS} = 1.07 \cdot T + 435.1. \tag{7-3}$$

In the case of the Tixels, an average TC of 1.08 mV/°C (after 1st order curve fitting) and an inaccuracy (3σ) of ±0.5 °C have been achieved (Figure 5-19 (a) and Figure 5-20, respectively; Chapter 5). The output signal of the BJT corresponds to the differential base-emitter voltage ΔV_{BE}, which is related to the absolute temperature in Equation (7-4):

$$\Delta V_{BE} = 1.08 \cdot T + 350.2. \tag{7-4}$$

The compensation technique works as follows: the output differential voltage of the IPTSs is replaced in the $\Delta V - T$ relation to find the corresponding absolute temperature of the image frame. In the case of the nSFTS, the average ΔV-T relation corresponds to Equation (7-3) and for the BJTs it is Equation (7-4). Then, the calculated temperature is replaced in “the dark current-T” Equation (7-1) and/or Equation (7-2) (depending on the part of the array) to calculate the dark current level for that particular temperature. Finally, as the images are related to a certain exposure time, this exposure time is used to obtain the dark signal level of the corresponding image frame. In the case of the nSFTSs, the compensation technique can be done per pixel as the nSFTSs give the temperature level per pixel (thus, the FPN can be highly compensated). With the temperature level per pixel obtained, these values can then be replaced in the temperature behavior of the dark current to find the dark current level per pixel. After determining the exposure time, the dark signal level of each pixel is calculated, and a dark reference frame can be estimated by using the dark signal level of all the pixels. A similar procedure can be applied in the case of the BJT-based temperature sensors, but the dark signal level of a group of pixels is estimated (instead of per pixel as in the nSFTSs). The estimated dark reference frame (either by using the nSFTSs or the BJTs) can either be used to compensate a pre-recorded dark reference frame or applied directly to the images.

For example, in the case of the nSFTS, if the ΔV_{GS} is 488.75 mV, this results in a temperature of 50 °C (using Equation (7-3)). Then, this temperature is replaced in the equation of the dark current vs. temperature (Equation (7-1), dark current without Tixels), resulting in a dark current level of 257.14 e^-/pixel/s. At a 1 s exposure time, the average dark reference level is 257.14 e^-/pixel. The same procedure can be used for the BJTs. Applying Equation (7-4) to obtain the temperature, if ΔV_{BE} is 406.07 mV, then the average temperature corresponds to 51.78 °C. This results in a dark current of 386.63 e^-/pixel/s (by using Equation (7-2)). Therefore, the average dark reference level is 386.63 e^-/pixel at 1 s.

Figure 7-5 (a) shows the histogram of a pre-recorded dark reference frame of a pixel array without Tixels taken at 50 °C and at an exposure time of 1 s. This dark reference frame has a median of 280.91 e^-/pixel and a standard deviation σ of 40 e^-. In the case of the pixel array with Tixels (Figure 7-5 (b)), the median is 379.29 e^-/pixel and the standard deviation of 60 e^-. It is clear the difference in terms of dark signal between the pixel array without Tixels and the pixel array with Tixels. There is a difference of almost 100 e^-/pixel between the two parts of the array. Also, the pixel array with Tixels does not follow exactly a Gaussian distribution and it looks more like a Poisson distribution exhibiting a long tail for high values of dark signal. This is due to the presence of the Tixels that contribute extra dark signal to some pixels across the array. However, due to the large number of samples and the high median value, a Poisson distribution approximates a Gaussian distribution when the median and the standard deviation are calculated in both types of distribution [15]. In the case of the array without Tixels, it also exhibits a tail for high dark signals, but it is considerable shorter than in the case of the array with Tixels. Probably, a few pixels are affected by the Tixels as well.

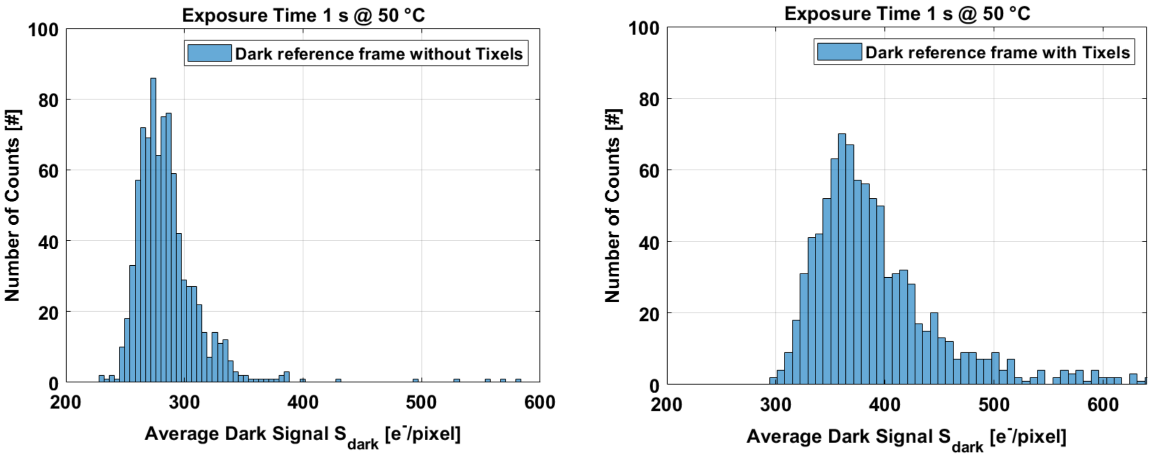

(a) (b)

Figure 7-5: (a) Histogram of a dark reference frame without Tixels at 50 °C and at an exposure time of 1 s. The median corresponds to 280.91 e-/pixel and the σ is 40 e-. (b) Histogram of a dark reference frame with Tixels at 50 °C and at an exposure time of 1 s. The median corresponds to 379.29 e-/pixel and the σ is 60 e-.

For instance, if the average dark level calculated by using the average temperature measurement of the nSFTSs and the Tixels is applied to each pre-recorded dark reference frame of Figure 7-5, then the dark level of each part of the array at 50 °C at an exposure time of 1 s can be highly compensated, as shown in Figure 7-6 (a) and (b).

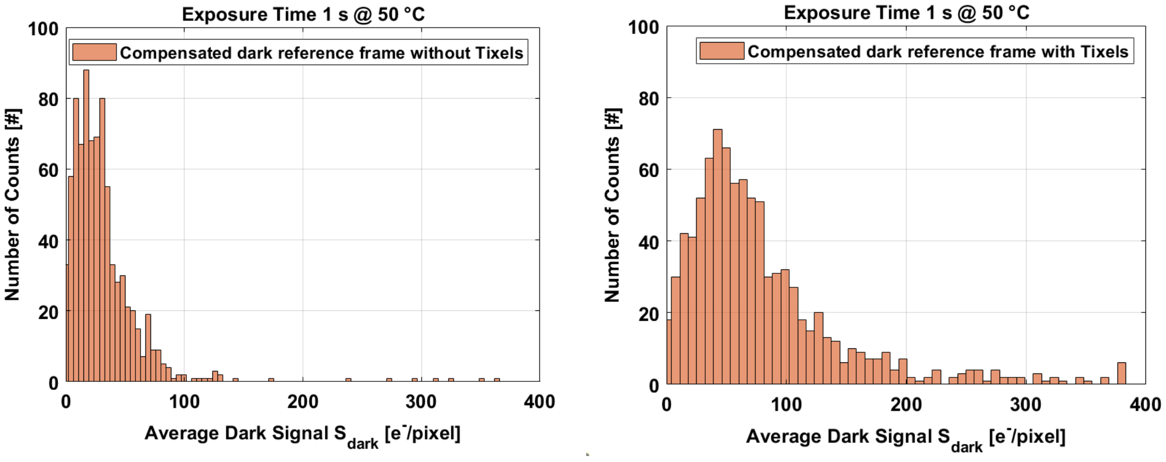

(a) (b)

Figure 7-6: (a) Histogram of a compensated dark reference frame without Tixels. (b) Histogram of a compensated dark reference frame with Tixels. In this case only the median has been compensated as a proof of concept.

The dark reference frame of Figure 7-6 is the result of only compensating the average value of the dark level (as a proof of concept). This is the reason why the non-uniformity of the dark frame remains as well as some values are out of the range. The compensated dark reference frame without Tixels has a median of 23.77 e^-/pixel, thus, the average dark signal is compensated in the order of 90 %. In the case of the pixel array with Tixels, the histogram has a median of 61.41 e^-/pixel, which means that the average dark signal is compensated in the order of 84 %.

A similar procedure can be applied to create a dark reference frame for the pixel's sub-array with the nSFTS and for the pixel's sub-array where the Tixels have been integrated. Then, this created dark reference frame can be applied to the reference dark frame to compensate it. In the case of the nSFTSs, the dark reference frame is calculated by using the individual temperature measurements per pixel obtaining a temperature array. This array of temperatures is applied to Equation (7-1) to find the corresponding dark current per pixel. The dark level per pixel is calculated at a 1 s exposure time. The histogram of the dark reference frame locally compensated by the temperature measurements of the nSFTSs is shown in Figure 7-7.

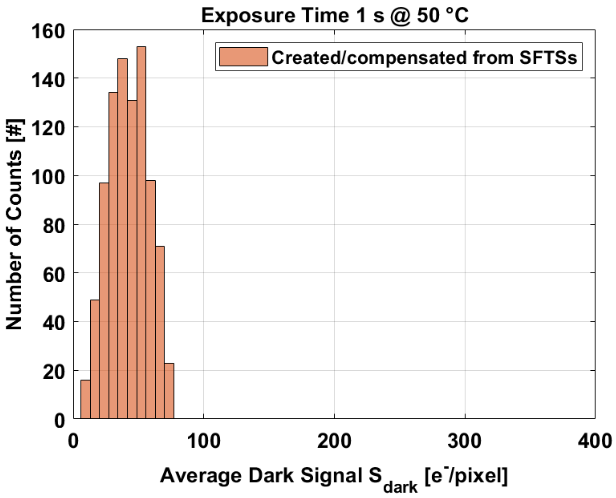

Figure 7-7: Histogram of the dark reference frame created/compensated by using the SFTSs. The median corresponds to 51 e^-/pixel and the σ is 15 e^-.

Comparing the histogram of Figure 7-7 with the reference one in Figure 7-5 (a) shows that the dark signal level is compensated in the order of 82% (considering the median value). In terms of the σ variation, the variation is greatly reduced thanks to the local compensation that the nSFTSs perform across the pixel array. The σ is significantly reduced from 40 e^- to 15 e^-, this means 63 % reduction.

The Tixels produce the dark reference level for approximately ~200 pixels in 20 different zones across the array (Figure 7-3). The histogram of the dark reference frame created/compensated by the temperature measurements of the Tixels is shown in Figure 7-8.

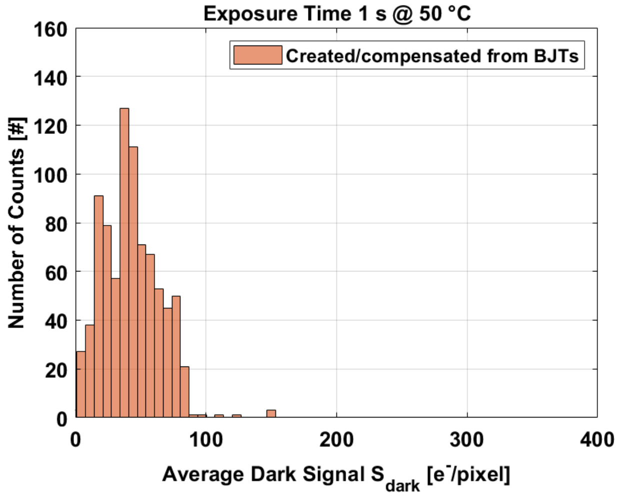

Figure 7-8: Histogram of the dark reference frame created by using the BJT temperature sensors. The median corresponds to 55 e^-/pixel and the σ is 35 e^-.

Comparing the dark reference frame of Figure 7-8 with the pre-recorded reference frame of Figure 7-5 (b) shows that the dark signal is compensated by 85% (considering the median value). However, the σ variation is only reduced from 60 e^- to 35 e^- (42 %) (compared to 63 % in the case of using the nSFTSs). This σ variation in the case of the Tixel's compensation is higher compared to that of the nSFTSs because the Tixels produce a dark level per zone instead of per pixel, as in the case of the nSFTS measurements.

An image of a dark reference frame taken by using the test CIS device is shown in Figure 7-9. This dark reference frame is taken at 1 s exposure and at 50 °C.

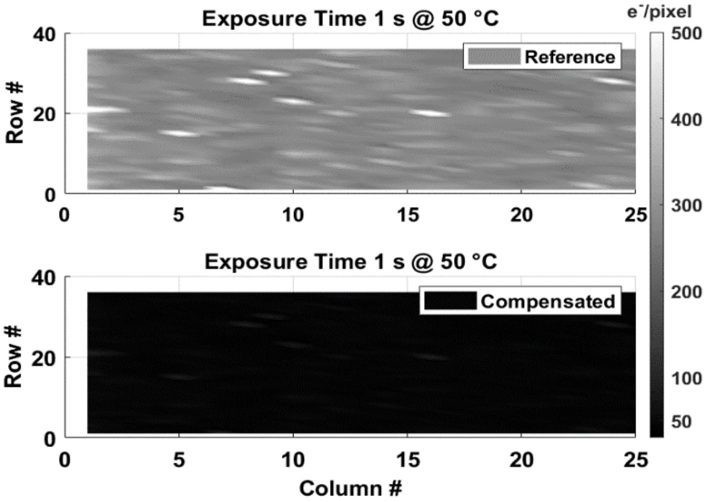

Figure 7-9: Image of the pre-recorded dark reference frame (top); and an image of the compensated dark reference frame (bottom) using the SFTSs. The dark level is reduced from ~300 e$^-$/pixel to ~30 e$^-$/pixel and the non-uniformity is reduced from 35 e$^-$ to 7 e$^-$.

This image is compensated by using the nSFTSs, reducing the dark level from approximately ~300 e$^-$/pixel to ~30 e$^-$/pixel, as shown in Figure 7-9 (bottom). Also, the non-uniformity of the image is reduced from 35 e$^-$ to 7 e$^-$ by using the nSFTSs to compensate the dark reference frame.

The performance of the test CIS device is summarized in Table 7-1 and Table 7-2.

Table 7-1: Summary of the IPTS performance.

Characteristic	Tixel	nSFTS
Type	BJT	nMOS
Resolution (°C)	0.1	0.1
3σ Inaccuracy (°C)	±0.5	±0.6
Range (°C)	−40 to 90	−40 to 90
Area (µm^2)	8591	8591
Technology (µm)	0.18 CIS	0.18 CIS
Power (µW)	110	120

Table 7-2: Summary of the CIS performance.

Characteristic	CIS Pixel
Type	4T
Process [μm]	0.18
Array	60 × 140
Area [μm^2]	11 × 11
Conversion Gain [$\mu V/e^-$]	78
Dark Current @ 30 °C [e^-/pixel]	50
Type	4T

7.4 Conclusion

A novel technique to compensate for the dark current of a CIS without shutter has been presented. The compensation is done using two types of accurate in-pixel temperature sensors that assist in creating/compensating a dark reference frame at a certain exposure time. The in-pixel temperature sensors provide not only the temperature information of the pixel array but also the thermal distribution across the array. In this way, compensation for the dark current can be locally carried out thanks to the integrated temperature sensors. The dark signal can be compensated up to 82 % in its median value and the non-uniformity is reduced in the order of 63 % by using the nSFTSs. In the case of using the Tixels, the median value of the dark reference frame is compensated up to 85 % and the non-uniformity is reduced by 42 %. The nSFTSs achieve better performance, further reducing the non-uniformity compared to the Tixels because the nSFTSs can locally compensate the dark signal instead of compensating per zone in the pixel array, as in the case of Tixels. Table 7-1 and Table 7-2 show the performance of the IPTS and the CIS, respectively.

References

[1] J. Janesick and G. Putnam, "Developments and applications of high-performance CCD and CMOS imaging arrays," *Annual Review of Nuclear and Particle Science,* vol. 53, no. 1, pp. 263-300, 2003.

[2] L. G. McIlrath, "A low-power low-noise ultrawide-dynamic-range CMOS imager with pixel-parallel A/D conversion," *IEEE Journal of Solid-State Circuits,* vol. 36, no. 5, pp. 846-853, 2001.

[3] C. Hsiu-Yu and K. Ya-Chin, "An ultra-low dark current CMOS image sensor cell using n+ ring reset," *IEEE Electron Device Letters,* vol. 23, no. 9, pp. 538-540, 2002.

[4] H. I. Kwon, I. M. Kang, B. G. Park, J. D. Lee, and S. S. Park, "The Analysis of Dark Signals in the CMOS APS Imagers From the Characterization of Test Structures," *IEEE Transactions on Electron Devices,* vol. 51, no. 2, pp. 178-184, 2004.

[5] J. Nakamura, *Image Sensors and Signal Processing for Digital Still Cameras*. Taylor & Francis Group, 2005, pp. 67-72.

[6] S. Yu-Chuan and W. Chung-Yu, "A new CMOS pixel structure for low-dark-current and large-array-size still imager applications," *IEEE Transactions on Circuits and Systems I: Regular Papers,* vol. 51, no. 11, pp. 2204-2214, 2004.

[7] X. Wang, "Noise in sub-micron CMOS image sensors," Ph.D. Dissertation, Delft University of Technology, pp. 46-68, 2008.

[8] P. S. Baranov, V. T. Litvin, D. A. Belous, and A. A. Mantsvetov, "Dark current of the solid-state imagers at high temperature," in *IEEE Conference of Russian Young Researchers in Electrical and Electronic Engineering (EIConRus)*, 2017: IEEE, pp. 635-638.

[9] R. Widenhorn, M. Blouke, A. Weber, A. Rest, and E. Bodegom, "Temperature dependence of dark current in a CCD," in *Electronic Imaging*, 2002, vol. 4669, pp. 193-201.

[10] P. M. Beaudoin, Y. Audet, and V. H. Ponce-Ponce, "Dark current compensation in CMOS image sensors using a differential pixel architecture," in *2009 Joint IEEE North-East Workshop on Circuits and Systems and TAISA Conference*, 2009, pp. 1-4.

[11] R. Widenhorn, A. Rest, M. Blouke, R. Berry, and E. Bodegom, "Computation of dark frames in digital imagers," in *Electronic Imaging 2007*, 2007, vol. 6501, pp. 650103-650111.

[12] S. Xie, A. A. Prouza, and A. Theuwissen, "A CMOS-Imager-Pixel-Based Temperature Sensor for Dark Current Compensation," *IEEE Transactions on Circuits and Systems II: Express Briefs,* vol. 67, no. 2, pp. 255-259, 2020.

[13] A. Abarca, S. Xie, J. Markenhof, and A. Theuwissen, "Integration of 555 temperature sensors into a 64 × 192 CMOS image sensor," *Sensors and Actuators A: Physical,* vol. 282, pp. 243-250, 2018.

[14] A. Abarca and A. Theuwissen, "In-Pixel Temperature Sensors with an Accuracy of ±0.25 °C, a 3σ Variation of ±0.7 °C in the Spatial Domain and a 3σ Variation of ±1 °C in the Temporal Domain," *Micromachines,* vol. 11, no. 7, p. 665, 2020.

[15] K. Grace-Martin. [Online]. Available: https://www.theanalysisfactor.com/differences-between-normal-and-poisson-distributions/.

8 CONCLUSIONS

In this chapter the main contributions and findings of this thesis are summarized. Suggestions for future work in the use of temperature sensors and pixels are also presented in this final chapter.

8.1 Main Contributions

- **For the very first time a bipolar junction transistor-based temperature sensor has been fully integrated into an active pixel array (Chapter 4).**

This design demonstrated that bipolar junction transistor (BJT) based temperature sensors can be integrated into the same layer as the pixels (4T pixel architecture) of a CMOS image sensor. This was never done before. The temperature information provided by the BJTs is intended to be used to compensate for dark signal non-uniformity. The temperature sensor pixel (Tixel) is based on a substrate parasitic bipolar. In this design, 555 pixels have been replaced by the temperature sensors and uniformly distributed across the pixel array. The size of one Tixel corresponds to the size of two pixels. The temperature sensors make use of the same readout circuit as the pixels but without incurring the need for extra circuitry. The readout circuit is based on an in-pixel (in-Tixel) source follower and column amplifiers. In this design, the column amplifiers are based on a switched capacitor amplifier providing different gains: 1, 2, 4, 8 and 16. Thanks to the readout architecture, the temperature information is obtained via the differential base-emitter voltage ΔV_{BE} of the bipolar, which is proportional to absolute temperature (PTAT). The readout architecture also provides the chance to read the temperature information either at the same time as the pixels or without the pixels. Measurements of the Tixels show high linearity in the temperature range of 20 °C to 90 °C exhibiting an average temperature coefficient of 1.2190 mV/°C with a variation of 0.7% from the average. In terms of the inaccuracy of the Tixels, an inaccuracy (3σ) of ±0.3 °C at a gain of 16 (gain of the column amplifier) and ±0.25 °C at a gain of 8 have been achieved.

- **For the very first time the nMOS source follower transistor of the 4T pixel has been used as a temperature sensor (Chapter 5)**

This design introduces the first temperature sensor which makes use of the pixel as a temperature sensor. This was never done before. The temperature sensor is based on the nMOS source follower (nSFTS) transistor inside of the 4T pixel. In this case, the temperature information is obtained via the differential gate-source voltage ΔV_{GS} when the source follower is biased by two different currents in a ratio *N*. It has been demonstrated that ΔV_{GS} is PTAT, as is the case for ΔV_{BE}. The use of the nSFTS does not incur a dead pixel, unlike the Tixel. By using the nSFTS, the temperature can be measured locally. Thus, local dark signal compensation can be performed.

On the other hand, Tixels have also been integrated into this design, but the area has been reduced to the size of one pixel (instead of to two pixels in the previous design).

- **Application of different techniques to improve the accuracy of the in-pixel temperature sensors (Chapter 5)**

The accuracy of the nSFTSs and the Tixels has been improved by using dynamic element matching (DEM), correlated double sampling (CDS), an on-chip bias current based on a bandgap reference (BGR) with a temperature-independent resistor, and a full BGR bias in the column amplifier. The bandgap reference bias current (BGRBC) provides a base current of 1µA with a temperature coefficient of 78.57 ppm/°C (TT corner). Also, the temperature-independent resistor exhibits a variation of 0.06 ppm/°C. The BGRs of the column amplifier have an average temperature variation in the order of 4 ppm/°C. Measurements of the temperature sensors validate the use of all these techniques and circuits because the nSFTSs and Tixels have been achieved an inaccuracy (3σ) of ±0.55 °C and ±0.5 °C, respectively.

- **Technique to compensate for dark current (Chapter 7)**

A novel technique to compensate for the dark current of a CMOS image sensor (CIS) is presented. This technique can be used by CIS devices without a shutter (such as in mobile phones). The compensation can be accomplished either by compensating a pre-recorded dark reference frame or by creating a dark reference frame that can be subtracted from the images. A dark reference frame can be created without the need for a shutter by using the temperature measurements provided by the in-pixel temperature sensors. The IPTSs locally provide the temperature information of the pixel array which is replaced in the exponential behavior of the dark current. Then, the dark signal level can be estimated by using the dark current at a certain exposure time, creating a dark reference frame. The dark signal non-uniformity can be locally compensated by using the nSFTS either to take a temperature frame every 20 image frames or to take temperature measurements per column while performing the image frame acquisition. In the case of the Tixels, the compensation can be carried out per pixel zones across the array. The use of nSFTSs results in a median's compensation of 82 % and 63 % in the case of the σ. In the case of the Tixels, the compensation is in the order of 85 % for the median and 42 % for the σ.

8.2 Main Findings

- **The presence of the Tixels affects the dark signal of the pixels (Chapter 6)**

It has been shown that the dark signal of CMOS pixels located next to the bipolars is almost ten times higher than the dark signal of the pixels placed far from the bipolars. Two effects have been identified as the cause of this phenomenon. The first one is associated to photon emission due to the forward biased of the p-n junction of the bipolars. This causes EL that can be absorbed by the active area of the pixel resulting in a higher dark signal. Forward biased p-n junction has been proved by measurements where the correlation between the output signal of the bipolars and the dark signal of the pixels has been found. The second effect might be related to hot carrier generation. To prove the presence of hot carriers (and also minority carriers), different near infrared (NIR) cameras were used in order to observe the spectrum of the EL. However, no EL was detected by the cameras. One reason might be that the p-n junction of the bipolars produces very low levels of EL intensity due to the small bias current of the BJTs. Another reason might be due to the short exposure time that was used.

8.3 Future Work

- **Isolation of the bipolars in the pixel array**

The presence of the bipolars produces a higher dark signal on those pixels next to the BJTs. To mitigate this effect, a wall surrounding the bipolar could cancel this phenomenon. Deep trench isolation (DTI) can be applied to isolate the bipolars from the pixels. This technique is currently used to cancel the cross-talk sensitivity between pixels in the array.

- **Further improvement in the accuracy of the temperature sensors**

Further investigation is needed into the effect of the beta gain (β_F) of the bipolars. β_F is temperature-dependent and affects the accuracy of the bipolars. In this thesis, the effect of β_F has been reduced by selecting a bias current range where β_F is current-independent. Therefore, an accurate PTAT differential base-emitter voltage can be generated. However, if a different bias current range is preferred (for instance, higher than 1 μA), then the β_F effect must be considered. It is possible to cancel the effect of β_F by adding a well-defined feedback resistor to the bipolar-based temperature sensor, although this resistor is usually added only in temperature sensors based on two bipolars. In this thesis, only one bipolar is used as a temperature sensor to avoid mismatch. A challenge would be either adding the resistor to a single bipolar configuration or integrating a temperature sensor based on two bipolars.

Further investigation is needed into the effect of the carrier mobility (μ) of the nMOS source-follower-based temperature sensor. The temperature effect of the threshold voltage (V_{TH}) of the SF transistor and the process parameter n have been minimized by applying ratiometric currents and sizing the dimensions of the SF transistor, respectively. However, the temperature effect of the mobility has not been considered in this thesis. Also, the mobility exhibits substantial process spread, affecting the accuracy of the SF temperature sensor. It might prove useful to obtain the temperature information by employing two SF transistors instead of one (for instance, two different rows or columns). The second SF transistor can be used to compensate for the mobility effect.

- **Application in a larger pixel array**

The pixel arrays of the different test chips in this thesis have limited size, as they were intended to be a proof-of-concept. Integration of temperature sensors into a larger pixel array would be the next step to see how the temperature information can be used to compensate for dark signal non-uniformity. Also, this would be a powerful tool to view the thermal distribution across the pixel array and observe how the different circuits contribute to the dark signal resulting from self-heating of the circuits. It might give a new perspective on how to place the different circuitry in the chip area itself.

- **Integration of other types of temperature sensors into the pixel array**

This thesis has presented two types of temperature sensors integrated into the pixel array: one based on a substrate parasitic bipolar and another based on the nMOS source follower transistor of the pixels. Promising research has been done into resistor-based temperature sensors [1], [2]. They exhibit high accuracy, with relatively low power consumption. The challenge would be to reduce the size of the resistor-based temperature sensor to the pixel level. Using this kind of temperature sensor would likely cancel the high dark signal produced by the bipolars.

Also, it would be interesting to add a second SF transistor to the pixel to measure the temperature and the video information at the same time. A challenge would be either to use the same readout circuit for the temperature and the video information or to add a second readout for the temperature data (and synchronize both readout systems).

- **On-chip dark signal compensation**

A dark signal compensation scheme has been presented in Chapter 7. This scheme makes use of external circuitry and software. It would be worth investigating the possibility of an on-chip solution. The temperature signal from the temperature sensors could be directly used as a reference for the column amplifier in a subtracting configuration to in-line compensate for dark signal.

References

[1] S. Pan, Y. Luo, S. H. Shalmany, and K. A. A. Makinwa, "A Resistor-Based Temperature Sensor With a 0.13 pJ · K2 Resolution FoM," *IEEE Journal of Solid-State Circuits,* vol. 53, no. 1, pp. 164-173, 2018.

[2] J. A. Angevare and K. A. A. Makinwa, "A 6800-µm2 Resistor-Based Temperature Sensor With ±0.35 °C (3σ) Inaccuracy in 180-nm CMOS," *IEEE Journal of Solid-State Circuits,* vol. 54, no. 10, pp. 2649-2657, 2019.

SUMMARY

This thesis describes the integration of temperature sensors into a CMOS image sensor (CIS). The temperature sensors provide the in-situ temperature of the pixels as well as the thermal distribution of the pixel array. The temperature and the thermal distribution are intended to be used to compensate for dark current affecting the CIS. Two different types of in-pixel temperature sensors have been explored. The first type of temperature sensor is based on a substrate parasitic bipolar junction transistor (BJT). The second type of temperature sensor that has been explored is based on the nMOS source follower (SF) transistor of the same pixel. The readout system that is used for the temperature sensors and for the image pixels is based on low noise column amplifiers. Both types of in-pixel temperature sensors (IPTS) have been designed implementing different techniques to improve their accuracy. The use of the IPTSs has been proved by measuring three prototypes chips. Also, a novel technique to compensate for the dark current of a CIS by using the IPTS has been proposed.

Chapter 1

Chapter 1 introduces the background, motivation and the outline of this thesis. An overview of silicon-based image sensors is given along with the charge coupled device (CCD) and the CMOS image sensor. Their main characteristics and differences are explained as well as their evolution throughout the last few decades. This chapter explores the reasons why the CIS has overtaken the CCD over the last few years. Also, an overview of different types of temperature sensors is given along with their evolution since the first appearance of BJTs in temperature-independent bandgap references (BGRs). The objectives of this thesis are stated in this first chapter.

Chapter 2

Chapter 2 presents an overview of the main characteristics of the CIS, explaining the evolution from the passive pixel sensor (PPS) to the active pixel sensor (APS) and the importance of the photodiode as the core of a CIS. Also, two APS architectures are explained: the 3T architecture and the 4T architecture. The 4T architecture has become the main structure used as a pixel because of its excellent performance. Different metrics and noise sources to characterize a CIS are explained as well.

Chapter 3

Chapter 3 gives a deeper analysis of the dark current in a CIS. The dark current is one of the major contributors of fixed pattern noise (FPN) in a CMOS image sensor. The dark current is generated from different sources: depletion dark current, diffusion dark current, and surface dark current. In a 4T architecture, the surface dark current is highly suppressed by the use of the pinned photodiode. An analysis of the time and temperature dependence of dark current has resulted in a verification of the dark current’s linear dependency on time and exponential dependency on temperature.

Chapter 4

Chapter 4 introduces the first CMOS image sensors where bipolar-based temperature sensors have been integrated. 555 pixels have been replaced with temperature sensor pixels (Tixels). These Tixels are uniformly distributed across the pixel array and the Tixels utilize the same readout system as the image pixels. The temperature information is obtained via the differential base-emitter voltage provided by the BJT when the bipolar is biased by two different currents in a ratio of 4:1. Measurement results prove the use of temperature sensors in a CIS as well as the temperature dependency of the dark current. Tixels exhibit high linearity and good accuracy, confirming that they can be used to compensate for the dark current of a CIS.

Chapter 5

Chapter 5 introduces a second type of in-pixel temperature sensor based on the nMOS source follower of the pixel itself. The nMOS source follower temperature sensor (nSFTS) measures the temperature via the differential gate-source voltage when the source follower transistor is biased by two different currents in a ratio of 4:1. A prototype chip including the bipolar temperature sensor and the nSFTS has been designed and tested. Different circuit techniques to improve the accuracy of the temperature sensors are included in this prototype. Dynamic element matching (DEM), correlated double sampling (CDS), a novel on-chip bias current based on a bandgap reference, and a fully temperature compensated column amplifier are applied to improve the accuracy of the temperature sensors. The inaccuracy (3σ) of the Tixel is ±0.5 °C and ±0.55 °C in the case of the nSFTS.

Chapter 6

Chapter 6 explains the sources of an unusually high output signal from some pixels when the dark current is measured in the CIS. Those pixels located next to the BJT-based temperature sensors are the ones exhibiting this high dark current. This effect is related to two different mechanisms: forward biased p-n junction and reverse biased p-n junction. Both phenomena generate electroluminescence (EL) effect. The carriers are generated in the p-n junction of the BJT, with some carriers reaching the photodiode, adding extra electrons to the dark current. The EL effect generates photons via radiative recombination, with some of these photons being absorbed into the photodiode of the pixel.

Chapter 7

Chapter 7 introduces a novel technique to compensate for dark current. As the dark current greatly depends on the temperature variations, the IPTSs are used to identify the temperature of the pixel array as well as the thermal distribution across the array. The dark current exhibits high non-uniformity along the pixel array which is mainly caused by the self-heating of the surrounding circuitry. The dark current can be locally compensated by uniformly distributing the temperature sensors in the pixel array. The dark current compensation can be carried out either by compensating a pre-recorded dark reference frame or by creating a dark reference frame from the temperature information provided by the IPTSs. Compensation for dark current in the order of 85 % can be reached by using either the bipolars or the SFTS. The main difference between using bipolars or nSFTSs is extent to which the dark signal non-uniformity is reduced. Bipolars only reduce the non-uniformity in the order of 42 % compared to the 63 % non-uniformity reduction when nSFTSs are used. This difference arises because the nSFTSs compensate per pixel while the bipolars compensate per group of pixels.

Chapter 8

Chapter 8 summarizes the main contributions and findings of this thesis as well as giving suggestions for future work in the use of in-pixel temperature sensors.

SAMENVATTING

Dit proefschrift beschrijft de integratie van temperatuursensoren in een CMOS image sensor (CIS). De temperatuursensoren zorgen voor de in-situ temperatuur van de pixels, evenals de thermische distributie van de pixelreeks. De temperatuur en de thermische verdeling zijn bedoeld om te compenseren voor donkerstroom die het CIS beïnvloedt. Er zijn twee verschillende soorten in-pixel temperatuursensoren onderzocht. Het eerste type temperatuursensor is gebaseerd op een substraat-parasitaire bipolaire junctie-transistor (BJT). Het tweede type temperatuursensor dat is onderzocht, is gebaseerd op de nMOS source follower (SF) -transistor van dezelfde pixel. Het uitleessysteem dat is gebruikt voor de temperatuursensoren en voor de beeldpixels is gebaseerd op ruisarme kolomversterkers. Beide soorten in-pixel temperatuursensoren (IPTS) zijn ontworpen, evenals verschillende technieken om hun nauwkeurigheid te verbeteren. Het gebruik van de IPTSs is bewezen door het meten van drie prototypes chips. Er is ook een nieuwe techniek voorgesteld om de donkerstroom van een CIS te compenseren door gebruik te maken van IPTS.

Hoofdstuk 1

Hoofdstuk 1 introduceert de achtergrond, motivatie en de opzet van dit proefschrift. Er wordt een overzicht gegeven van de op silicium gebaseerde beeldsensoren, met zowel het charge coupled device (CCD) als de CMOS image sensor. Hun belangrijkste kenmerken en verschillen worden uitgelegd, evenals hun evolutie in de afgelopen decennia. Het vermeldt de redenen waarom het CIS de CCD de afgelopen jaren heeft ingehaald. Ook wordt een overzicht gegeven van verschillende soorten temperatuursensoren en hun evolutie sinds de eerste verschijning van BJT's in temperatuuronafhankelijke bandgap referenties (BGR). De doelstellingen van dit proefschrift worden vermeld in dit eerste hoofdstuk.

Hoofdstuk 2

Hoofdstuk 2 geeft een overzicht van de belangrijkste kenmerken van het CIS, waarin de evolutie van de passieve pixel sensor (PPS) naar de actieve pixel sensor (APS) en het belang van de fotodiode als de kern van een CIS wordt uitgelegd. Ook worden twee architecturen van APS uitgelegd: de 3T-architectuur en de 4T-architectuur. De 4T-architectuur is de belangrijkste structuur geworden die als pixel moet worden gebruikt vanwege zijn uitstekende prestaties. Verschillende statistieken en ruisbronnen om een CIS te karakteriseren, worden ook uitgelegd.

Hoofdstuk 3

Hoofdstuk 3 geeft een diepere analyse van de donkerstroom in een CIS. De donkerstroom is een van de belangrijkste oorzaken van fixed pattern noise (FPN) in een CMOS image sensor. De donkerstroom wordt gegenereerd uit verschillende bronnen: depletie donkerstroom, diffusie donkerstroom en oppervlakte donkerstroom. In een 4T-architectuur wordt de donkerstroom aan het oppervlak sterk onderdrukt door het gebruik van de vastgezette pinned fotodiode. De tijdsafhankelijkheid en de temperatuurafhankelijkheid van de donkerstroom worden geanalyseerd, waarbij de lineaire afhankelijkheid van de tijd en de exponentiële afhankelijkheid van de temperatuur wordt aangegeven.

Hoofdstuk 4

Hoofdstuk 4 introduceert de eerste CMOS image sensor waarin bipolaire temperatuursensoren zijn geïntegreerd. 555 pixels zijn vervangen door temperatuursensoren pixels (Tixels). Deze Tixels zijn gelijkmatig verdeeld over de pixelarray en de Tixels maken gebruik van hetzelfde uitleessysteem van de beeldpixels. De temperatuurinformatie wordt verkregen via de differentiële basis-emitterspanning die wordt geleverd door de BJT wanneer de bipolaire spanning wordt voorgespannen door twee verschillende stromen in een verhouding van 4: 1. Meetresultaten bewijzen het gebruik van temperatuursensoren in een CIS en de temperatuurafhankelijkheid van de donkerstroom. Tixels vertonen een hoge lineariteit en een goede nauwkeurigheid, wat bevestigt dat ze kunnen worden gebruikt om de donkerstroom van een CIS te compenseren.

Hoofdstuk 5

Hoofdstuk 5 introduceert een tweede type in-pixel temperatuursensor gebaseerd op de nMOS source follower van de pixel zelf. De source-follower-temperatuursensor (SFTS) meet de temperatuur via de differentiële gate-source-spanning wanneer de SF wordt voorgespannen door twee verschillende stromen in een verhouding van 4: 1. Een prototype chip inclusief de bipolaire temperatuursensor en de SFTS is ontworpen en getest. In dit prototype zijn verschillende circuittechnieken opgenomen om de nauwkeurigheid van de temperatuursensoren te verbeteren. Dynamic element matching (DEM), correlated double sampling (CDS), een nieuwe on-chip biasstroom op basis van een bandgap-referentie, en een volledig temperatuur gecompenseerde kolomversterker zijn toegepast om de nauwkeurigheid van de temperatuursensoren te verbeteren. De nauwkeurigheid (3σ) van de Tixel is ±0,5 °C en ±0,55 °C in het geval van de nSFTS.

Hoofdstuk 6

Hoofdstuk 6 legt de bronnen uit van een ongewoon hoog uitgangssignaal van sommige pixels wanneer de donkerstroom wordt gemeten in het CIS. Die pixels naast de op BJT gebaseerde temperatuursensoren zijn degenen die deze hoge donkerstroom vertonen. Dit effect houdt verband met twee verschillende mechanismen: voorwaarts voorgespannen pn-overgang en omgekeerd voorgespannen pn-overgang. Beide fenomenen genereren een elektroluminescentie (EL) effect. De dragers worden gegenereerd in de p-n-overgang van de BJT en sommige elektronen bereiken de fotodiode, waardoor extra elektronen aan de donkerstroom worden toegevoegd. Het EL-effect genereert fotonen door stralingsrecombinatie en een deel van deze fotonen wordt geabsorbeerd door de fotodiode van de pixel.

Hoofdstuk 7

Hoofdstuk 7 introduceert een nieuwe techniek om donker stroom te compenseren. Omdat de donkerstroom sterk afhankelijk is van de temperatuurvariaties, worden de IPTSs gebruikt om de temperatuur van de pixelarray te kennen, evenals de thermische verdeling over de array. De donkerstroom vertoont een hoge ongelijkmatigheid langs de pixelreeks, die voornamelijk wordt veroorzaakt door de zelfverhitting van de omringende schakelingen. De donkerstroom kan lokaal worden gecompenseerd door de temperatuursensoren gelijkmatig in de pixelreeks te verdelen. De donkerstroomcompensatie kan worden uitgevoerd door m.b.v. een vooraf opgenomen donker referentieframe te compenseren of door een donker referentieframe te creëren op basis van de temperatuurinformatie die door de IPTSs. Compensaties voor donkerstroom in de orde van 85% kunnen worden bereikt door gebruik te maken van de bipolaire waarden of de SFTS. Het belangrijkste verschil bij het gebruik van de bipolaire of nSFTSs is afhankelijk van de vermindering van de niet-uniformiteit van het donkere signaal. De bipolaire staven verminderen de niet-uniformiteit slechts in de orde van 42 % vergeleken met de 63 % vermindering van de niet-uniformiteit wanneer de nSFTSs worden gebruikt. Dit verschil wordt verklaard doordat de nSFTSs compenseren per pixel, terwijl de bipolairen in plaats daarvan een groep pixels compenseren.

Hoofdstuk 8

Hoofdstuk 8 vat de belangrijkste bijdragen en bevindingen van dit proefschrift samen en geeft suggesties voor toekomstig werk in het gebruik van in-pixel temperatuursensoren.

TABLE OF FIGURES

LIST OF ABBREVIATIONS

3T	3 transistors
4T	4 transistors
ADC	Analog-to-digital converter
APS	Active pixel sensor
BGR	Bandgap reference
BGRBC	Bandgap reference bias current
BJT	Bipolar junction transistor
BSI	Backside illumination
CCD	Charge coupled device
CDS	Correlated double sampling
CG	Conversion gain
CIS	CMOS image sensor

CMOS	Complementary metal-oxide-semiconductor
CS	Column select
DC	Direct current
DDS	Double data sampling
DEM	Dynamic element matching
DN	Digital number
DR	Dynamic range
DSNU	Dark signal non-uniformity
DTI	Deep trench isolation
EL	Electroluminescence
EMMI	Emission microscopy
FD	Floating diffusion
FF	Fill factor
FPN	Fixed pattern noise
FWC	Full well capacity
IC	Integrated circuit
IPTS	In-pixel temperature sensor
LOFIC	Lateral overflow integration capacitor
MOS	Metal-oxide-semiconductor
NIR	Near infrared
nMOS	n-type MOS
nSFTS	nMOS source follower temperature sensor
OPAMP	Operational amplifier
PD	Photodiode

PGA	Programmable gain amplifier
pMOS	p-type MOS
PPD	Pinned photodiode
PPS	Passive pixel sensor
PRNU	Photon response non-uniformity
PTAT	Proportional to absolute temperature
QE	Quantum efficiency
R	Responsivity
RS	Row select
RST	Reset transistor
RT	Room temperature
S/H	Sample and hold
SF	Source follower
SNR	Signal-to-noise ratio
SoC	System-on-chip
TC	Temperature coefficient
TCO	Temperature column
TF	Temperature frame
TG	Transfer gate
Tixel	Temperature sensor pixel

LIST OF PUBLICATIONS

Journal Articles

A. Abarca, and A. Theuwissen, “In-Pixel Temperature Sensors with an Accuracy of ±0.25 °C, a 3σ Variation of ±0.7 °C in the Spatial Domain and a 3σ Variation of ±1 °C in the Temporal Domain,” *Micromachines*, vol. 11, no. 7, 665, Jul. 2020;

S. Xie, **A Abarca Prouza**, and A. Theuwissen, “A CMOS-Imager-Pixel-Based Temperature Sensor for Dark Current Compensation,” *IEEE Transactions on Circuits and Systems II: Express Briefs*, vol. 67, no. 2, pp. 255-259, Feb. 2020;

A. Abarca, S. Xie, J. Markenhof, and A. Theuwissen, “Integration of 555 Temperature Sensors into a 64 × 192 CMOS Image Sensor,” *Sensors and Actuators A: Physical*, vol. 282, pp. 243-250, Oct. 2018.

Conference Proceedings

S. Xie, **A. Abarca Prouza**, and A. Theuwissen, “A CMOS Image Sensor with In-pixel Temperature Sensors for Dark Signal Non-uniformity,” *International Image Sensor Workshop 2019*, Snowbird, Utah, USA, pp. 31-34, 2019;

S. Xie, **A. Abarca**, J. Markenhof, X. Ge and A. Theuwissen, "Analysis and Calibration of Process Variations for an Array of Temperature Sensors," *2017 IEEE SENSORS*, Glasgow, United Kingdom, pp. 1-3, 2017;

A. Abarca, S. Xie, J. Markenhof, and A. Theuwissen, “Temperature Sensors Integrated into a CMOS Image Sensor,” *Eurosensors 2017 Proc. Engineering*, Paris, France, vol.1, pp. 358-361, 2017.

ABOUT THE AUTHOR

Accel Abarca was born in Santiago, Chile, in 1983. He received his B.Sc. degree and Professional Engineering degree (summa cum laude) in Electrical Engineering from the University of Chile, Chile in May 2011. From 2011 to 2013, he worked as a researcher at the University of Chile and at the Advanced Mining Technology Center (AMTC) in the area of sensors for meteorology and seismology. In 2013, he started his Master's in Microelectronics at Delft University of Technology. He completed his M.Sc. in Microelectronics in September 2015 with a Master's thesis in the area of flow-independent thermal conductivity detectors for gas sensing. After his Master's, he worked as a researcher in the Electronic Instrumentation Laboratory, Delft University of Technology, in the area of temperature sensor integration in CMOS image sensors. From 2017 to 2021, he was been a Ph.D. candidate in the Electronic Instrumentation Laboratory, Delft University of Technology, in the area of in-pixel temperature sensors compensation for dark signal non-uniformity in CMOS image sensors.

ACKNOWLEDGMENTS

This thesis is the final step of a journey that started when I came to the Netherlands almost eight years ago to pursue my Master's degree and then my Ph.D. Throughout these years, I have had the pleasure of meeting many people who made my experience very pleasant.

First of all, I would like to express my deepest gratitude to my supervisor Prof. Albert J. P. Theuwissen for granting the opportunity to join his group and do research into such a fascinating topic. His profound understanding of CMOS image sensors has always amazed me, especially his precision when it comes to details. His amazing talent and vast experience in CMOSs are only the professional side, though. I got to know him as a person who knows how to enjoy life. If there is a question about music (especially about Neil Young), he probably has the answer. I really appreciate all the talks and advice, both professional and personal. I feel proud and content having been part of his group.

In addition, I would like to thank Dr. Shuang Xie, my co-promotor during the first two years of my Ph.D. journey. I learned a lot from her solid knowledge about IC design and testing experience.

Next, I would like to express my gratitude to the committee members for their participation. Many thanks to: Prof. Kofi Makinwa, Prof. Paddy French, Prof. Qinwen Fan, Prof. Marcos Diaz, Prof. Pierre Magnan, Prof. Kristina Bliznakova, and Dr. Guy Meynants.

Special thanks to Prof. Marcos Diaz, a real free spirit, who introduced Microelectronics to me and encouraged me to study abroad. He has been a great inspiration ever since. Without his help and guidance, it might have been a whole different story.

I am very grateful to all my colleagues from the CMOS Image Sensor group not only for all the technical discussions but also for the pleasant talks we had. Many thanks to Xiaoliang, Fei, Weihan, Liqiang, and Jaekyum.

This research could not have been possible without the help of the technicians in our Laboratory: Lukasz, Zuyao, Ron, and Jeroen. Many thanks for solving the impossible!

Many thanks to Dr. Sining Pan who reviewed this thesis and helped me to improve it with his valuable comments.

My special thanks to our kind, friendly, and super-efficient secretary, Joyce Siemers.

I would like to thank all my colleagues and friends from the Electronic Instrumentation Laboratory: Thije, Mingliang, Chao, Hui, Taehoon, Teruki, Jan, Eren, Efraim, Yannick, Eunchul, Shoubnik, Long, Annemarijn, Douwe, Bahman, Zhao. Special thanks to the EI football team “Chopper United”: Arthur, Roger, Jaesung, Amir, Jaekyum. Such a great team we had, guys; I have the best memories!

My life in Delft would not have been so nice without all the friends I have made through all these years. Luzma, Ale, Moises, Toño, Jandro, Jet, Nico, Maca, Oscar, Carlos, Rodolfo, Kiki, Daniel, Ramin, Vanida, Lida, Rocio, Ignacio, Isidora, Bernat, Nadjla, Tele, Phaedra, Tommy, Pato, Javier, Nicole, Lucas, Lore, Thomas, Mari, Jorge, Fra, Maca, Diego, Luis, Paulina, and Diego – you, guys, are the best!

Also, I am grateful to my friend, Soheil. He explained so many things about living here. Also, he took me to the Sundays’ football – my passion for years. Thanks to Pooria, Daniel, Ali, Stefan, Mohammad, Alireza, JP, Amid.

I would like to express all my gratitude to my mom, Ivonne, and my grandparents, Pepa, Tata Mario, Abuelita Albina and Tata Eduardo: thank you very much for your love and constant support all these years. Also, to my in-laws: Tamás, Dorottya, Tamás-jr for their friendliness and support.

Finally, the most important persons in my life: my wife, Dóri, and my daughter, Lucía. I am so grateful for all your support, understanding, and love through this journey. I love you both. It is all about you girls!

Accel Abarca

Delft, August 2021